

ROTATING NUCLEAR RINGS AND EXTREME STARBURSTS IN ULTRALUMINOUS GALAXIES

D. DOWNES

Institut de Radio Astronomie Millimétrique, 38406 St. Martin d'Hères, France; downes@iram.fr

AND

P. M. SOLOMON

Astronomy Program, State University of New York, Stony Brook, NY 11794; psolomon@astro.sunysb.edu

Received 1997 June 26; accepted 1998 June 18

ABSTRACT

New CO interferometer data show that the molecular gas in infrared ultraluminous galaxies is in rotating nuclear disks or rings. The CO maps yield disk radii, kinematic major axes, rotation speeds, enclosed dynamical masses, and gas masses. The CO brightness temperatures, the double-peaked CO line profiles, the limits on thermal continuum flux from dust, and the constraint that the gas mass must be less than the dynamical mass all indicate that the CO lines are subthermally excited and moderately opaque ($\tau = 4$ to 10). We fit kinematic models in which most of the CO flux comes from a moderate-density warm intercloud medium, rather than from self-gravitating clouds. Typical ring radii are 300 to 800 pc. We derive gas masses not from a standard CO-to-mass ratio, but from a model of radiative transfer through subthermally excited CO in the molecular disks. This model yields gas masses of $\sim 5 \times 10^9 M_\odot$, ~ 5 times lower than the standard method, and a ratio $M_{\text{gas}}/L_{\text{CO}} \approx 0.8 M_\odot (\text{K km s}^{-1} \text{pc}^2)^{-1}$. In the nuclear disks, we derive a ratio of gas to dynamical mass of $M_{\text{gas}}/M_{\text{dyn}} \approx 1/6$, and a maximum ratio of gas to total mass surface density, μ/μ_{tot} , of 1/3. For the galaxies VII Zw 31, Arp 193, and IRAS 10565+2448, the CO position-velocity diagrams provide good evidence for rotating molecular rings with a central gap. In addition to the rotating central rings or disks, a new class of star formation region is identified, which we call an extreme starburst. These have a characteristic sizes of only 100 pc, with about $10^9 M_\odot$ of gas and an IR luminosity of $\approx 3 \times 10^{11} L_\odot$ from recently formed OB stars. Four extreme starbursts are identified in the 3 closest galaxies in the sample, including Arp 220, Arp 193, and Mrk 273. These are the most prodigious star formation events in the local universe, each representing about 1000 times as many OB stars as 30 Doradus. In Mrk 231, the CO (2–1) velocity diagram along the line of nodes shows a 1.2 diameter inner disk and a 3" diameter outer disk. The narrow CO line width, the single-peak line profile, the equality of the major and minor axes, and the observed velocity gradients all imply that the molecular disk is nearly face-on, yielding low optical and UV extinction to the active galactic nucleus (AGN). Such a geometry means that the molecular disk cannot be heated by the AGN; the far-infrared (FIR) luminosity of Mrk 231 is powered by a starburst, not the AGN. In Mrk 273, the CO (1–0) maps show long streamers of radius 5 kpc (7") with velocity gradients north-south, and a nuclear disk of radius 400 pc (0.6") with velocity gradients east-west. The nuclear disk contains a bright CO core of radius 120 pc (0.2"). In Arp 220, the CO and 1.3 mm continuum maps show the two "nuclei" embedded in a central ring or disk at P.A. 50° and a fainter structure extending 7" (3 kpc) to the east, normal to the nuclear disk. Models of the CO and dust flux indicate that the two K-band sources contain high-density gas, with $n(\text{H}_2) = 2 \times 10^4 \text{ cm}^{-3}$. There is no evidence that these sources really are the premerger nuclei. They are more likely to be compact extreme starburst regions, containing $10^9 M_\odot$ of dense molecular gas and new stars, but no old stars. Most of the HCN emission arises in the two nuclei. The luminosity-to-mass ratios for the CO sources in Arp 220 are compatible with the early phases of compact starbursts. There is a large mass of molecular gas currently forming stars with plenty of ionizing photons, and no obvious AGN. The entire bolometric luminosity of Arp 220 comes from starbursts, not an AGN. The CO maps show that the gas in ultraluminous IR galaxies is in extended disks that cannot intercept all the power of central AGNs, even if they exist. We conclude that in ultraluminous IR galaxies—even in Mrk 231, which hosts a quasar—the FIR luminosity is powered by extreme starbursts in the molecular rings or disks, not by dust-enshrouded quasars.

Subject headings: galaxies: ISM — galaxies: kinematics and dynamics — galaxies: nuclei — radio lines: galaxies

1. INTRODUCTION

Infrared ultraluminous galaxies are recent galaxy mergers in which much of the gas in the former spiral disks has fallen into the center. The gas reestablishes rotational support at a radius of a few hundred parsecs. This is the same size scale as the narrow-line region in active galactic nuclei (AGNs) and the rotating nuclear disks in some elliptical galaxies. During its infall from 5 to 0.5 kpc, the high-density gas forms many massive stars, as in the early starbursts that

formed the bulge stars in protogalaxies at high redshifts. The ultraluminous galaxies we observe in the local universe are reenacting this primeval process, with a large part of the central mass in gas ready to turn into stars, and ready to fall into a black hole.

The large nuclear concentration of molecular gas in ultraluminous galaxies has been detected in the millimeter lines of CO by many groups during the past decade. Scaling to the signal strengths from Milky Way molecular clouds,

however, soon led to a paradox for many of the sources—the estimated gas mass was equal to or larger than the dynamical mass indicated by the line widths. For Arp 220, for example, Scoville et al. (1991) found that nearly all of the mass in the central few hundred pc was in the form of molecular gas. To resolve this dilemma, we showed that in the extreme environment in the central 600 pc of ultraluminous galaxies, much of the CO luminosity must come from an intercloud medium that fills the whole volume, rather than from clouds bound by self-gravity, and therefore the CO luminosity traces the geometric mean of the gas mass and the dynamical mass, rather than just the gas mass (Downes, Solomon, & Radford 1993). This allows the nuclear disk gas to be overluminous in CO relative to self-gravitating clouds in galactic spiral arms. The important line width for this calculation is the dynamical line width of the galaxy, not that of individual self-gravitating giant molecular clouds (GMCs). The physical basis for estimating gas mass from the CO emission is therefore different from that in Milky Way GMCs. The Milky Way conversion factor is relevant for an ensemble of GMCs in an ordinary spiral galaxy, but not for the center of an ultraluminous galaxy.

In a subsequent survey paper on 37 ultraluminous galaxies observed with the IRAM 30 m telescope (Solomon et al. 1997), we derived the molecular gas mass by several methods. The minimum estimates of the gas mass, for optically thin CO, did indeed reduce the gas mass to much lower fractions of the dynamical mass. The true gas mass must be between the optically thin CO estimate and the dynamical mass, *both* of which are less than the gas mass derived with the Milky Way conversion factor for self-gravitating molecular clouds.

The significance of the lower molecular gas mass is twofold. First, it makes the gas mass smaller than the dynamical mass, as it must be. Second, it means the total molecular gas mass in ultraluminous galaxies is similar to, and not greater than, the molecular mass in the disk of a gas-rich spiral. It is thus not necessary to force all the gas in the galaxy, H₂ and H I, into the nuclear region. The nuclear starbursts can be fed by preexisting molecular gas that falls into the central few hundred pc from an original radius of a few kpc, and not from the outer H I disk.

These ideas show that the kinematics of the nuclear gas is critical to understanding both the evolution of ultraluminous galaxies and the molecular line formation. The CO emissivity per unit gas mass surface density is not constant, but varies with position in the nuclear disk. A more correct treatment requires radiative transfer modeling, with kinematic data from millimeter interferometers.

To carry out this next step in our study of molecular gas disks at the centers of IR ultraluminous galaxies, we made high-resolution CO maps with the IRAM interferometer. We chose sources from our CO survey, concentrating on the nearest ultraluminous galaxies in the northern sky, for which we already had accurate measurements of the total flux, line width, and radial velocity. The new observations give accurate positions, line and continuum fluxes at the interferometer resolution, images, directions of the kinematic major axes, and radii of the nuclear disks.¹ These radii and the velocity extremes give the enclosed dynamical mass. The velocity data allow modeling of the kinematics

and the CO brightness temperature versus radius. For most sources, the CO data indicate that the gas kinetic temperature is higher than in typical Galactic molecular clouds, but the CO is subthermally excited, turbulent, and warm, quite unlike the molecular clouds in galaxy-scale disks. At the positions of maximum CO intensity in the disks, the CO lines are moderately opaque, with optical depth $\tau(1-0) \approx 4$ to 10, but in other parts of the disk the CO lines can be optically thin. The result is that the molecular gas mass is about a factor of 5 lower than it would be if the CO emission came from self-gravitating clouds. The rest of the dynamical mass is accounted for by young stars that provide the luminosity and older stars that were already in the central bulge before the merger.

We argue that the bright spots in the ultraluminous galaxies are compact extreme starburst regions that occur in the dense gas traced by HCN and CS emission. They produce most of the HCN luminosity and 1 mm dust continuum, while the more diffuse gas in the nuclear disks dominates the CO luminosity. These compact extreme starburst regions, which we identify in Arp 193, Arp 220, and Mrk 273, are the most prodigious star formation events in the local universe. There are undoubtedly many more too compact to be resolved.

The plan of this paper is as follows. Section 2 describes the observations and summarizes the parameters obtained by direct measurement. Section 3 introduces our model of a turbulent rotating disk and discusses the derivations of the rotation curve, disk radius, disk height, turbulent velocity, gas mass, and dynamical mass obtained by fitting the model disk to the data. Sections 4 through 8 present the results for the galaxies with CO (2–1) data, obtained with subarcsecond resolution. These galaxies are VII Zw 31, Mrk 231, Arp 193, Mrk 273, and Arp 220. Section 9 gives the results for five additional ultraluminous galaxies mapped in CO (1–0) only. Section 10 discusses the source sizes, gas masses, the ratio of gas mass to dynamical mass, and the mass of young stars needed to power the starburst. Section 11 presents our conclusions.

2. OBSERVATIONS AND RESULTS

CO (1–0) and (2–1) were observed with the IRAM interferometer on Plateau de Bure, France (Guilloteau et al. 1992). Three to four configurations of the four 15 m antennas gave baselines from 24 to 410 m for VII Zw 31, Mrk 231, Mrk 273, and Arp 220, and 24 to 288 m for the other sources. The SIS mixers had receiver temperatures of 60–80 K, and operated single-sideband at 3 mm and double-sideband at 1.3 mm, with system temperatures of 200 and 400 K, respectively. The spectral correlator covered a 500 MHz band at 2.5 MHz resolution, giving velocity ranges of 1300 km s⁻¹ at 7 km s⁻¹ resolution at 3 mm, and 700 km s⁻¹ at 3.4 km s⁻¹ resolution at 1.3 mm. For analysis, we smoothed the data to 20 and 40 km s⁻¹. Amplitude and phase were calibrated relative to quasars, and the flux scale was adopted from same-epoch measurements of quasars and planets with the interferometer and the IRAM 30 m telescope. The beam widths (FWHM) were 1" to 3" at CO (1–0) and 0".5 to 1" at CO (2–1). Table 1 summarizes the observing parameters.

Table 2 lists CO source positions and integrated CO line fluxes from the interferometer. We also list the CO line fluxes from the 30 m telescope (Radford, Solomon, & Downes 1991a; Solomon et al. 1997). Table 3 lists sizes from

¹ In this paper, distances are for $H_0 = 75 \text{ km s}^{-1} \text{ Mpc}^{-1}$ and $q_0 = 0.5$.

TABLE 1
OBSERVING PARAMETERS

| SOURCE NAME | DATE | FREQUENCY ^a (GHz) | PHASE CALIBRATOR | FLUX (Jy) | CLEAN BEAM | | FLUX SCALE (K Jy ⁻¹) |
|-------------------|-------------------|------------------------------|------------------|-----------|---------------|------------|----------------------------------|
| | | | | | Size (arcsec) | P.A. (deg) | |
| 00057 + 4021..... | 1994 Jun–Nov | 110.360 | 0003 + 380 | 0.5 | 2.2 × 1.1 | 47 | 40 |
| 02483 + 4302..... | 1994 Jun–Nov | 109.700 | 0234 + 285 | 1.4 | 2.2 × 1.7 | 0 | 27 |
| VII Zw 31 | 1996 Mar–May | 109.380 | 0355 + 508 | 2.6 | 1.4 × 0.8 | 58 | 88 |
| | 1996 Mar–May | 218.650 | 0355 + 508 | 1.0 | 0.7 × 0.4 | 46 | 78 |
| 10565 + 2448..... | 1994 Jun–Nov | 110.535 | 0923 + 392 | 5.5 | 2.3 × 1.4 | 25 | 32 |
| Mrk 231 | 1995 Nov–1996 Feb | 110.602 | 0923 + 392 | 4.4 | 1.3 × 1.1 | 0 | 70 |
| | 1995 Nov–1996 Feb | 221.204 | 0923 + 392 | 2.7 | 0.7 × 0.5 | 52 | 75 |
| Arp 193 | 1996 Jun–1998 Feb | 112.641 | 1308 + 326 | 1.5 | 1.3 × 0.9 | 37 | 83 |
| | 1997 May–1998 Feb | 225.282 | 1308 + 326 | 0.8 | 0.6 × 0.4 | 33 | 84 |
| Mrk 273 | 1996 Mar–1996 May | 111.076 | 1308 + 326 | 1.4 | 1.4 × 1.3 | 116 | 56 |
| | 1996 Mar–1996 May | 222.176 | 1308 + 326 | 0.7 | 0.6 × 0.6 | 0 | 66 |
| Arp 220 | 1995 Nov–1996 Mar | 113.228 | 3C 345 | 4.8 | 1.6 × 1.1 | 25 | 55 |
| | 1995 Nov–1996 Mar | 226.422 | 3C 345 | 2.4 | 0.7 × 0.5 | 28 | 69 |
| 17208 – 0014..... | 1994 Jun–1994 Oct | 110.535 | 1741 – 038 | 2.6 | 5.1 × 1.6 | 47 | 12 |
| 23365 + 3604..... | 1996 May–1996 Aug | 108.292 | 3C 454.3 | 5.0 | 3.9 × 2.5 | 45 | 11 |

^a The frequency is the zero of our velocity scales, not necessarily the CO line center.

Gaussian fits to the CO visibilities. Sources observed in CO (1–0) and (2–1) had the same sizes in both lines. The visibility fits are independent of the synthesized beam or the CLEAN algorithm, and there is no need to deconvolve an apparent size on a map. The phase calibration can broaden a source because of the baseline error, varying as $2\pi\lambda/D$ times the angle between the source and its phase calibrator (λ = wavelength, D = baseline). For sources and calibrators in this paper, the broadening is <0.1 beam width. After correcting for atmospheric decorrelation, we obtained sizes of $<0''.2$ for the quasar calibrator sources.

3. DISK MODELS

3.1. Geometry of Nuclear Disks from Kinematic Data

CO surveys of our Galaxy show that most of the gas in the inner $R < 5$ kpc is in ~ 6000 giant molecular clouds

(GMCs) of diameter ~ 50 pc, with H₂ density of 150 cm⁻³. In an ultraluminous IR galaxy merger, these clouds fall into the central $R \sim 500$ pc, forming a disk of height ~ 50 pc. Because the GMCs' density is too low to stabilize them against tidal shear at the merger's center, and because the new volume is 10 times smaller than the original volume of all the GMCs in the galactic disk, the GMCs loose their identity and blend into a continuous medium with a mean H₂ density of $\sim 10^3$ cm⁻³. We therefore modeled the nuclear disks as a continuous medium rather than an ensemble of individual clouds.

We used the CO spectral data to estimate how much of the gas was in a high-density inner ring or disk and how much was in a lower-density outer disk. To simulate the observed spectra and position-velocity diagrams, we modified a model for rotating disks developed by A. Dutrey (see

TABLE 2
CO POSITIONS AND FLUXES

| SOURCE NAME | CO LINE | R.A. (J2000) | DECL. (J2000) | CO FLUX | | CONTINUUM | |
|-------------------|---------|--------------|---------------|---|---|-----------------|------------|
| | | | | Interferometer (Jy km s ⁻¹) | 30 m Telescope (Jy km s ⁻¹) | Frequency (GHz) | Flux (mJy) |
| 00057 + 4021..... | (1–0) | 00 08 20.58 | +40 37 55.5 | 47 | 45 | 110 | <10 |
| 02483 + 4302..... | (1–0) | 02 51 36.01 | +43 15 10.8 | 28 | 25 | 109 | <10 |
| VII Zw 31 | (1–0) | 05 16 46.49 | +79 40 12.6 | 87 | 92 | 109 | <2 |
| | (2–1) | 05 16 46.53 | +79 40 12.4 | 135 | 280 | 219 | <10 |
| 10565 + 2448..... | (1–0) | 10 59 18.15 | +24 32 34.4 | 68 | 71 | 111 | <2 |
| Mrk 231 | (1–0) | 12 56 14.21 | +56 52 25.1 | 68 | 97 | 111 | 63 |
| | (2–1) | 12 56 14.22 | +56 52 25.1 | 276 | 280 | 221 | 36 |
| Arp 193 | (1–0) | 13 20 35.32 | +34 08 22.2 | 161 | 162 | 110 | <5 |
| disk | (2–1) | 13 20 35.32 | +34 08 22.2 | 360 | ... | 228 | 7 |
| SE core | (2–1) | 13 20 35.35 | +34 08 21.7 | 90 | ... | 228 | 3 |
| sum | (2–1) | ... | ... | 450 | 415 | 228 | 10 |
| Mrk 273 | (1–0) | 13 44 42.12 | +55 53 13.5 | 78 | 86 | 111 | 11 |
| disk | (2–1) | 13 44 42.10 | +55 53 13.4 | 197 | ... | 222 | <10 |
| core | (2–1) | 13 44 42.12 | +55 53 13.4 | 34 | ... | 222 | 8 |
| sum | (2–1) | ... | ... | 231 | ... | 222 | 8 |
| Arp 220 | (1–0) | 15 34 57.24 | +23 30 11.2 | 410 | 490 | 113 | 41 |
| west | (2–1) | 15 34 57.221 | +23 30 11.5 | 130 | ... | 229 | 90 |
| east | (2–1) | 15 34 57.29 | +23 30 11.3 | 220 | ... | 229 | 30 |
| disk | (2–1) | 15 34 57.24 | +23 30 11.2 | 750 | ... | 229 | 55 |
| sum | (2–1) | ... | ... | 1100 | 1100 | 229 | 175 |
| 17208 – 0014..... | (1–0) | 17 23 21.95 | –00 17 00.7 | 132 | 162 | 111 | <5 |
| 23365 + 3604..... | (1–0) | 23 39 01.25 | +36 21 08.4 | 30 | 47 | 108 | <5 |

NOTE.—Errors: For positions at CO (1–0), $\pm 0''.2$; at CO (2–1), $\pm 0''.1$; fluxes, $\pm 20\%$.

TABLE 3
MEASURED DIAMETERS OF THE INTEGRATED CO EMISSION

| Source Name | Angular Diameter (arcsec) | P.A. E of N (deg) | Angular Size Distance (Mpc) | Redshift cz_{lsr} (km s $^{-1}$) | Linear Scale (pc arcsec $^{-1}$) | Semimajor Axis (pc) | Semiminor Axis (pc) |
|-----------------------|---------------------------|-------------------|-----------------------------|--|-----------------------------------|---------------------|---------------------|
| 00057+4021 | 1.1 × <0.6 | -22 | 165 | 13390 | 802 | 440 | <240 |
| 02483+4302 | 1.8 × 1.7 | -4 | 188 | 15419 | 913 | 820 | 780 |
| VII Zw 31 | 2.4 × 2.1 | -5 | 196 | 16260 | 949 | 1140 | 1000 |
| 10565+2448 | 1.6 × 1.4 | -26 | 160 | 12923 | 776 | 620 | 540 |
| Mrk 231 | 0.9 × 0.8 | 77 | 157 | 12650 | 761 | 340 | 300 |
| Arp 193 disk | 2.8 × 0.8 | -40 | 90 | 7000 | 436 | 610 | 170 |
| Arp 193 SE core | 1.1 × 0.5 | -40 | 90 | 7000 | 436 | 240 | 100 |
| Mrk 273 tail | 3.1 × 2.8 | 5 | 142 | 11324 | 686 | 1060 | 960 |
| Mrk 273 disk | 0.9 × 0.6 | 18 | 142 | 11324 | 686 | 310 | 210 |
| Mrk 273 core | 0.35 × <0.2 | 76 | 142 | 11324 | 686 | 120 | <69 |
| Arp 220 disk | 2.0 × 1.6 | 50 | 70 | 5450 | 341 | 340 | 270 |
| Arp 220 west | 0.31 × 0.28 | -14 | 70 | 5340 | 341 | 53 | 48 |
| Arp 220 east | 0.9 × 0.9 | ... | 70 | 5650 | 341 | 150 | 150 |
| 17208-0014 | 1.8 × 1.6 | 7 | 159 | 12837 | 771 | 690 | 620 |
| 23365+3604 | 1.0 × 0.9 | -15 | 231 | 19330 | 1120 | 560 | 500 |

NOTE.—Diameters are FWHM from elliptical Gaussian fits to u, v data. Diameters, $\pm 0.^{\circ}2$; position angles, $\pm 10^{\circ}$.

Dutrey, Guilloteau, & Simon 1994). This model has an inner disk of high-density gas between radii R_{\min} and $R_1 = R_{\min} + \Delta R$, and an outer disk of lower density gas between radii R_{\min} and R_{\max} . The H₂ density between R_{\min} and R_{\max} is

$$n(R) = n_0 A \exp \left[-4 \ln 2 \left(\frac{R - R_{\min}}{\Delta R} \right)^2 \right] + n_0 R^\alpha, \quad (1)$$

where the inner disk is the Gaussian of width ΔR (FWHM), and the outer disk is the power law. We fit the outer disks with constant density ($\alpha = 0$). Our beams cannot distinguish between a ring and a filled disk, so for most sources, we took $R_{\min} = 0$. Because of the radiative transfer through the rotating inclined disk, the predicted CO map looks like a ring, even if there is gas in to $R = 0$. For the galaxies VII Zw 31, Arp 193, and IRAS 10565+2448, the position-velocity diagrams are better fitted with ring models, with $R_{\min} = R_0$, rather than filled disk models. Table 4 gives the source geometry, derived as follows:

1. *Line of nodes*: The visibility fits in individual spectral channels gave position offsets versus velocity, which showed

TABLE 4
DISK SIZES FROM POSITION-VELOCITY DATA

| Source Name | Linear Scale (pc arcsec $^{-1}$) | R_0^{a} (pc) | R_1^{b} (pc) | R_{\max}^{c} (pc) | H^{d} (pc) |
|--------------------|-----------------------------------|-----------------------|-----------------------|----------------------------|---------------------|
| 00057+4021 | 802 | 240 | 480 | 1000 | 50 |
| 02483+4302 | 913 | 270 | 730 | 1400 | 54 |
| VII Zw 31 | 949 | 290 | 1100 | 3300 | 58 |
| 10565+2448 | 776 | 230 | 700 | 1600 | 47 |
| Mrk 231 | 761 | 75 | 460 | 1100 | 23 |
| Arp 193 disk | 436 | 220 | 740 | 1300 | 65 |
| Mrk 273 disk | 686 | 70 | 400 | 1900 | 42 |
| Arp 220 disk | 341 | 200 | 480 | 1400 | 80 |
| Arp 220 west | 341 | 35 | 68 | ... | 68 |
| Arp 220 east | 341 | 50 | 110 | ... | 80 |
| 17208-0014 | 771 | 310 | 540 | 1500 | 62 |
| 23365+3604 | 1120 | 340 | 670 | 2200 | 67 |

^a Rotation curve turnover radius.

^b Half-power radius.

^c Outer disk boundary.

^d Disk thickness H is FWHM perpendicular to the equator.

the direction of the kinematic major axis. We checked the angle of the line of nodes from channel maps and isovelocity contour maps. Errors are $\pm 10^{\circ}$.

2. *Rotation curve turnover radius R_0* : In the data, the position-velocity diagrams along the kinematic major axis often have two peaks near the source center. In our models, twin peaks occur near the points where the rotation curve turns over and becomes flat. The observed offsets of the two intensity peaks on the major axis were tried as first guesses for the rotation curve turnover radii R_0 . Model fits converged close to these values. In angular units, the uncertainties are $\sim \pm 0.^{\circ}1$. In our models, R_0 is the projected radius with the largest gas column density at the same line-of-sight velocity and the highest flux. For most of the sources, the solid angle inside this zone is too small to affect the maps, even if the gas is really in a filled disk rather than a ring.

3. *Inner disk half-intensity radius $R_1 = R_{\min} + \Delta R$* : In our models, most of the CO flux comes from the high-density inner disk. The extent of the central double peak in the position-velocity diagrams constrained the radial width ΔR , which we varied until the model position-velocity diagrams matched the data. The uncertainty in ΔR is $\sim \pm 0.^{\circ}2$.

4. *Outer radius, R_{\max} , of the low-density disk*: This was taken to be the observed CO maximum extent on the line of nodes.

5. *Disk thickness, H* : Along the z -axis perpendicular to the equatorial plane, the gas volume density $n(z)$ near $z = 0$ was approximated by a Gaussian with FWHM H . For a disk with a flat rotation curve, the disk thickness can be estimated with the Mestel formula (Mestel 1963; see also Binney & Tremaine 1987):

$$H(R) = 1.4 \sigma(R) \left(\frac{R}{V_{\text{rot}}} \right) \left[1 + \frac{\rho_{\text{gas}}}{\rho_1} \left(1 - \frac{H}{2R} \right) \right]^{-0.5}, \quad (2)$$

where σ is the one-dimensional velocity dispersion (assumed to be independent of z), and $\rho_1(R)$ is the total mass density (gas plus stars) in an equivalent sphere with a flat rotation curve. This equivalent density, in M_{\odot} pc $^{-3}$, is related to the rotation velocity, in km s $^{-1}$, through the usual integral for dynamical mass, $\rho_1(R) = 18.5(V_{\text{rot}}/R)^2$. We dropped the second-order term and estimated the disk

thickness as

$$H \approx 1.4 \sigma(R) \left(\frac{R}{V_{\text{rot}}} \right) \left[1 + \frac{\rho_{\text{gas}}}{18.5} \left(\frac{R}{V_{\text{rot}}} \right)^2 \right]^{-0.5}, \quad (3)$$

where H and R are in pc, V_{rot} is in km s^{-1} , and ρ_{gas} is in $M_{\odot} \text{ pc}^{-3}$. Because the velocity dispersion decreases with distance from the center, our model disk thickness tends to a constant value. In reality, the molecular disks are warped and twisted, and their shape depends on the merger's infall history.

3.2. Rotation Curves

We combined our density models with rotation curves that reproduced the observed channel maps, position-velocity diagrams, spectral profiles, interferometer visibilities, and line intensities. We took the rotation velocity to be

$$V_{\text{rot}}(R) = V_0 \left(\frac{R}{R_0} \right)^{\beta}, \quad (4)$$

where $\beta = 1$ for $R < R_0$ and $\beta = 0$ for $R_0 \leq R \leq R_{\text{max}}$; that is, the curve rises from the center and flattens after R_0 . Most of the derived values of R_0 are smaller than our beam, so more elaborate rotation curves are not justified for now.

For the inclination, i , we started from the major/minor axis ratio of the integrated CO source, with $i = \cos^{-1}$ (minor/major), and then varied the inclination to match the position-velocity data and to ensure that the derived gas mass was less than the dynamical mass. The nuclear rings or disks may not be circular; they might be elliptical, analogous to x_2 orbits at the center of a barred galaxy. The inclination i listed in Table 5 should be interpreted in the sense $\sin i = \sin I \cos \phi$, where I is the true inclination of the disk relative to face-on, and ϕ is the azimuth of the major axis of the ellipse, if there is one. With our current beams, we cannot tell the difference between circular and elliptical orbits.

For the rotation velocity, V_0 , we first guessed the apparent speed, $V_0 \sin i$, to be half the velocity range of the twin

CO peaks on the major axis. The best fits were close to these values, giving 200–300 km s^{-1} (corrected for inclination) on the flat part of the curve (Table 5). This is an equivalent circular velocity if the orbits are elliptical.

The turbulent velocity, ΔV , of the gas was taken from the model fit, not from the observed line profiles, which include both turbulent broadening and the rotational velocity gradient in the beam. Rotation alone cannot explain the observed profiles. We need a local, turbulent line broadening as well. The models actually constrain this parameter rather well. We assumed that the local line broadening had the form

$$f(V - V_0) = \exp \left[-\left(\frac{V - V_0}{\Delta V} \right)^2 \right], \quad (5)$$

where ΔV is the local line half-width to the $1/e$ level ($\Delta V = 0.6 \times \text{FWHM} = 1.4 \sigma$, where σ is the rms velocity dispersion along the line of sight). The radiative transfer model included the local line width at each point and the rotational velocity versus radius. We iterated the model fits until the local turbulence and the rotational velocity gradient, convolved with our beam, matched the observed position-velocity diagrams and the observed line profiles. Turbulent velocities ΔV that fit the data were 30–140 km s^{-1} , with some of the position-velocity diagrams indicating lower turbulence at greater radii from the nucleus. At the rotation curve turnover point R_0 , the values of ΔV correspond to local FWHM line widths of 70–230 km s^{-1} , so the nuclear disks are highly turbulent.

3.3. CO Line Parameters

After deriving sizes and velocities from the data, we adjusted our models to match the observed CO line intensities. As a first guess, we set the gas kinetic temperature to be equal to the dust temperature derived from blackbody fits to the *IRAS* fluxes. At the gas densities in our models, collisions cannot raise the CO excitation temperature to the gas kinetic temperature, nor populate the CO levels ther-

TABLE 5
ROTATION CURVES FROM POSITION-VELOCITY DATA

| SOURCE NAME | DATA | | MODEL | | |
|--------------------|--|---|----------------|--|--|
| | Line of Nodes E of N, P.A. (deg) | $V_{\text{rot}} \sin i^a$ (km s^{-1}) | i^b (deg) | V_{rot}^c (km s^{-1}) | ΔV^d (km s^{-1}) |
| 00057+4021..... | 135 | 75 | 20 | $250r^{\beta}$ | $100r^{-0.5}$ |
| 02483+4302..... | 0 | 70 | 15 | $270r^{\beta}$ | $40r^{0.0}$ |
| VII Zw 31 | 0 | 100 | 20 | $290r^{\beta}$ | $30r^{0.0}$ |
| 10565+2448..... | 100 | 75 | 20 | $220r^{\beta}$ | $40r^{0.0}$ |
| Mrk 231 | 90 | 60 | 10 | $345r^{\beta}$ | $60r^{-0.3}$ |
| Arp 193 disk | 140 | 175 | 50 | $230r^{\beta}$ | $40r^{0.0}$ |
| Mrk 273 disk..... | 90 | 200 | 45 | $280r^{\beta}$ | $140r^{0.0}$ |
| Arp 220 disk | 40 | 212 | 40 | $330r^{\beta}$ | $140r^{-0.2}$ |
| Arp 220 west | 300 | 103 | 20 | $300r^{\beta}$ | $100r^{-0.3}$ |
| Arp 220 east..... | 50 | 300 | 60 | $350r^{\beta}$ | $100r^{-0.3}$ |
| 17208-0014..... | 120 | 130 | 30 | $260r^{\beta}$ | $150r^{-0.2}$ |
| 23365+3604..... | 135 | 130 | 30 | $260r^{\beta}$ | $100r^{-0.2}$ |

^a Apparent rotation.

^b Inclination, 0° = face-on.

^c V_{rot} = rotation velocity. For the model rotation curve, $\beta = 1$ for $r < 1$ and $\beta = 0$ for $r \geq 1$; $r = R/R_0$, where R_0 is the rotation curve turnover radius (see Table 4).

^d Turbulent velocity ΔV = half-width to the $1/e$ level. $\Delta V = 0.6 \text{ FWHM} = 1.4 \sigma$, where σ is the one-dimensional velocity dispersion. Turbulent velocities are valid for $R_0 \leq R \leq R_{\text{max}}$ (see Table 4).

mally. Instead, there are different excitation temperatures for each transition. The line brightness temperatures, excitation temperatures, and gas kinetic temperatures are in the sense $T_b < T_{\text{ex}} < T_{\text{kin}}$, with $T_{\text{ex}}(2-1) < T_{\text{ex}}(1-0)$. We therefore assumed the CO level populations to be determined by the local gas kinetic temperature, density, and velocity gradient, and we calculated, with an escape probability program, CO column densities per unit velocity width for a local velocity gradient of $1 \text{ km s}^{-1} \text{ pc}^{-1}$ and a $[\text{CO}/\text{H}_2]$ abundance of 8×10^{-5} , both typical of Milky Way molecular clouds. For these values, the escape probability method yields the following non-LTE excitation temperatures T_{ex} :

$$T_{\text{ex}}(1-0) = 0.186 n^{0.622} T_{\text{kin}}^{0.240} \quad (6)$$

$$T_{\text{ex}}(2-1) = 0.117 n^{0.678} T_{\text{kin}}^{0.247}, \quad (7)$$

where n is the H_2 number density in cm^{-3} , and T_{kin} is the gas kinetic temperature in K. These formulae are valid for $50 \text{ K} < T_{\text{kin}} < 150 \text{ K}$ and $100 \text{ cm}^{-3} < n < 3000 \text{ cm}^{-3}$.

We then calculated the radiative transfer on the lines of sight through the disk (see eqs. [7] and [8] of Dutrey et al. 1994), convolved the computed map with our beam, and adjusted the parameters to match the observed brightness temperatures. The highest CO opacity occurs at the rotation curve turnover radius, R_0 , which yields the largest column density at the same line-of-sight velocity. Table 6 gives the best-fit model CO (1-0) excitation temperatures and gas densities, and Tables 7 and 8 give the model CO (1-0) and (2-1) line opacities and Rayleigh-Jeans brightness temperatures. We also ran models for higher density gas, with excitation temperatures closer to the kinetic temperatures, but these models gave too much CO and dust flux, and did not reproduce the position-velocity diagrams.

At the rotation curve turnover radius R_0 , our models yield CO (1-0) opacities of 2–8. These mean opacities apply to smoothly distributed gas. The model of subthermal excitation yields the observed CO (2-1)/(1-0) ratios of 0.6–1.0 (Radford et al. 1991a). In the lower density outer disks detected in these sources, the volume-averaged densities in the model are too low to yield detectable CO lines. For these outer disks, our model must be corrected with an area filling factor for molecular clouds, as in CO maps of disks of normal galaxies. For the mean values for the outer disks in

TABLE 6
MODEL TEMPERATURES AND DENSITIES

| Source Name | Gas Kinetic Temperature ^a (K) | $\langle n(\text{H}_2) \rangle^b$ at R_0 (cm^{-3}) | $\langle n(\text{H}_2) \rangle^b$ Outer Disk (cm^{-3}) |
|--------------------|---|---|---|
| 00057 + 4021 | $72r^{-0.5}$ | 400 | 40 |
| 02483 + 4302 | $50r^{-0.5}$ | 250 | 20 |
| VII Zw 31 | $50r^{-0.5}$ | 450 | 10 |
| 10565 + 2448 | $60r^{-0.5}$ | 1200 | 30 |
| Mrk 231 | $100r^{-0.5}$ | 3600 | 60 |
| Arp 193 disk | $40r^{-0.5}$ | 550 | 10 |
| Mrk 273 disk | $70r^{-0.5}$ | 1800 | 60 |
| Arp 220 disk | $64r^{-0.5}$ | 900 | 30 |
| Arp 220 west | $150r^{-0.5}$ | 22000 | 900 |
| Arp 220 east | $100r^{-0.5}$ | 20000 | 900 |
| 17208 – 0014 | $70r^{-0.5}$ | 600 | 60 |
| 23365 + 3604 | $67r^{-0.5}$ | 200 | 20 |

^a In the scaling laws, $r = R/R_0$ where R_0 is the turnover radius of the rotation curve (see Table 4). At large radii, we adopted minimum gas kinetic temperatures of 10 K.

^b Gas densities $\langle n(\text{H}_2) \rangle$ are averaged over the inner and outer disk volumes.

Table 6, we adopted a volume filling factor of 0.1, an area filling factor of 0.3, and local gas densities 10 times higher than the volume-averaged values listed in the table.

3.4. Gas Mass and Dynamical Mass

We used the CO parameters to estimate the gas mass and the dynamical mass versus radius (Table 9). After we found a density law that reproduced the observed brightness temperatures, we integrated over the source to get the gas mass. These masses are for a $[\text{CO}/\text{H}_2]$ abundance of 8×10^{-5} , as in molecular clouds in our Galaxy. For the sources observed here, it is difficult to lower the model CO abundance below the Milky Way value. Keeping the same CO line intensity at a lower CO abundance would force us to make the gas mass larger than the dynamical mass, invalidating the model.

The dynamical masses were taken to be RV_{rot}^2/G , where V_{rot} is the rotation speed listed in Table 5. Most of the sources have flat rotation curves, so the dynamical mass increases linearly with radius. Table 9 lists the ratio of gas mass to dynamical mass in the inner high-density disk alone

TABLE 7
CO (1-0) LINE PARAMETERS

| SOURCE NAME | MODEL | | BEAM FWHM AT R_0 (arcsec) | T_b IN BEAM | |
|--------------------|---------------------------------|------------------------|-----------------------------------|------------------------|----------------------|
| | CO (1-0) Opacity at R_0 | True T_b at R_0 | | Predicted/Model (K) | Observed/Data (K) |
| 00057 + 4021 | 4.8 | 16 | 2.2×1.1 | 2.7 | 2.4 |
| 02483 + 4302 | 9.7 | 11 | 2.2×1.7 | 1.9 | 1.4 |
| VII Zw 31 | 7.8 | 18 | 1.4×0.8 | 7.2 | 7.4 |
| 10565 + 2448 | 9.8 | 36 | 2.3×1.4 | 4.6 | 4.5 |
| Mrk 231 | 3.4 | 56 | 1.3×1.1 | 13.5 | 14.0 |
| Arp 193 disk | 9.9 | 25 | 1.7×1.6 | 5.0 | 6.9 |
| Mrk 273 disk | 3.7 | 36 | 1.4×1.3 | 4.8 | 4.5 |
| Arp 220 disk | 5.9 | 29 | 1.6×1.1 | 10.2 | 10.2 |
| Arp 220 west | ... | 50 | 1.6×1.1 | 10 | ... |
| Arp 220 east | ... | 50 | 1.6×1.1 | 10 | ... |
| 17208 – 0014 | 3.9 | 21 | 5.1×1.6 | 2.5 | 2.2 |
| 23365 + 3604 | 6.0 | 10 | 3.9×2.5 | 1.0 | 0.8 |

NOTE.—Model CO abundance: $X_{\text{CO}}/(dv/dr) = 8 \times 10^{-5}$. All brightness temperatures are Rayleigh-Jeans.

TABLE 8
CO (2–1) LINE PARAMETERS

| SOURCE NAME | MODEL | | | T_b IN BEAM | | |
|--------------------|---------------------------------|-------------------------------|--------------------------|------------------------|----------------------|--------------------------------|
| | CO (2–1) Opacity at R_0 | True T_b at R_0 (K) | BEAM FWHM (arcsec) | Predicted/Model (K) | Observed/Data (K) | CO (2–1)/(1–0) IN 3 mm BEAM |
| VII Zw 31 | 25 | 12 | 1.1×0.8 | 5.4 | 5.4 | 0.7 ± 0.2 |
| Mrk 231 | 12 | 51 | 0.7×0.5 | 30.3 | 28.5 | 1.0 ± 0.2 |
| Arp 193 disk | 54 | 13 | 0.7×0.6 | 8.2 | 8.1 | 0.5 ± 0.2 |
| Mrk 273 disk..... | 11 | 34 | 0.6×0.6 | 14 | 6.6 | ... |
| Arp 220 disk | 15 | 23 | 0.7×0.5 | 16.6 | 10.0 | 0.6 ± 0.2 |
| Arp 220 west | 17 | 53 | 0.7×0.5 | 18.8 | 17.0 | ... |
| Arp 220 east..... | 9 | 70 | 0.7×0.5 | 9.5 | 9.1 | ... |

NOTE.—Model CO abundance: $X_{\text{CO}}/(dv/dr) = 8 \times 10^{-5}$. All brightness temperatures are Rayleigh-Jeans.

(to radius R_1 in Table 4) and in the inner and outer disks together (to radius R_{\max} in Table 4). Relative to our assumed Hubble constant, the gas mass scales as H_0^{-2} , the dynamical mass as H_0^{-1} , and their ratio as H_0^{-1} .

We also list in Table 9 the maximum ratio of gas to total (gas + stars) surface density in our models. We calculated the ratio of gas to total mass surface density, μ/μ_{tot} , in 15 bins in radius, and found maximum values of $\sim 1/3$ to $1/4$, midway between the rotation curve turnover radius R_0 and the half-intensity radius R_1 . The models in this paper are for the distributed gas, but there is also denser gas in star-forming cores that give rise to HCN and CS lines. Most of the CO flux comes from the distributed medium, but our gas masses may have to be corrected upward to allow for the cores, depending on future interferometer results in the dense-gas tracer lines. We return to this point in § 10.

3.5. Dust Continuum Flux

We used the model gas mass to predict the dust flux, from

$$S(v_{\text{obs}}) = (1 + z)\kappa(v_r)MD_L^{-2}B(v_r, T_d), \quad (8)$$

where S is the dust continuum flux density, v_{obs} and v_r are the observed and rest-frame frequencies, M is the gas mass, D_L is the luminosity distance, B is the Planck function, and T_d is the dust temperature. We took the dust temperatures from our fits to the *IRAS* fluxes (Solomon et al. 1997), as for the gas temperatures in Table 6, and we used a dust mass absorption coefficient $\kappa(v_r) = 0.1 \times v^n$, where v_r is in THz, κ is in $\text{cm}^2 \text{ gm}^{-1}$ of interstellar matter, and we took the index $n = 1.5$. At 230 GHz, this absorption coefficient is $\kappa = 0.011 \text{ cm}^2 \text{ gm}^{-1}$ of interstellar matter, or, for a gas-to-dust mass ratio of 100, $\kappa_d = 1.1 \text{ cm}^2 \text{ gm}^{-1}$ of dust, as in previous

TABLE 9
CO (1–0) LUMINOSITY, GAS MASS, AND DYNAMICAL MASS

| Source Name | Radius (pc) | L'_{CO} ($10^9 L_\odot$) | M_{gas} ($10^9 M_\odot$) | $M_{\text{gas}}/L'_{\text{CO}}$ (M_\odot/L_\odot) | M_{dyn} ($10^9 M_\odot$) | Mass Ratio ($M_{\text{gas}}/M_{\text{dyn}}$) | μ/μ_{tot} (max) |
|-----------------------------|----------------|--|--|--|--|---|---------------------------------|
| 00057+40 to R_1 | 480 | 2.3 | 0.6 | 0.3 | 7.0 | 0.09 | 0.31 |
| to R_{\max} | 1000 | 4.0 | 1.4 | 0.4 | 14.5 | 0.10 | ... |
| 02483+43 to R_1 | 730 | 2.0 | 1.2 | 0.6 | 12.4 | 0.10 | ... |
| to R_{\max} | 1400 | 3.2 | 1.9 | 0.6 | 23.6 | 0.08 | ... |
| VII Zw 31 to R_1 | 1100 | 3.2 | 3.0 | 0.9 | 21.5 | 0.14 | 0.22 |
| to R_2 | 1900 | 5.5 | 5.2 | 1.0 | 37.3 | 0.14 | ... |
| to R_{\max} | 3670 | 8.5 | 8.3 | 1.0 | 71.5 | 0.12 | ... |
| 10565+24 to R_1 | 700 | 2.3 | 1.8 | 0.8 | 7.8 | 0.23 | 0.28 |
| to R_2 | 1150 | 3.4 | 3.0 | 0.9 | 13.1 | 0.23 | ... |
| to R_{\max} | 1600 | 5.5 | 4.0 | 0.7 | 17.4 | 0.23 | ... |
| Mrk 231 to R_1 | 460 | 2.8 | 1.8 | 0.7 | 12.7 | 0.14 | 0.20 |
| to R_2 | 850 | 4.2 | 3.1 | 0.7 | 23.1 | 0.13 | ... |
| to R_{\max} | 1700 | 5.1 | 4.0 | 0.8 | 31.5 | 0.13 | ... |
| Arp 193 to R_1 | 740 | 1.4 | 1.7 | 0.8 | 9.1 | 0.19 | ... |
| to R_2 | 1100 | 2.1 | 2.6 | 0.8 | 15.0 | 0.16 | ... |
| to R_{\max} | 1300 | 2.6 | 3.4 | 0.9 | 16.1 | 0.21 | ... |
| Mrk 273 to R_1 | 400 | 4.1 | 2.1 | 0.5 | 8.7 | 0.24 | 0.28 |
| to R_2 | 900 | 4.6 | 2.7 | 0.6 | 16.2 | 0.17 | ... |
| to R_{\max} | 1900 | 5.6 | 5.6 | 1.0 | 34.6 | 0.16 | ... |
| Arp 220 west..... | 68 | 0.6 | 0.6 | 1.0 | 1.4 | 0.43 | ... |
| Arp 220 east | 150 | 0.8 | 1.1 | 1.3 | 3.2 | 0.35 | ... |
| Arp 220 disk to R_1 | 480 | 2.7 | 2.0 | 0.8 | 12.1 | 0.17 | 0.30 |
| Arp 220 disk to R_2 | 760 | 3.7 | 3.0 | 0.8 | 19.2 | 0.16 | ... |
| Arp 220 total | 1360 | 5.9 | 5.2 | 0.9 | 34.5 | 0.15 | ... |
| 17208–00 to R_1 | 540 | 3.3 | 2.4 | 0.7 | 8.5 | 0.28 | ... |
| to R_{\max} | 1500 | 5.8 | 6.1 | 1.0 | 23.5 | 0.26 | ... |
| 23365+36 to R_1 | 670 | 3.0 | 1.5 | 0.5 | 10.5 | 0.14 | ... |
| to R_{\max} | 2200 | 5.4 | 3.8 | 0.7 | 34.5 | 0.11 | ... |

NOTE.— $L_l \equiv K \text{ km s}^{-1} \text{ pc}^2$; μ = gas ($\text{H}_2 + \text{He}$) surface density in $M_\odot \text{ pc}^{-2}$; μ_{tot} = gas + stars; μ/μ_{tot} = peak ratio in the disk. $R_1 = R_{\min} + \Delta R$ is the inner disk's half-power radius, $R_2 = R_{\min} + 2\Delta R$ is the zero-power radius, and R_{\max} is the boundary of the outer disk (see eq. [1] and Table 4).

TABLE 10
CONTINUUM EMISSION

| SOURCE NAME | 2.6 mm | | 1.3 mm | | INTERPRETATION OF OBSERVED FLUX AT 13 mm ^a |
|---------------------|---------------------------------|---------------------------------|---------------------------------|---------------------------------|---|
| | Predicted Dust Flux (mJy) | Observed Total Flux (mJy) | Predicted Dust Flux (mJy) | Observed Total Flux (mJy) | |
| 00057+4021 | 0.9 | <10 | 10.1 | ... | ... |
| 02483+4302 | 0.6 | <10 | 6.1 | ... | ... |
| VII Zw 31 | 0.9 | <2 | 17.0 | <20 | ... |
| 10565+2448 | 2.2 | <2 | 24.9 | ... | ... |
| Mrk 231 | 2.4 | 63 | 7.0 | 36 | 80% nt, 20% d |
| Arp 193 | 3.8 | <5 | 39 | 10 | >90% d |
| Mrk 273 core | 1.5 | 11 | 16 | 8 | 50% nt, 50% d |
| Arp 220 west | 6.3 | ... | 71 | 90 | 10% nt, 10% ff, 80% d |
| Arp 220 east | 2.3 | ... | 25 | 30 | 10% nt, 10% ff, 80% d |
| Arp 220 disk | 4.8 | ... | 54 | 55 | 10% nt, 90% d |
| Arp 220 total | 13.4 | 41 | 150 | 175 | 15% nt, 5% ff, 80% d |
| 17208-0014 | 3.5 | 5 | 40 | ... | ... |
| 23365+3604 | 1.0 | <5 | 11 | ... | ... |

NOTE.—Predicted fluxes are for the temperatures given in Table 6 and a dust emissivity index of 1.5.

^a Errors in observed fluxes are $\pm 20\%$; nt = nonthermal, ff = free-free, d = dust.

estimates for dense molecular clouds (see Fig. 12 of Krügel & Siebenmorgen 1994). The predicted thermal fluxes from dust are then

$$S(v_{\text{obs}}) = 6.4 \times 10^{-7} (1+z) M D_L^{-2} T_d v_r^{2+n}, \quad (9)$$

where flux density S is in Jy, gas mass M is in M_\odot , luminosity distance D_L is in Mpc, dust temperature T_d is in K, and rest frequency v_r is in THz. The predicted thermal dust fluxes at 2.6 and 1.3 mm are compared with the observed fluxes in Table 10.

Four sources, VII Zw 31, Mrk 231, Mrk 272, and Arp 220, were observed in both the CO (1-0) and (2-1) lines, and on the longest baselines of 410 m. Because we have better angular resolution for these sources, we discuss them in more detail than our other sources.

4. VII ZWICKY 31

This source, catalogued by Zwicky (1971), was identified by Fairclough (1986) as an ultraluminous IR galaxy. Its optical surface brightness profiles resemble those of elliptical galaxies, and its optical line ratios fit a starburst rather than an AGN (Djorgovski, de Carvalho, & Thompson 1990). Sage & Solomon (1987) found that this source had one of the highest known CO luminosities, and deduced that the molecular gas was a large part of the dynamical mass. Scoville et al. (1989) showed that the CO source had a radius of < 3.8 kpc.

The CO maps of the galaxy VII Zw 31 are the best evidence in our sample for a rotating ring. Models that best fit the data are those with a minimum ring radius R_{\min} in equation (1) equal to $R_0 = 290$ pc. Filled-disk models, with $R_{\min} = 0$, give poorer fits, with much less contrast. In 40 km s⁻¹ wide channel maps, the CO peak migrates from south to north with increasing velocity (Fig. 1). The source is resolved east-west, perpendicular to the kinematic major axis. This indicates that the source is inclined, but more face-on than edge-on. Our modeling gives a good fit to the data for a ring inclined at 20° to face-on. Figure 2 shows the maps of integrated intensity and isovelocitity contours across the source in both CO lines. The total CO (1-0) flux measured with the interferometer is equal to the flux obtained at the 30 m telescope (Radford et al. 1991a). At CO (2-1), the

source is partially resolved out, and the flux from the interferometer is only half the single-dish flux. In channels off the CO line, the continuum flux is < 2 mJy at 109 GHz and < 10 mJy at 221 GHz. This limit on any thermal dust flux is consistent with the gas mass of 1.1×10^{10} deduced from the CO luminosity, for a dust temperature of < 50 K.

The CO velocity contours shown in Figure 2 indicate the north-south velocity gradient. In the position-velocity diagrams (Fig. 3), there is a 200 km s⁻¹ velocity shift over 4" north-south. The model in the tables reproduces well the observed diagrams, the CO profiles across the source, the channel maps, and the observed line intensities. The CO spectra (Fig. 4) have twin peaks separated by ± 70 km s⁻¹. The blue- and redshifted CO peaks are 0'65 south and north of the source centroid, respectively. The line profiles are remarkably symmetric along the north-south kinematic major axis. The CO line of nodes differs from the northwest-southeast dust lane found by Djorgovski et al. (1990) on a 10" scale by subtracting a model from their optical images.

5. MARKARIAN 231

The Seyfert 1 galaxy Mrk 231 has an IR luminosity of $3.3 \times 10^{12} L_\odot$ (e.g., Sanders et al. 1987). Most of the power is emitted at the center of a major galaxy merger that has tidal tails extending over 75 kpc (Cutri, Rieke, & Lebofsky 1984; Hutchings & Neff 1987; Sanders et al. 1987). Optical spectroscopy indicates the presence of stars formed in the past 1 Gyr over a widespread region (10–15 kpc). In this large extranuclear region, the H α emission comes from shocks rather than stellar photoionization (e.g., Hamilton & Keel 1987; Lipari, Colina, & Macchetto 1994). The best previous CO study is that of Bryant & Scoville (1996), who found an east-west velocity gradient in the CO source. Our higher sensitivity results have a factor of 2 better resolution than their study, and not only confirm the velocity gradient, but also distinguish the inner and outer disks in the position-velocity diagrams.

5.1. CO in Mrk 231 Molecular Disk

In contrast to the large optical extent, the CO source is very compact, on a scale 20 times smaller in radius. In 40 km s⁻¹ channel maps in CO (1-0) and (2-1), the line peak

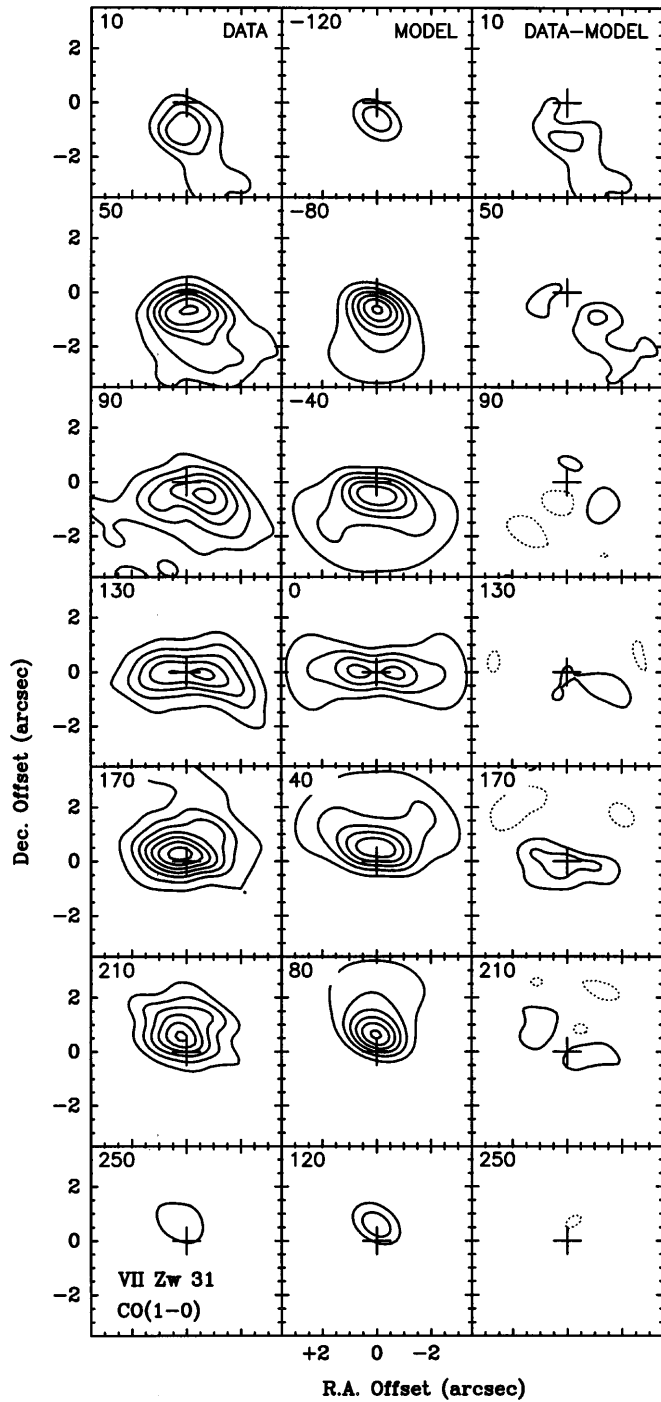


FIG. 1.—VII Zw 31. *Left column:* CO (1–0) in 40 km s⁻¹ channels. Radial velocities (km s⁻¹, upper left of each box) are relative to 109.380 GHz ($cz_{ls} = 16147$ km s⁻¹). Contour unit is 11 mJy beam⁻¹, with $T_b/S = 88$ K Jy⁻¹. The beam is $1.^{\circ}4 \times 0.^{\circ}8$. The cross at (0, 0) is $05^{\circ}16'46\overset{.}{.}51, 79^{\circ}40'12\overset{.}{.}8$ (J2000). *Middle column:* Maps from the model, with the same contours and resolution as the data. *Right column:* Data minus the model, with the same contour unit.

shifts from west to east with increasing velocity (Fig. 5). The gradient is clearly shown on the CO isovelocity maps (Fig. 6). The CO (2–1) intensity contours (Fig. 6) are symmetric and only slightly broader than the beam. The CO (2–1) position-velocity diagram along the line of nodes (Fig. 7) shows an inner nuclear disk of diameter $1.^{\circ}2$ (radius 460 pc) and a $3''$ outer disk with a lower velocity gradient. The asymmetric CO (2–1) line profiles $0.^{\circ}4$ from the center of the galaxy (Fig. 8) are a characteristic signature of a rotating

nuclear disk. The maximum line width in both CO lines is 190 km s⁻¹ FWHM, which is narrow for ultraluminous galaxies.

The CO data imply that the molecular disk is face-on, for three reasons. (1) The CO major and minor axes are nearly equal, indicating an inclination $i \leq 20^\circ$. (2) To reproduce the single-peaked CO profile, narrow CO line width, and observed velocity gradients, our model disks must be within 20° of face-on. For $i \geq 20^\circ$ to face-on, the gas mass would exceed the dynamical mass. (3) The CO does not absorb the nuclear continuum source at any velocity. This agrees with the CO disk being face-on, leaving the Seyfert 1 nucleus unobscured. For $i = 10^\circ$ to face-on, the true rotation velocity would be 345 km s⁻¹, the same as we deduce for Arp 220. If the disk were even more face-on, the observed velocity gradient would imply a rotation speed of >400 km s⁻¹, higher than in all the other galaxies in our sample, which seems unlikely. We adopt $i = 10^\circ$ and $V_{\text{rot}} = 345$ km s⁻¹, although the kinematic data alone would also allow a rotation velocity of 250 km s⁻¹.

In CO, we do not detect the gas being emitted in the 1667 MHz OH megamaser with the 760 km s⁻¹ line width (Staveley-Smith et al. 1987), nor do we detect anything at the IR source $3.^{\circ}5$ south of the nucleus, to a limit of 5 mJy in 40 km s⁻¹ channels (see also Bryant & Scoville 1996). Armus et al. (1994) interpreted the southern IR source as the nucleus of the merger partner, but recent *HST* images show this feature to be a dense arc of star-forming knots (Surace et al. 1998). In any case, it is very weak in both CO and the millimeter continuum.

In the center of Mrk 231, the AGN is detected by centimeter-wavelength VLBI as a variable, nonthermal radio continuum source with a size of <1 pc (Preuss & Fosbury 1983; Neff & Ulvestad 1988; Lonsdale, Smith, & Lonsdale 1993; Taylor et al. 1994). New VLBA images at 1.4 GHz resolve this nonthermal source into a nuclear core with parsec-scale lobes. Carilli, Wrobel, & Ulvestad (1998) subtracted their VLBA map from a VLA map and found a $0.^{\circ}4$ nonthermal nuclear disk source that emits half the nuclear flux, the rest coming from the core and the parsec-scale lobes.

At millimeter wavelengths, outside the CO line channels, we detect an unresolved (size $<0.^{\circ}1$) nonthermal, millimeter-continuum source at the nucleus, which is probably the nonthermal VLBA core. The millimeter-continuum source and the CO centroid both coincide with the 8.44 GHz continuum source (Condon et al. 1991).

5.2. Mrk 231 Luminosity: 2/3 Starburst, 1/3 AGN

The CO kinematic data for the central 1 kpc of Mrk 231 and our model of a face-on disk show that the FIR luminosity comes from a starburst, not a black hole accretion disk. We assume that the central UV-to-FIR continuum has three components; the visible and UV continuum is blackbody flux from the AGN accretion disk, the $2 \mu\text{m}$ peak is blackbody flux from a dusty AGN torus, and the FIR peak is blackbody flux from the molecular disk. The extinction to the accretion disk is low, $A_V = 2$ mag, because both the dusty torus and the larger scale molecular disk are face-on.

The accretion disk's luminosity can be derived from the UV and visible fluxes and the extinction to the Seyfert 1 nucleus. The UV fluxes measured by *IUE* and *HST* are 2×10^{-15} ergs s⁻¹ cm⁻² Å⁻¹ (Schmidt & Miller 1985; Hutchings & Neff 1987; Smith et al. 1995). A blackbody

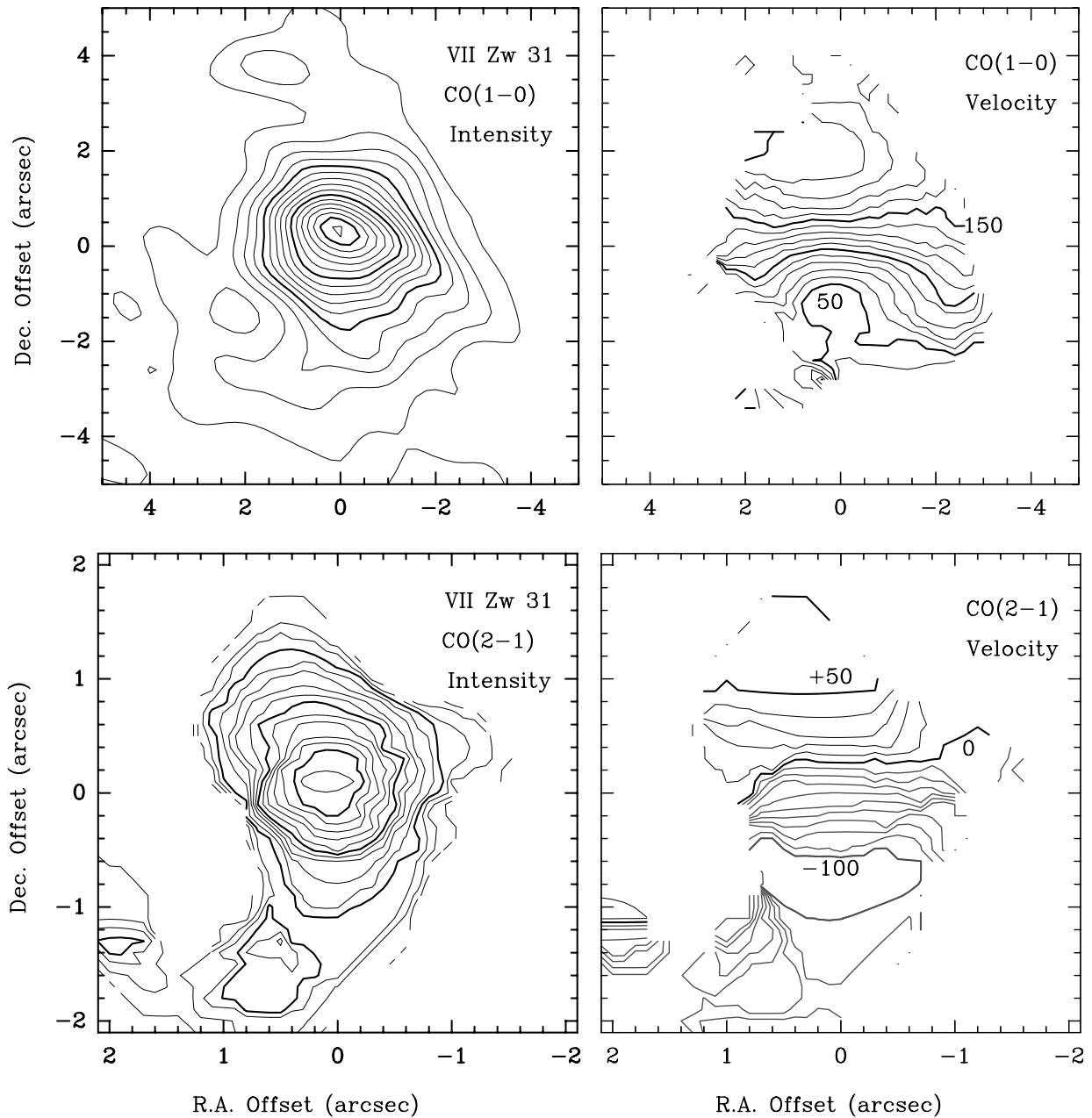


FIG. 2.—VII Zw 31. *Upper left panel:* CO (1–0) integrated over $(-40, +260)$ km s $^{-1}$. The beam is $1.^{\circ}4 \times 0.^{\circ}8$. Contour step is 1.2 Jy beam $^{-1}$ km s $^{-1}$, with $T_b/S = 88$ K Jy $^{-1}$. *Upper right panel:* Velocity contours in steps of 10 km s $^{-1}$ relative to 109.380 GHz ($cz_{\text{lsr}} = 16,147$ km s $^{-1}$). Labels are in km s $^{-1}$. *Lower left panel:* CO (2–1) integrated over $(-140, +80)$ km s $^{-1}$. Beam is $1.^{\circ}1 \times 0.^{\circ}8$. Contours are at 2 to 16 by 1 , in units of 1.6 Jy beam $^{-1}$ km s $^{-1}$, with $T_b/S = 30$ K Jy $^{-1}$. *Lower right panel:* Velocity contours in steps of 10 km s $^{-1}$ relative to 218.650 GHz ($cz_{\text{lsr}} = 16300$ km s $^{-1}$). Labels are in km s $^{-1}$. Center position in all maps is $05^{\text{h}}16^{\text{m}}46.51, 79^{\circ}40'12.5$ (J2000).

with this flux, corrected for a UV extinction of 5 mag (Smith et al. 1995) and a distance of 170 Mpc, has a UV luminosity of $4 \times 10^{11} L_{\odot}$. For an accretion disk temperature of 20,000 to 30,000 K, as in the models of Malkan & Sargent (1982) and Sanders et al. (1989), the blackbody peaks at 2000 to 1000 Å and has a radius of 1×10^{-3} pc. This result is consistent with the optical continuum, which has $A_V = 2$ mag and an intrinsic magnitude $M_V = -25.1$ (luminosity $5 \times 10^{11} L_{\odot}$; Boksenberg et al. 1977).

The dusty torus' luminosity can be derived from the near-infrared (NIR) continuum. As in other Seyfert 1 galaxies, the 2 μm bump is fitted well by a 1470 K blackbody, close to the dust sublimation point (Kobayashi et al. 1993). The flux at the 2 μm bump, 9.3×10^{-11} ergs s $^{-1}$ cm $^{-2}$ μm $^{-1}$, cor-

rected for an IR extinction of 0.2–0.6 mag (Krabbe et al. 1997), implies a blackbody luminosity of $3\text{--}4 \times 10^{11} L_{\odot}$ and a radius of 0.18 pc. The compact 10–25 μm source in Mrk 231 (Matthews et al. 1987; Keto et al. 1992; Miles et al. 1996) arises farther out in the dusty torus, where the dust temperature is ~ 200 K, at a radius of ~ 10 pc from the AGN. This dusty torus is heated by the AGN. If its thickness is equal to its radius, then the torus absorbs half the AGN's power, so the AGN's total luminosity is $6\text{--}9 \times 10^{11} L_{\odot}$, the same as estimated from the optical and UV flux.

The molecular disk's FIR luminosity can be derived from the *IRAS* fluxes, and is $2 \times 10^{12} L_{\odot}$ (e.g., Solomon et al. 1997). The molecular disk has a dust optical depth close to unity at 100 μm and causes the deep 10 μm silicate absorp-

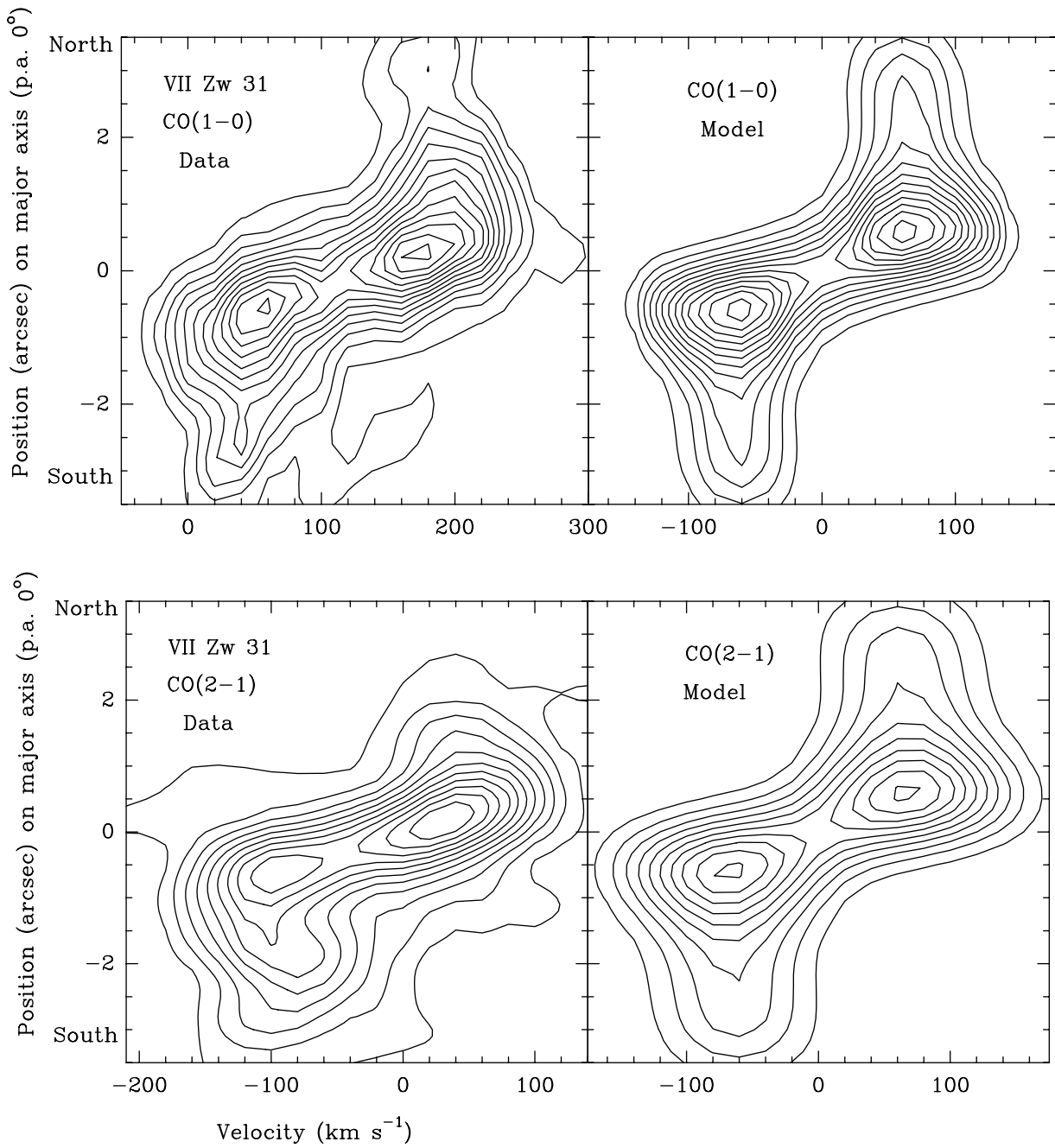


FIG. 3.—VII Zw 31. Shown are position-velocity cuts in declination, with zero position at $05^{\text{h}}16^{\text{m}}46\overset{\text{s}}{.}51, 79^{\circ}40'12\overset{\text{s}}{.}5$ (J2000). *Upper left panel:* CO (1–0) in a $1\overset{\prime}{.}4 \times 0\overset{\prime}{.}8$ beam. Contour step is 6 mJy beam $^{-1}$, with $T_b/S = 88$ K Jy $^{-1}$. Velocity is relative to 109.380 GHz ($cz_{\text{lsr}} = 16,147$ km s $^{-1}$). *Upper right panel:* Predicted CO (1–0) from the model, with same contours and resolution as for the data. *Lower left panel:* CO (2–1) in a $1\overset{\prime}{.}1 \times 0\overset{\prime}{.}8$ beam. Contours are 8 to 90, in steps of 4.9 mJy beam $^{-1}$, with $T_b/S = 30$ K Jy $^{-1}$. Velocity is relative to 218.650 GHz ($cz_{\text{lsr}} = 16,300$ km s $^{-1}$). *Lower right panel:* Predicted CO (2–1) from the model, with same contours and resolution as for the data.

tion (Allen 1976; Rieke 1976; Roche, Aitken, & Whitmore 1983). The blackbody radius calculated from the FIR luminosity is 200 pc, half the measured size of the molecular disk. The molecular disk receives some heat from the dusty torus. With the thickness-to-radius ratio in our CO model, it would intercept half of the power, or $2 \times 10^{11} L_\odot$ of reprocessed radiation from the AGN. Since this is only 10% of the FIR luminosity, most of the FIR luminosity of Mrk 231 must come from the starburst in the molecular ring or disk. A similar model was used by Rigopoulou, Lawrence, & Rowan-Robinson (1996) to fit the FIR continuum spectrum.

Our CO model fit gives a gas mass of $3.1 \times 10^9 M_\odot$ (equal to the mass of all the molecular gas in the Milky Way) in a high-density disk between $R = 76$ and 850 pc. There is another $0.9 \times 10^9 M_\odot$ of gas in a lower density outer disk extending to a radius of 1.7 kpc. The high-density molecular disk is the region observed in H₂ at 2 μm by Krabbe et al. (1997). The brightest H₂ line is 200 pc from the nucleus, in the molecular disk, so the low 2 μm extinction on the line of sight to the nucleus itself does not apply to the H₂ flux.

Our conclusion that most of Mrk 231's FIR luminosity comes from a starburst can be checked for consistency (see

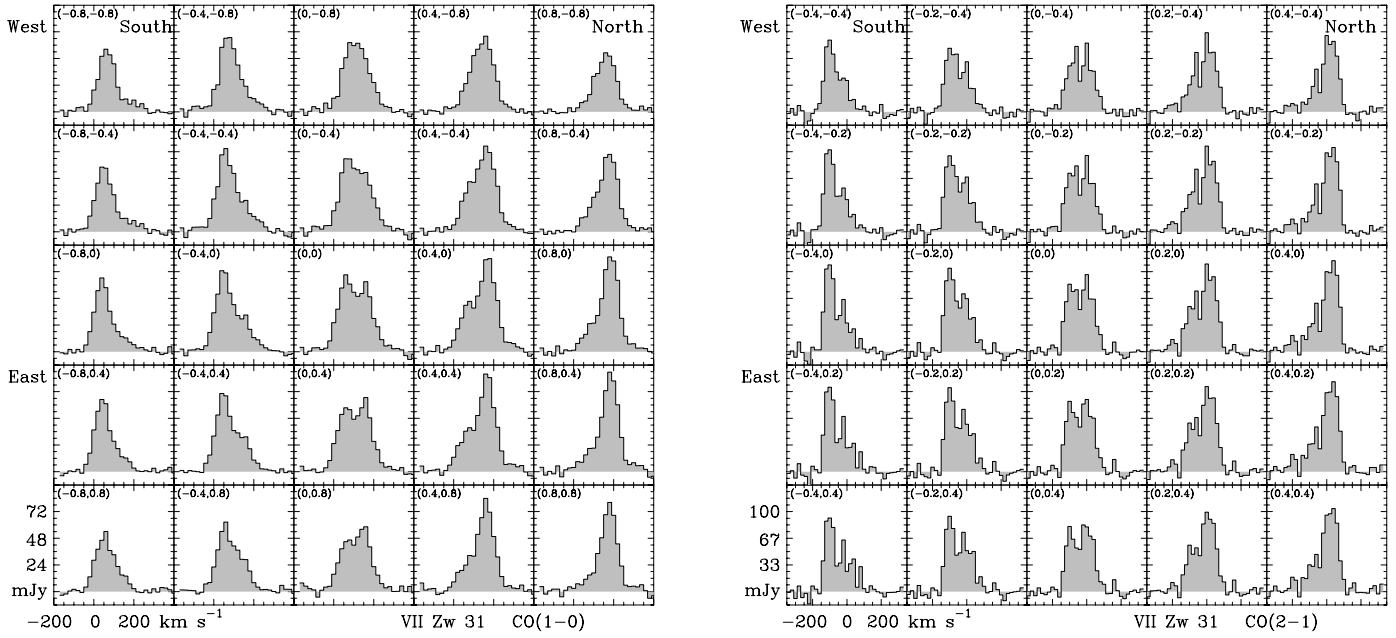


FIG. 4.—VII Zw 31. *Left panel:* CO (1–0) spectra vs. radial velocity relative to 109.380 GHz ($cz_{\text{lsr}} = 16,147 \text{ km s}^{-1}$). In the upper left of each box are offsets (in arcsec) on the kinematic major and minor axes. Beam is $1.4' \times 0.8'$, with $T_b/S = 88 \text{ K Jy}^{-1}$. *Right panel:* CO (2–1) spectra vs. radial velocity relative to 218.650 GHz ($cz_{\text{lsr}} = 16,300 \text{ km s}^{-1}$). In the upper left of each box are offsets (in arcsec) on the kinematic major and minor axes. Beam is $1.1' \times 0.8'$. The (0, 0) position in both diagrams is at $05^{\text{h}}16^{\text{m}}46.51^{\text{s}}$, $79^{\circ}40'12.5''$ (J2000).

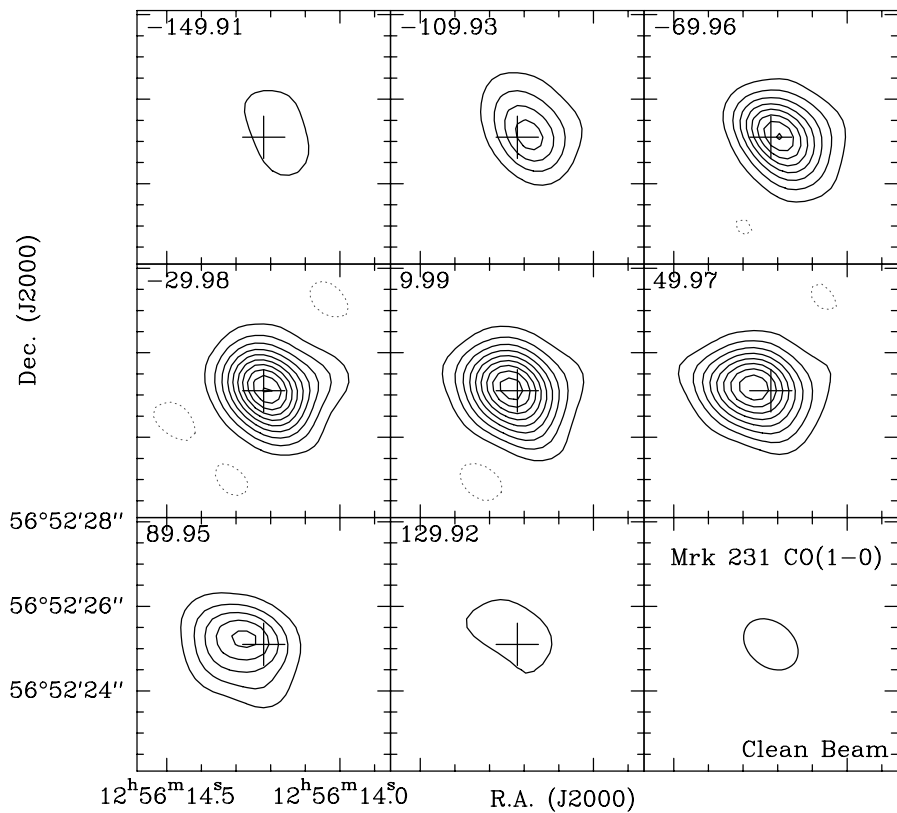


FIG. 5.—Mrk 231. *This page:* CO (1–0) in 40 km s $^{-1}$ channels. A 63 mJy continuum point source has been subtracted at the CO centroid (cross). Radial velocities (km s $^{-1}$, *upper left of each box*) are relative to 110.602 GHz ($cz_{\text{lsr}} = 12,656 \text{ km s}^{-1}$). Contour unit is 20 mJy beam $^{-1}$. Beam is $1.3' \times 1.1'$ (*lower right box*), with $T_b/S = 70 \text{ K Jy}^{-1}$. *Next page:* CO (2–1) in 40 km s $^{-1}$ channels. A 36 mJy continuum point source has been subtracted at the CO centroid (cross). Radial velocities (km s $^{-1}$, *upper left of each box*) are relative to 221.204 GHz ($cz_{\text{lsr}} = 12,650 \text{ km s}^{-1}$). Contour unit is 25 mJy beam $^{-1}$. Beam is $0.7' \times 0.5'$ (*lower right box*), with $T_b/S = 75 \text{ K Jy}^{-1}$.

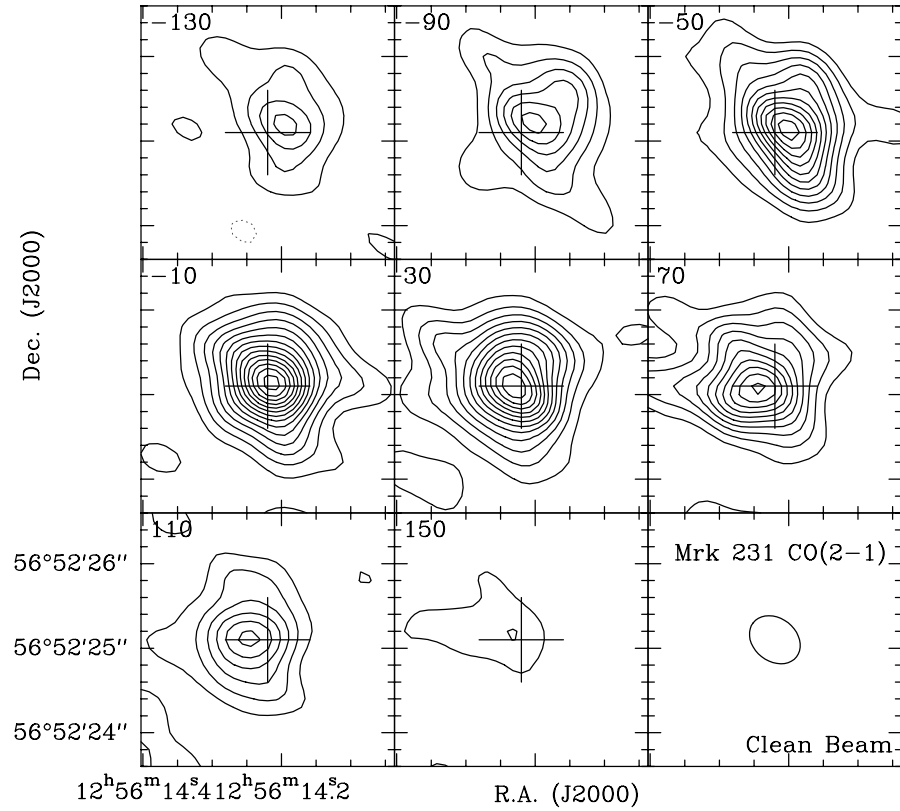


FIG. 5.—Continued

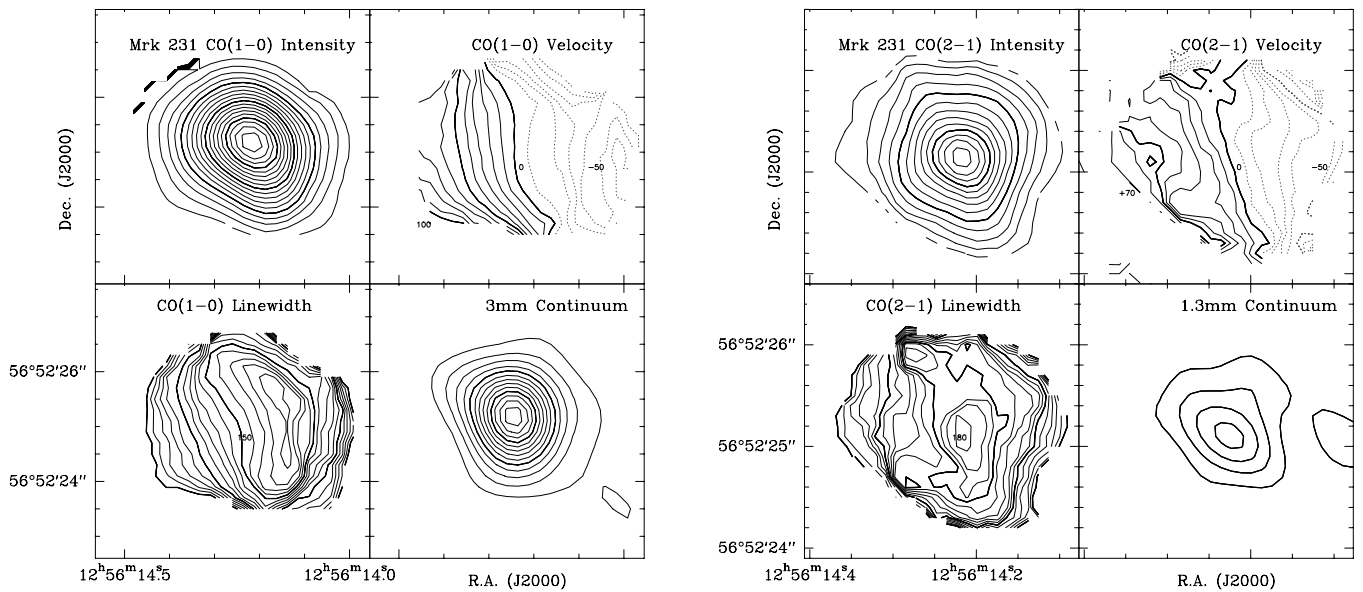


FIG. 6.—Mrk 231. *Left panel:* CO (1-0) integrated intensity, velocity, line width (FWHM), and the 3 mm continuum. The continuum source has been subtracted from the CO data. Integration limits are -180 , $+200$ km s $^{-1}$. Beam is 1.3×1.1 . Contours for the integrated CO are 1 to 18 by 1, in units of 2 Jy beam $^{-1}$ km s $^{-1}$, with $T_b/S = 70$ K Jy $^{-1}$; contours for the CO velocity are -60 to $+100$ km s $^{-1}$, in steps of 10 km s $^{-1}$, relative to 110.602 GHz ($cz_{lsr} = 12,656$ km s $^{-1}$); contours for the CO line width are 50 to 190 km s $^{-1}$, in steps of 10 km s $^{-1}$; contours for the 3 mm continuum are 1 to 13 by 1, in units of 4 mJy. Labels are in km s $^{-1}$. *Right panel:* CO (2-1) integrated intensity, velocity, line width (FWHM), and the 1.3 mm continuum. The continuum source has been subtracted from the CO data. Integration limits are ± 180 km s $^{-1}$. Beam is 0.7×0.5 . Contours for the integrated CO are 1 to 13 by 1, in units of 5 Jy beam $^{-1}$ km s $^{-1}$, with $T_b/S = 75$ K Jy $^{-1}$; contours for the CO velocity are -60 to $+70$ km s $^{-1}$, in steps of 10 km s $^{-1}$, relative to 221.204 GHz ($cz_{lsr} = 12,650$ km s $^{-1}$); contours for the CO line width are 50 to 180 km s $^{-1}$ in steps of 10 km s $^{-1}$; contours for the 1.3 mm continuum are 1 to 4 by 1, in units of 8 mJy. Labels are in km s $^{-1}$.

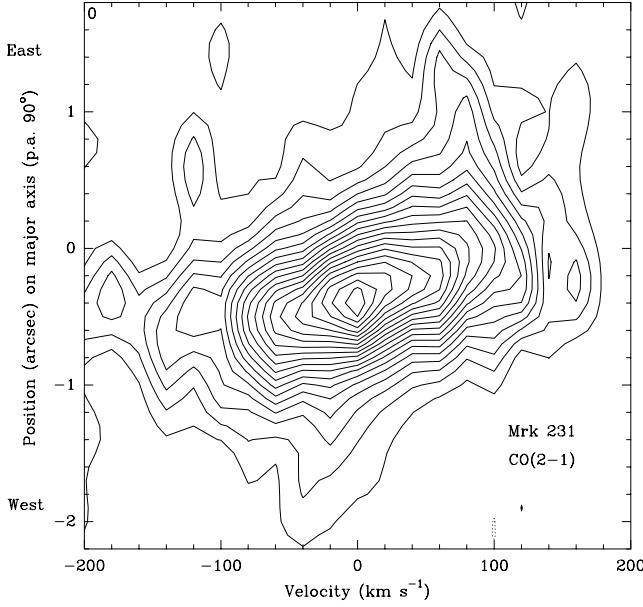


FIG. 7.—Mrk 231 CO (2-1) position-velocity diagram along the line of nodes (P.A. 90°). Contour levels are 1 to 19, in units of 20 mJy beam^{-1} , with $T_b/S = 75 \text{ K Jy}^{-1}$. Beam is $0\farcs7 \times 0\farcs5$. The $(0, 0)$ position is $12^{\text{h}}56^{\text{m}}14\rlap{.}^{\text{s}}260, 56^{\circ}52'25\rlap{.}^{\text{s}}13$ (J2000). Velocity is relative to 221.204 GHz ($cz_{\text{lsr}} = 12,650 \text{ km s}^{-1}$). The continuum source has been subtracted from the CO data.

Table 11). We assume that the new stars in the burst, $M_{\text{new}\star}$, yield $L_{\text{FIR}}/M_{\text{new}\star} \approx 500 L_\odot M^{-1}_\odot$, a luminosity ratio that can be attained in a fast starburst (Leitherer & Heckman 1995). Dividing this ratio into the FIR luminosity yields $M_{\text{new}\star}$, from which we then calculate $M_{\text{old}\star} = M_{\text{dyn}} - M_{\text{gas}} - M_{\text{new}\star}$, where $M_{\text{old}\star}$ is the mass of old stars in the nuclear bulge before the merger. For the region $R \leq 460 \text{ pc}$ in Mrk 231, the rotation velocity inferred from our CO data yields a dynamical mass $M_{\text{dyn}} (< 460 \text{ pc}) = 12.7 \times 10^9 M_\odot$, and our CO model yields $M_{\text{gas}} = 1.8 \times 10^9 M_\odot$. The consistency check then yields $M_{\text{old}\star} = 7.1 \times 10^9 M_\odot$, which is about the same as the mass of old stars in a similar radius in the Milky Way (e.g., Oort 1977). Because of our assumed L/M , the derived stellar masses in the starburst and the bulge are uncertain by at least a factor of 2. Our point is simply that with a starburst powering the FIR luminosity, all the gas and stellar masses are quite plausible. In summary, we think Mrk 231's black hole accretion disk emits $\sim 1 \times 10^{12} L_\odot$, or $\sim 30\%$ of the total bolometric luminosity. Most of the luminosity, $\sim 2 \times 10^{12} L_\odot$, comes from the starburst in the molecular ring or disk.

6. ARP 193

The ultraluminous merger Arp 193 shows two tidal tails in the visible and the NIR (Smith et al. 1995, 1996). The IR images show a single, elongated nucleus, but centimeter

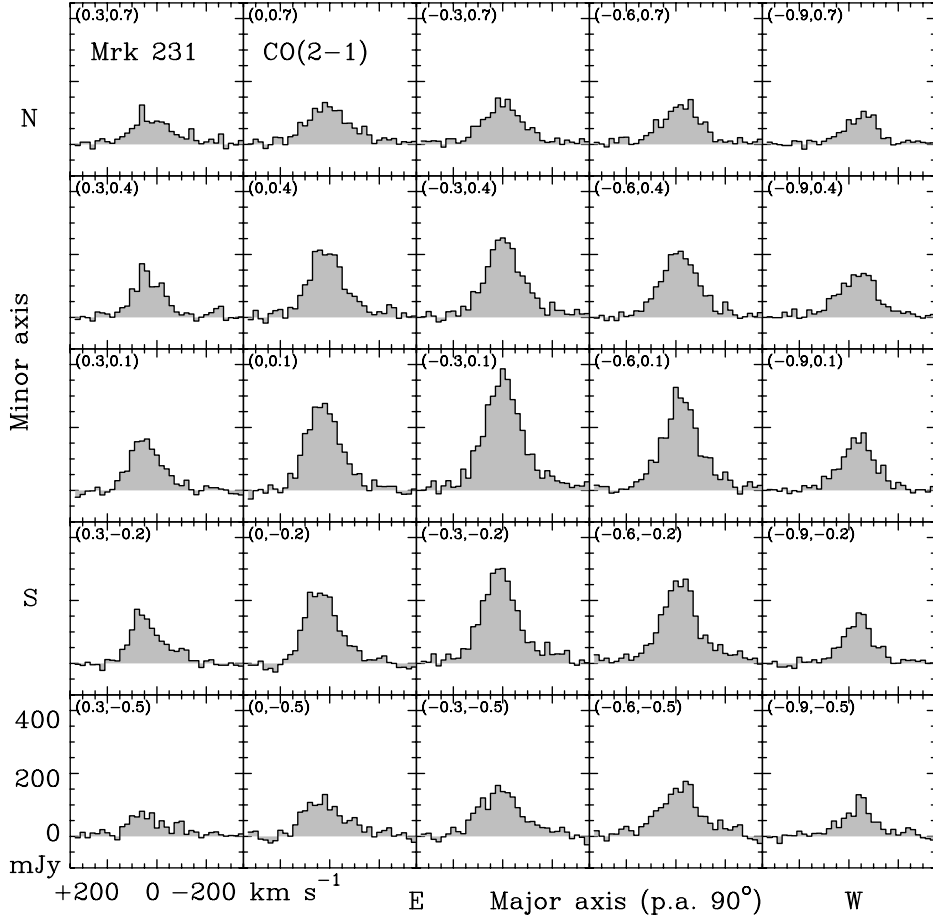


FIG. 8.—Mrk 231 CO (2-1) spectra vs. radial velocity relative to 221.204 GHz ($cz_{\text{lsr}} = 12,650 \text{ km s}^{-1}$; the velocity scale is reversed to emphasize the symmetry of the profiles). In the upper left of each box are offsets (in arcsec) on the kinematic major and minor axes. The $(0, 0)$ position is $12^{\text{h}}56^{\text{m}}14\rlap{.}^{\text{s}}260, 56^{\circ}52'25\rlap{.}^{\text{s}}13$ (J2000). Beam is $0\farcs7 \times 0\farcs5$, with $T_b/S = 75 \text{ K Jy}^{-1}$. The continuum source has been subtracted from the CO data.

TABLE 11
STARBURST CONSISTENCY CHECK: MASS IN GAS, NEW STARS, AND OLD BULGE STARS
IN THE CENTRAL MOLECULAR DISKS

| Parameter | Mrk 231 Disk | Mrk 273 Disk | Arp 220 Disk |
|--|--------------|--------------|--------------|
| Reference radius: | | | |
| R (pc)..... | 460 | 400 | 480 |
| Luminosity: | | | |
| $L_{\text{FIR}} (< R) (10^{12} L_{\odot})$ | 1.9 | 1.0 | 0.7 |
| $L_{\text{IR}}/M_{\text{new*}}^{\text{a}} (L_{\odot}/M_{\odot})$ | 500 | 500 | 300 |
| Deduced mass in new stars: | | | |
| $M_{\text{new*}}^{\text{b}} (< R) (10^9 M_{\odot})$ | 3.8 | 2.0 | 2.3 |
| Mass from CO model: | | | |
| $M_{\text{dyn}} (< R) (10^9 M_{\odot})$ | 12.7 | 8.7 | 12.1 |
| $M_{\text{gas}} (< R) (10^9 M_{\odot})$ | 1.8 | 2.1 | 1.9 |
| Deduced mass in old stars: | | | |
| $M_{\text{old*}}^{\text{c}} (< R) (10^9 M_{\odot})$ | 7.1 | 4.6 | 7.9 |

^a $L_{\text{IR}}/M_{\text{new*}}$ = assumed luminosity-to-mass ratio in a rapid starburst.

^b $M_{\text{new*}} = L_{\text{FIR}} (< R)/(L_{\text{IR}}/M_{\text{new*}})$ = mass of new stars formed in the current starburst.

^c $M_{\text{old*}} = M_{\text{dyn}} - M_{\text{gas}} - M_{\text{new*}}$ = mass of bulge stars within R (pc).

radio continuum maps show two sources separated by 1''. Strong lines of Br γ and H $_2$ are seen in the K band (Goldader et al. 1995). The NIR continuum is dominated by young supergiants formed in the merger-induced starburst. Previous CO line ratio studies indicated subthermal CO excitation and moderate densities (Radford et al. 1991b). Our detection of HCN in Arp 193 indicated, however, that large amounts of dense gas were also present (Solomon, Downes, & Radford 1992).

The CO (2–1) emission is nearly unresolved in individual 20 km s $^{-1}$ channels, with temperatures up to 8 K (Fig. 9). The CO intensity and isovelocity contour maps (Fig. 10) reveal a rotating disk with a line of nodes at the same orientation as the optical isophotes in the center of the merger. The position-velocity diagrams and CO spectra (Figs. 11 and 12) along the line of nodes have the characteristic signature of a rotating ring, with two peaks near the rotation curve turnover radius, as in VII Zw 31 and IRAS

10565+24. Models that best fit the data are those with a minimum ring radius R_{\min} in equation (1) equal to $R_0 = 220$ pc. As in VII Zw 31, filled-disk models with $R_{\min} = 0$ give poorer fits, with much less contrast. The centroid of the CO source coincides with the main radio continuum peak on the 8.4 GHz map of Condon et al. (1991). The strongest CO peak is 1'' to the southeast of the centroid, and peaks at –120 km s $^{-1}$ (relative to 225.282 GHz). It is nearly unresolved on our maps, coinciding with a secondary radio continuum peak. This hot, compact southeast CO core in Arp 193 is responsible for the large difference in the CO (2–1)/(1–0) ratio in the blue and redshifted sides of the line profiles we observed at the 30 m telescope (Radford et al. 1991a). This region is hotter and denser than the disk and has properties similar to a huge molecular cloud core.

This compact southeast core is one of several sources we identify in this study as *extreme starburst regions* (see § 8 on Arp 220 for a detailed discussion). Using the observed CO

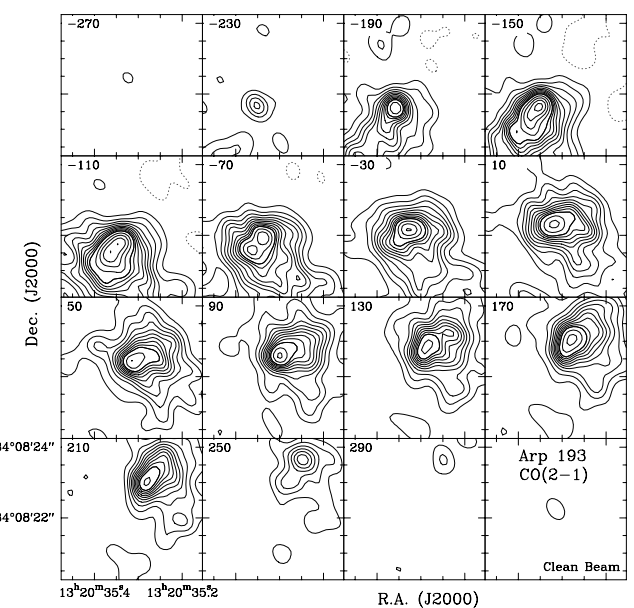
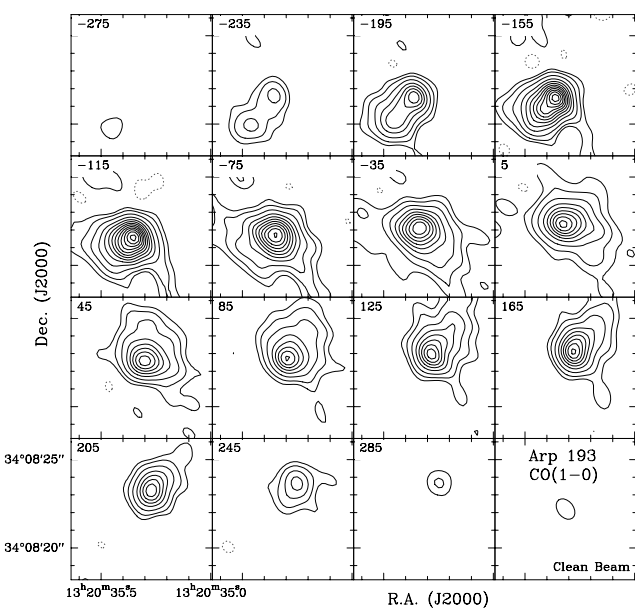


FIG. 9.—Arp 193. Left panel: CO (1–0) maps in 40 km s $^{-1}$ channels. Radial velocities (km s $^{-1}$, upper left of each box) are relative to 112.641 GHz ($cz_{\text{lsr}} = 7000$ km s $^{-1}$). Contour units are –5, 5, 10, then 20 to 170 by 15 mJy beam $^{-1}$. Beam is 1''.3 × 0''.9, with $T_b/S = 83$ K Jy $^{-1}$. Right panel: CO (2–1) maps in 40 km s $^{-1}$ channels. Radial velocities (km s $^{-1}$, upper left of each box) are relative to 225.282 GHz ($cz_{\text{lsr}} = 6994$ km s $^{-1}$). Contour intervals are –10, 10 to 100 in steps of 10, then 10 to 180 in steps of 20 mJy beam $^{-1}$. Beam is 0''.6 × 0''.4, with $T_b/S = 84$ K Jy $^{-1}$.

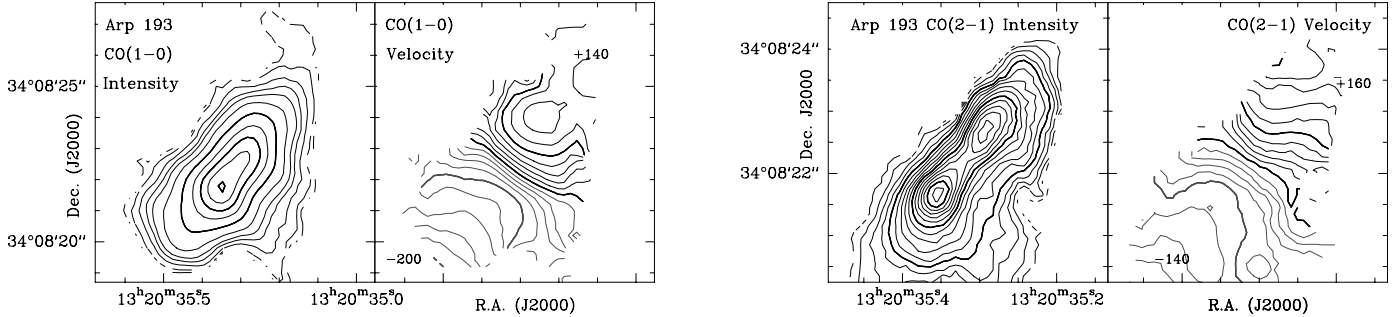


FIG. 10.—Arp 193. 1st left panel: CO (1–0) integrated from -245 to $+270 \text{ km s}^{-1}$. Beam is $1.^{\circ}3 \times 0.^{\circ}9$. Contours are $0.5, 1, 2, 3, 4, 6$, then 10 to 45 by $5 \text{ Jy beam}^{-1} \text{ km s}^{-1}$, with $T_b/S = 83 \text{ K Jy}^{-1}$. 2d left panel: Velocity contours in steps of 20 km s^{-1} relative to 112.641 GHz ($cz_{\text{lsr}} = 7000 \text{ km s}^{-1}$). Labels are in km s^{-1} . 1st right panel: CO (2–1) integrated from -210 to $+270 \text{ km s}^{-1}$. Beam is $0.^{\circ}6 \times 0.^{\circ}4$. Contour step is $2 \text{ Jy beam}^{-1} \text{ km s}^{-1}$, with $T_b/S = 84 \text{ K Jy}^{-1}$. 2d right panel: Velocity contours in steps of 20 km s^{-1} relative to 225.282 GHz ($cz_{\text{lsr}} = 6994 \text{ km s}^{-1}$). Labels are in km s^{-1}

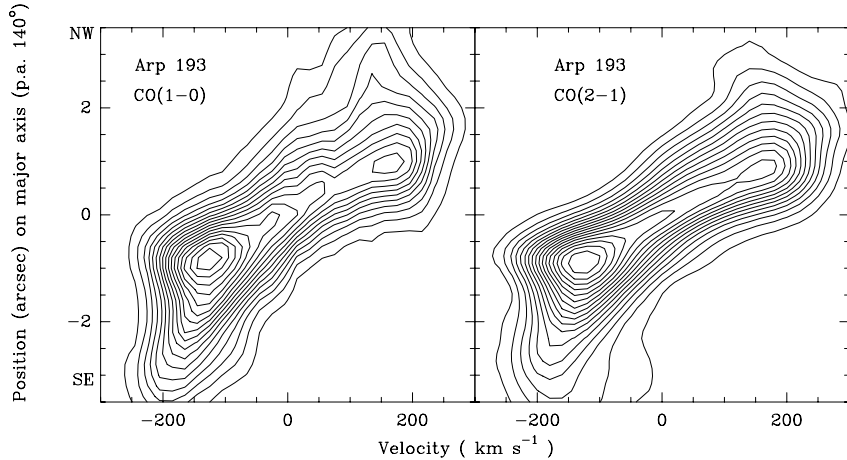


FIG. 11.—Arp 193 CO position-velocity diagrams along the line of nodes (P.A. 140°). Left panel: CO (1–0), contour units 10 mJy beam^{-1} , with $T_b/S = 83 \text{ K Jy}^{-1}$. Beam is $1.^{\circ}3 \times 0.^{\circ}9$. Velocity is relative to 112.641 GHz ($cz_{\text{lsr}} = 7000 \text{ km s}^{-1}$). Right panel: CO (2–1), contour unit 10 mJy beam^{-1} , with $T_b/S = 84 \text{ K Jy}^{-1}$. Beam is $0.^{\circ}6 \times 0.^{\circ}4$. Velocity is relative to 225.282 GHz ($cz_{\text{lsr}} = 6994 \text{ km s}^{-1}$). The $(0, 0)$ position in both diagrams is $13^{\text{h}}20^{\text{m}}35^{\text{s}}315, 34^{\circ}08'22''.20$ (J2000).

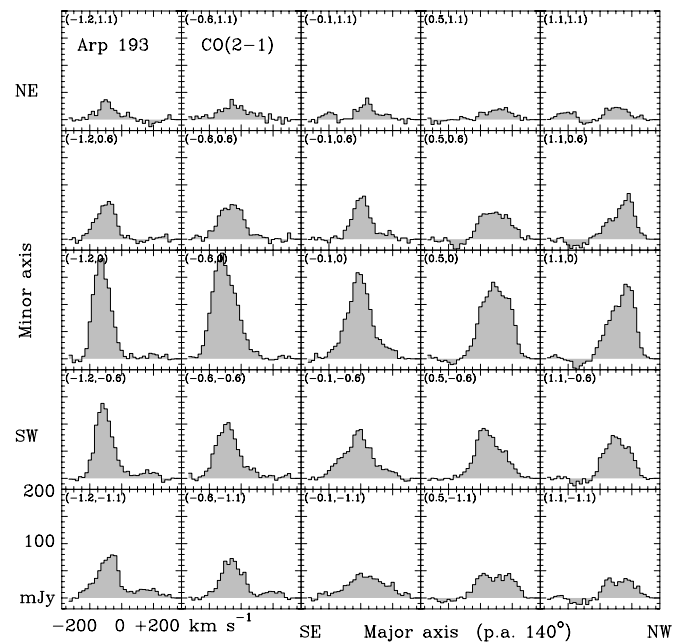
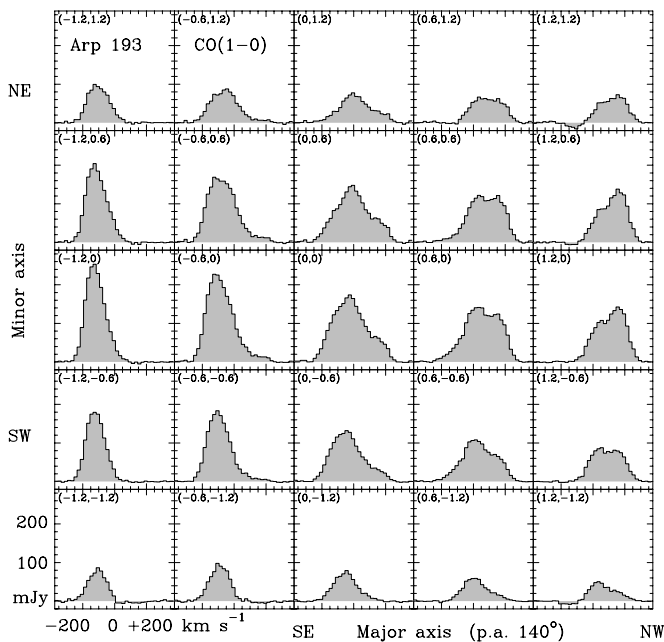


FIG. 12.—Arp 193. Left panel: CO (1–0) spectra. In each box, the vertical axis is CO intensity and the horizontal axis is radial velocity relative to 112.641 GHz ($cz_{\text{lsr}} = 7000 \text{ km s}^{-1}$). In the upper left of each box are offsets (in arcsec) on the kinematic major and minor axes. Beam is smoothed to $1.^{\circ}7 \times 1.^{\circ}6$. Right panel: CO (2–1) spectra. Beam is $0.^{\circ}6 \times 0.^{\circ}4$. Velocity is relative to 225.282 GHz ($cz_{\text{lsr}} = 6994 \text{ km s}^{-1}$). The $(0, 0)$ position in both diagrams is $13^{\text{h}}20^{\text{m}}35^{\text{s}}315, 34^{\circ}08'22''.20$ (J2000).

luminosity, line width, radius, and temperature, we can estimate the gas mass, dynamical mass, and FIR luminosity of the core. The results, summarized in Table 12, indicate an object with a gas mass $\sim 6 \times 10^8 M_\odot$, a luminosity of $\sim 2 \times 10^{11} L_\odot$, and about $\sim 1 \times 10^9 M_\odot$ of newly formed stars.

7. MARKARIAN 273

The galaxy Mrk 273 has at least one Seyfert 2 nucleus with optical line widths of 700 km s^{-1} (e.g., Sargent 1972; Koski 1978). There is evidence for two Seyfert 2 nuclei (Asatrian, Petrosian, & Börnigen 1990), and two nuclei are seen on IR images (Armus et al. 1992; Majewski et al. 1993; Knapen et al. 1997). Centimeter radio maps show a $0''.3$ northwest peak coinciding with the CO, and a weaker $0''.2$ southeast peak with no CO or IR counterpart (Ulvestad & Wilson 1984; Schmelz, Baan, & Haschick 1988; Sopp & Alexander 1991; Condon et al. 1991). There is also an 18 cm VLBI source of 16 mJy (Lonsdale et al. 1993; Smith, Lonsdale, & Lonsdale 1998a). The best previous CO study is by Yun & Scoville (1995), who observed the source with a $2''$ beam and found a component extended north-south as well as an unresolved nuclear component. Our higher resolution CO maps also show the extended structure, but now resolve the nuclear source into a nuclear disk oriented east-west and a very compact core embedded in the nuclear disk.

7.1. Extended Molecular Gas and Nuclear Disk in Mrk 273

The extended gas is best traced in the CO (1–0) channel maps, blueshifted to the south and redshifted to the north (Fig. 13a). The CO at $+250$ to $+350 \text{ km s}^{-1}$ runs in an arc from $3''$ to $7''$ (2 to 5 kpc) north of the nucleus (Fig. 14). This extended gas also appears in the maps of CO (1–0) integrated intensity and isovelocity contours (Fig. 15a). The CO (1–0) lines are weaker and narrower in the northern arc than in the nuclear disk (Fig. 16). The arc has 4% of the CO (1–0) flux of Mrk 273, so if gas mass is proportional to CO flux, then the northern arc has a gas mass of $1 \times 10^8 M_\odot$. Figure 17a is the CO position-velocity cut in declination, through the nucleus. The narrow-line emission extends $7''$ (5

kpc) south at 0 km s^{-1} and $7''$ north at $+300 \text{ km s}^{-1}$. It is tempting to speculate that the streamers are bringing molecular gas into the center. The north-south extent of the streamers on our CO map agrees with that on the map of Yun & Scoville (1995). While those authors deduced a line of nodes at P.A. 30° , our isovelocity contour maps show that there are two perpendicular kinematic systems. In the extended gas the velocity gradient is north-south, and in the nuclear disk it is east-west.

The $2''$ nuclear disk and its compact core are best seen in the CO (2–1) channel maps, made with a $0''.6$ beam (Fig. 13b). The nuclear disk kinematics are shown in the CO (2–1) map (Fig. 15b), where the isovelocity contours trace the east-west velocity gradient of the nuclear disk over a 1 kpc diameter. Figure 17b shows the CO position-velocity diagram of the nuclear disk in right ascension. The broad nuclear disk line has a FWHM of 380 km s^{-1} , and its velocity centroid changes from -300 to $+200 \text{ km s}^{-1}$ over $0''.5$ from west to east. This is a projected velocity gradient of $1.5 \text{ km s}^{-1} \text{ pc}^{-1}$, the same as deduced by Schmelz et al. (1988) from H I absorption. Table 11 lists the stellar and gas masses that would be needed in a starburst in the Mrk 273 molecular disk if the $L_{\text{FIR}}/M_{\text{new}*}$ ratio is the same as adopted in our starburst model of Mrk 231.

7.2. An Extreme Starburst Region in Mrk 273

The high-resolution CO (2–1) maps show a remarkable molecular-line source in the Mrk 273 nuclear disk: a bright, $0''.35 \times <0''.2$ CO core (Fig. 15b) that resembles the west nucleus of Arp 220. This is the most luminous extreme starburst region in our sample of 10 galaxies. It has an IR luminosity of about $6 \times 10^{11} L_\odot$, generated in a region with a radius of only 120 pc and a current molecular mass of $1 \times 10^9 M_\odot$ (Table 12). To put this in perspective, the entire molecular core has a radius about 5 times that of an IR-luminous Milky Way GMC (for example, W51), but with about 3000 times the molecular mass and $\approx 10^5$ times the IR luminosity from OB stars.

This core has a broad CO line with a zero-intensity width of 1060 km s^{-1} , the same as the OH megamaser (Staveley-Smith et al. 1987). It coincides with the northwest extended

TABLE 12
PROPERTIES OF EXTREME STARBURST REGIONS

| Parameter | Arp 193 SE Core | Mrk 273 Core | Arp 220 West | Arp 220 East |
|--|-----------------|-----------------|-----------------|-----------------|
| Reference radius: ^a | | | | |
| R (pc)..... | 150 | 120 | 68 | 110 |
| Gas mass: ^b | | | | |
| $M_{\text{gas}} (< R) (10^9 M_\odot)$ | 0.6 | 1.0 | 0.6 | 1.1 |
| Mean gas density: ^c | | | | |
| $\langle N(\text{H}_2) \rangle (\text{cm}^{-3})$ | 2×10^3 | 5×10^3 | 2×10^4 | 8×10^3 |
| Total mass (gas plus stars): ^d | | | | |
| $M_{\text{tot}} (< R) (10^9 M_\odot)$ | 1.4 | 2.6 | 1.4 | 3.2 |
| Estimated mass in new stars: ^e | | | | |
| $M_{\text{new}*} (< R) (10^9 M_\odot)$ | 0.8 | 1.6 | 0.8 | 2.1 |
| Luminosity: ^f | | | | |
| $L_{\text{FIR}} (< R) (10^{12} L_\odot)$ | 0.2 | 0.6 | 0.3 | 0.2 |
| Luminosity to mass ratio: ^g | | | | |
| $L_{\text{FIR}}/M_{\text{new}*} (L_\odot/M_\odot)$ | 300 | 360 | 380 | 100 |

^a Radius from measurements (see Table 3 or 4).

^b $M_{\text{gas}} \approx 1.0 L'_{\text{CO}}$ (see Table 9).

^c $\langle N(\text{H}_2) \rangle \text{ cm}^{-3} = 0.1 (M_{\text{gas}}/M_\odot) r_{\text{pc}}^3$ (cylinder).

^d $M_{\text{tot}} = R \Delta V^2/G$.

^e $M_{\text{new}*} = M_{\text{tot}} - M_{\text{gas}}$.

^f $L_{\text{IR}}/L_\odot = 0.13 r_{\text{pc}}^2 T^4$, with T from Table 6.

^g $L_{\text{FIR}}/M_{\text{new}*}$ = luminosity-to-mass ratio of new stars formed in the current starburst.

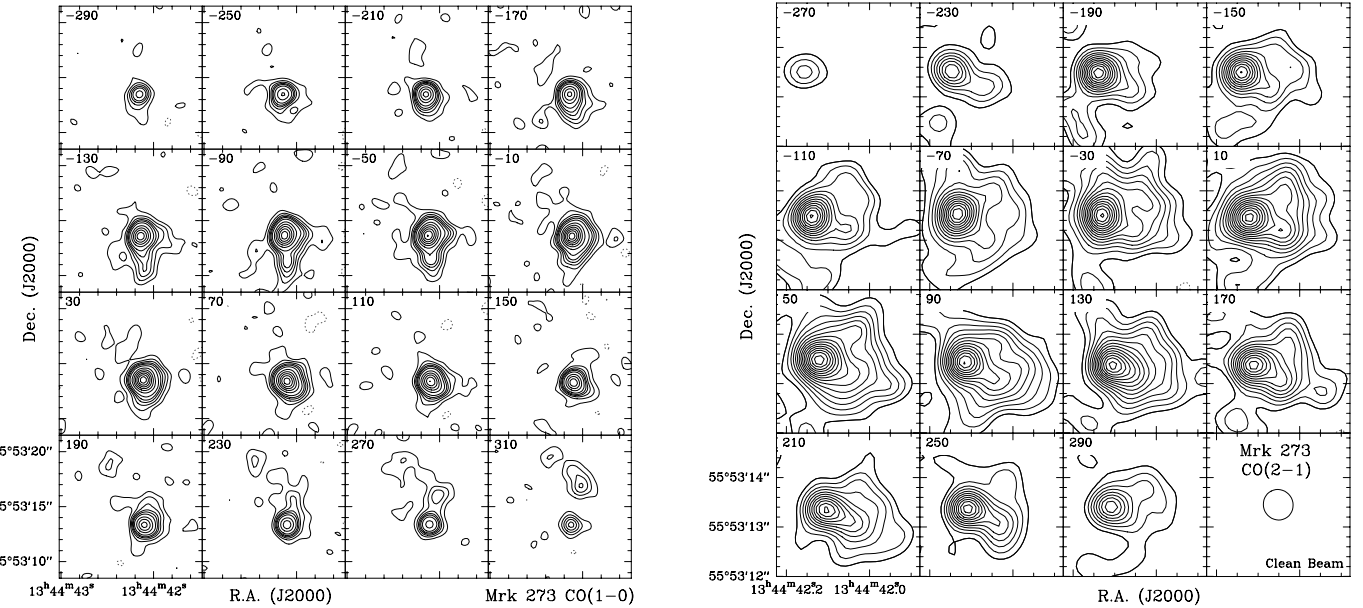


FIG. 13.—Mrk 273. Left panel: CO (1–0) maps in 40 km s^{-1} channels. Radial velocities (km s^{-1} , upper left of each box) are relative to 111.076 GHz ($cz_{\text{lsr}} = 11323 \text{ km s}^{-1}$). Contour units are $-3, +3$ to 15 by 5, then 20 to 80 by 10 mJy beam^{-1} ; negative contours are dashed, and the zero contour is omitted. Beam = $1.^{\circ}4 \times 1.^{\circ}3$ with $T_b/S = 56 \text{ K Jy}^{-1}$. Right panel: CO (2–1) maps in 40 km s^{-1} channels. Radial velocities (km s^{-1} , upper left of each box) are relative to 222.176 GHz ($cz_{\text{lsr}} = 11,283 \text{ km s}^{-1}$). Contour interval is 10 to 85, in steps of 5 mJy beam^{-1} . Beam is $0.^{\circ}6$, with $T_b/S = 66 \text{ K Jy}^{-1}$.

continuum peak at 8.44 GHz, which has a size of $0.^{\circ}32 \times 0.^{\circ}18$ (Condon et al. 1991), the same as the compact CO. The radio spectrum is nonthermal, with a spectral index of -0.6 . The thermal dust emission dominates the spectrum above 350 GHz (Chini et al. 1989; Rigopoulou et al. 1996). At the CO core, we detect continuum fluxes of $11 \pm 2 \text{ mJy}$ at 111 GHz and $8 \pm 2 \text{ mJy}$ at 225 GHz. Extrapolation of the synchrotron and thermal dust spectra indicates that the dust contributes 50% of the flux at 1.3 mm and $<10\%$ at 3 mm. The extended nonthermal continuum emission coin-

cident with a high mass of dust and gas leaves little doubt that this region is powered by star formation.

8. ARP 220

The center of the ultraluminous galaxy Arp 220 has two radio-continuum and two IR sources $1.^{\circ}0$ apart that are interpreted as merger nuclei. These are not exactly the same objects in the radio and the IR, because both the east and west IR nuclei are 4 times larger ($0.^{\circ}8$) than the radio sources ($0.^{\circ}2$) (Condon et al. 1991; Graham et al. 1990; Majewski et al. 1993; Miles et al. 1996; Scoville et al. 1998). The K-band continuum is starlight associated with the nuclei, and is best seen on the *HST* NICMOS images (Scoville et al. 1998). These images resolve the eastern IR nucleus into a strong northeastern and weaker southeastern component, the latter of which coincides with the eastern radio-continuum component and the eastern OH masers (Diamond et al. 1989). The two radio sources are extended and nonthermal, and are produced by supernovae in the most active star-forming regions. The 1.3 and $1.6 \mu\text{m}$ [Fe II] lines in the west source indicate iron evaporated from dust in shocks (Armus et al. 1995b; van der Werf & Israel 1998). The best previous CO study is that by Scoville, Yun, & Bryant (1997), who derived the kinematics of the nuclear disk with a resolution of $1''$.

8.1. CO and Dust Emission from the Two Nuclei of Arp 220

Our CO (2–1) and 1.3 mm continuum maps (Fig. 18a) show two compact sources embedded in more extended emission. The continuum fluxes at 1.3 mm are due to dust, because they are well above the extrapolated radio synchrotron spectra (Fig. 19). The different appearance of the dust continuum and the CO maps is a temperature effect. At 1.3 mm, the dust is optically thin and its flux varies as the column density and the dust temperature, while the CO flux is partly opaque, with flux varying with temperature at the surface, and partly optically thin, with flux varying inversely

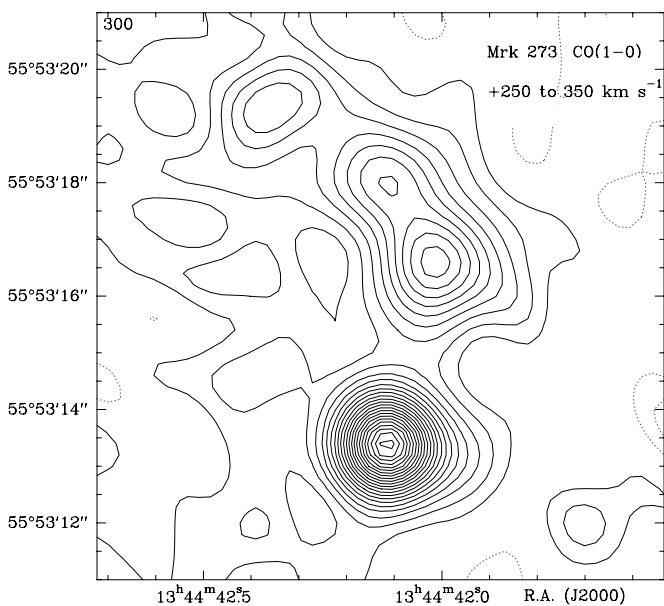


FIG. 14.—Mrk 273 CO (1–0), integrated over 250 to 350 km s^{-1} , relative to 111.076 GHz ($cz_{\text{lsr}} = 11323 \text{ km s}^{-1}$). Beam is $1.^{\circ}4 \times 1.^{\circ}3$, with $T_b/S = 56 \text{ K Jy}^{-1}$. Contour step is 1 mJy beam^{-1} ; negative contours are dashed, and the zero contour is omitted.

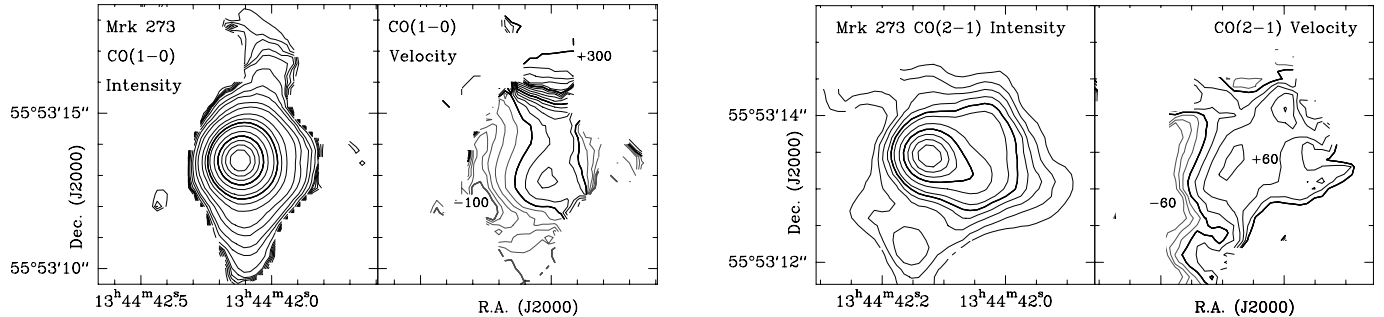


FIG. 15.—Mrk 273. 1st left panel: CO (1–0) integrated over $\pm 340 \text{ km s}^{-1}$. Beam is $1.^{\circ}4 \times 1.^{\circ}3$. Contours are 0.3 to 0.7 by 0.1; then 1, 1.5, 2, 3, 4, 6; then 8 to 36 by $4 \text{ Jy beam}^{-1} \text{ km s}^{-1}$, with $T_b/S = 56 \text{ K Jy}^{-1}$. 2d left panel: Velocity contours are in steps of 20 km s^{-1} relative to 111.076 GHz ($cz_{\text{lsr}} = 11,323 \text{ km s}^{-1}$). Labels are in km s^{-1} . 1st right panel: CO (2–1) integrated over $\pm 300 \text{ km s}^{-1}$. Beam is $0.^{\circ}6 \times 0.^{\circ}6$. Contours are 2, 4, 6, then 8 to 32 in steps of $4 \text{ Jy beam}^{-1} \text{ km s}^{-1}$, with $T_b/S = 66 \text{ K Jy}^{-1}$. 2d right panel: Velocity contours are in steps of 20 km s^{-1} relative to 222.176 GHz ($cz_{\text{lsr}} = 11,283 \text{ km s}^{-1}$). Labels are in km s^{-1} .

with CO excitation temperature. The Arp 220 molecular disk contributes strongly to the CO maps, while the warmer compact peaks dominate the dust-continuum maps. From the 1.3 mm dust flux alone, and for dust at 100 K and solar metallicity, we derive gas masses for Arp 220 west and east of 0.6 and $1.1 \times 10^9 M_\odot$.

In Arp 220 west, the $0.^{\circ}3$ (100 pc) mm continuum dust source coincides within $0.^{\circ}1$ of the centimeter-continuum west peak and the K-band west peak (Scoville et al. 1998). In the CO (2–1) channel maps (Fig. 20b), Arp 220 west appears as a strong source in the range -310 to $+210 \text{ km}$

s^{-1} , peaking at -110 km s^{-1} ($cz_{\text{lsr}} = 5340 \text{ km s}^{-1}$), with an observed CO (2–1) brightness temperature of 27 K, of which 10 K is from the more extended Arp 220 disk. The positive-velocity emission near Arp 220 west is centered at $+80 \text{ km s}^{-1}$, and appears in both the CO (2–1) channel maps and in a position-velocity cut at P.A. 300° (Fig. 21b). This positive-velocity emission has about 25% of the CO integrated intensity of the negative-velocity emission of Arp 220 west.

The dust continuum is centered between the negative- and positive-velocity emission, suggesting that Arp 220 west is a composite structure, with a kinematic axis nearly per-

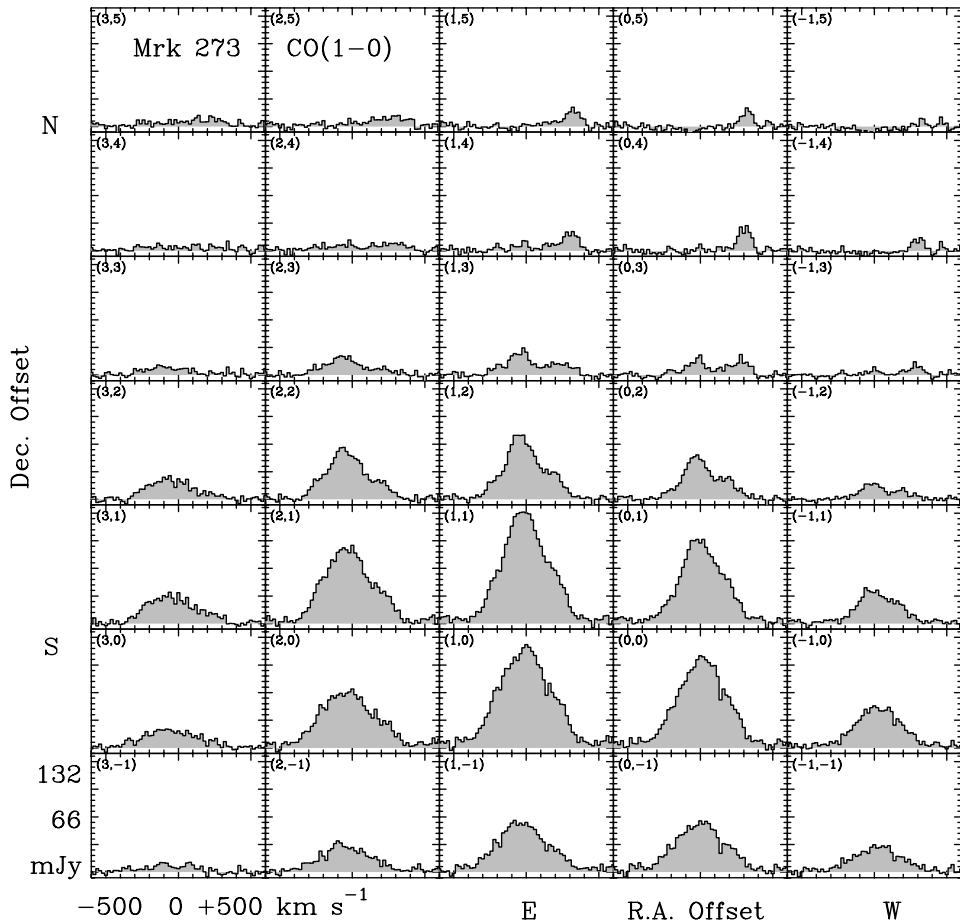


FIG. 16.—Mrk 273 CO (1–0) spectra. In each box, vertical axis is the CO intensity, horizontal axis is the radial velocity relative to 111.076 GHz ($cz_{\text{lsr}} = 11,323 \text{ km s}^{-1}$). In the upper left of each box are R.A. and decl. offsets (in arcsec); the $(0, 0)$ position is $13^{\text{h}}44^{\text{m}}42\rlap{.}^{\text{s}}01, 55^{\circ}53'13\rlap{.}^{\text{s}}0$ (J2000). Beam is $2.^{\circ}9 \times 2.^{\circ}1$, with $T_b/S = 16 \text{ K Jy}^{-1}$.

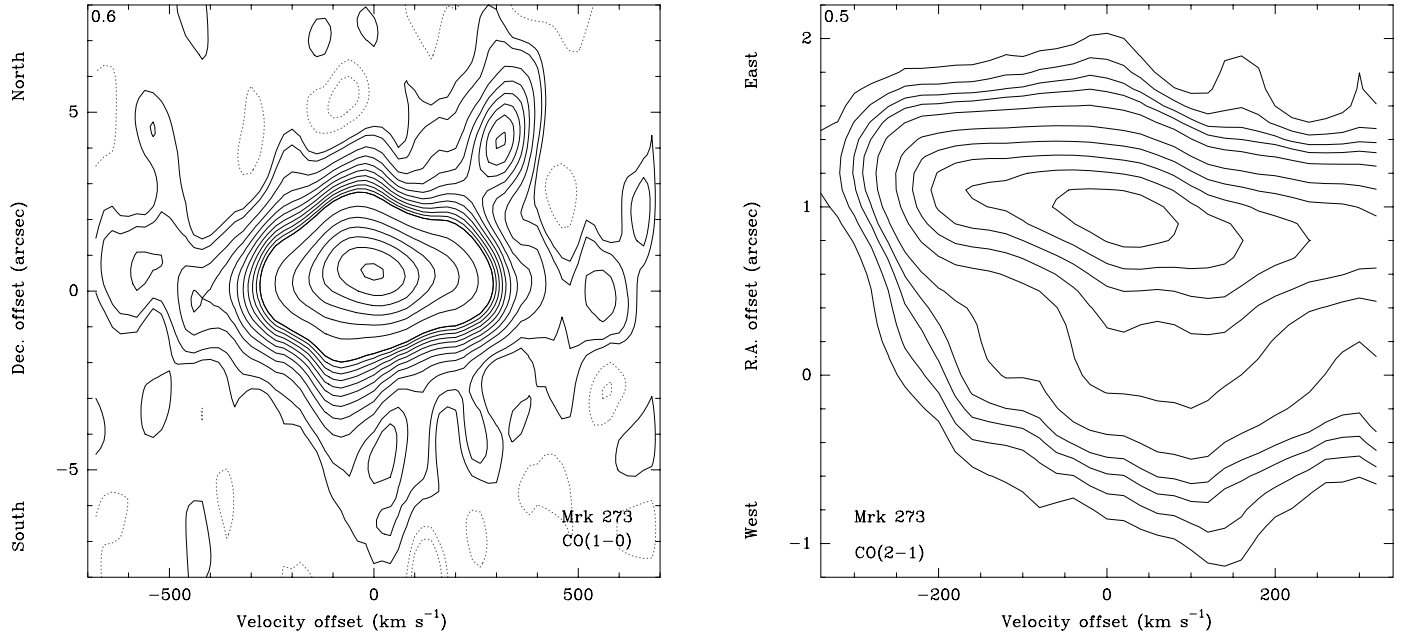


FIG. 17.—Mrk 273. *Left panel:* CO (1–0) position-velocity diagram in declination, through the center of Mrk 273. Note at +300 km s^{−1} the second CO complex 4'' north of the main CO peak. Contour levels are −2, −1, +1, then 2 to 20 by 2, and 20 to 160 by 10, in units of 1.7 mJy beam^{−1}, with $T_b/S = 16$ K Jy^{−1}. Beam is 2''.9 × 2''.1. Velocity is relative to 111.076 GHz ($cz_{lsr} = 11,323$ km s^{−1}). The (0, 0) position is 13^h44^m42^s01, 55°53'13".0 (J2000). *Right panel:* CO (2–1) position-velocity diagram along the line of nodes of the nuclear disk (P.A. 90°, i.e., the R.A. axis). Contour levels are 3 to 15 by 3, then 20 to 70 by 10 mJy beam^{−1}, with $T_b/S = 66$ K Jy^{−1}. Beam is 0''.6 × 0''.6. Velocity is relative to 222.176 GHz ($cz_{lsr} = 11,283$ km s^{−1}). The (0, 0) position is 13^h44^m42^s01, 55°53'13".5 (J2000).

pendicular to that of Arp 220's main disk. At the negative-velocity west core, the emission extends asymmetrically from −50 to −400 km s^{−1} (Fig. 21b). At the positive velocity core, it runs from +50 to +350 km s^{−1}. These extreme asymmetric line profiles, confined to a small region, suggest either possible radial flows along a bar-like structure, or immense high-velocity molecular outflows similar to those observed in high-mass star formation regions. Molecular outflows are also the likely sites of the strong H₂ lines (Sturm et al. 1996).

In Arp 220 east, the CO covers a wide velocity range. The negative-velocity gas at −230 to −30 km s^{−1} is separated from Arp 220 west by 0''.85 at P.A. 110°, the same angle as the centimeter radio continuum sources, the 18 cm OH masers, and the K-band southeast peak (Scoville et al. 1998). The center velocity of this gas is $cz_{lsr} = 5330$ km s^{−1}, close to that of the OH megamasers and H₂CO emission at the centimeter radio east source (Baan & Haschick 1995; Lonsdale et al. 1998). There is also more extended, positive-velocity gas (0''.9 FWHM) at 130 to 290 km s^{−1}. It is 1''.3 from Arp 220 west, at P.A. 85°, the same orientation as the K-band northeast source (Scoville et al. 1998). This positive-velocity gas in Arp 220 east, at ∼+200 km s^{−1} ($cz_{lsr} = 5650$ km s^{−1}), has the same velocity offset from Arp 220 west as the ionized gas seen in Bry and Paβ (Larkin et al. 1995) and in the weak OH masers at 1612 MHz (Baan & Haschick 1987). Its observed maximum CO (2–1) brightness temperature is 19 K, of which 4 K is from the extended Arp 220 disk. The 1.3 mm continuum from dust in Arp 220 east has a diameter of 0''.6 (205 pc) and is displaced by 0''.3 from the centimeter radio east source. It falls in between the K-band northeastern and southeastern peaks on the images by Scoville et al. (1998), and in between the positive- and negative-velocity CO. The kinematic data suggest that Arp

220 east has a steady progression of velocity between the CO peaks at 5330 km s^{−1} and 5650 km s^{−1}, along the same position angle (P.A. 50°), and in the same sense of rotation as the main, larger scale molecular disk of Arp 220 (Fig. 21c).

8.2. CO in the Arp 220 Molecular Disk

The molecular disk is best seen as an extended source in the CO (1–0) maps (Fig. 18b). The CO (2–1) maps show this same extended source when the compact peaks are subtracted. The disk has CO half-widths of 2''.0 × 1''.6 at P.A. 50°, with a line of nodes at this same position angle, blue-shifted in the southwest and redshifted in the northeast, as seen in the CO spectra along the major axis (Fig. 22). Our model fits yield a rotation curve turnover radius of 200 pc, a disk outer radius of 480 pc, and a disk rotation velocity of 330 km s^{−1} on the flat part of the rotation curve. The CO emission centroid of the molecular disk is ∼0''.3 east of the western nucleus. These parameters reproduce the position-velocity diagrams along the kinematic major axis (Fig. 21), and are similar to the values derived by Scoville et al. (1997) using a different algorithm. On a larger scale, CO can be traced in the 8'' diameter outer disk at the same position angle. The inner and outer disks both contain shocked gas, detected in the NIR vibrational lines of H₂ (van der Werf 1996).

The CO (1–0) maps also show an eastern streamer extending 7'' (3 kpc) perpendicular to the disk, in the range +45 to +245 km s^{−1}, curving in to the east nucleus with increasing velocity offset (Fig. 20a). This east streamer is most intense at 85 to 165 km s^{−1} (Fig. 18b). It may be material that is still falling in to the center. Surprisingly, this CO streamer appears on the *HST V*-band image of Shaya et al. (1994). The CO inner and outer disks coincide with the

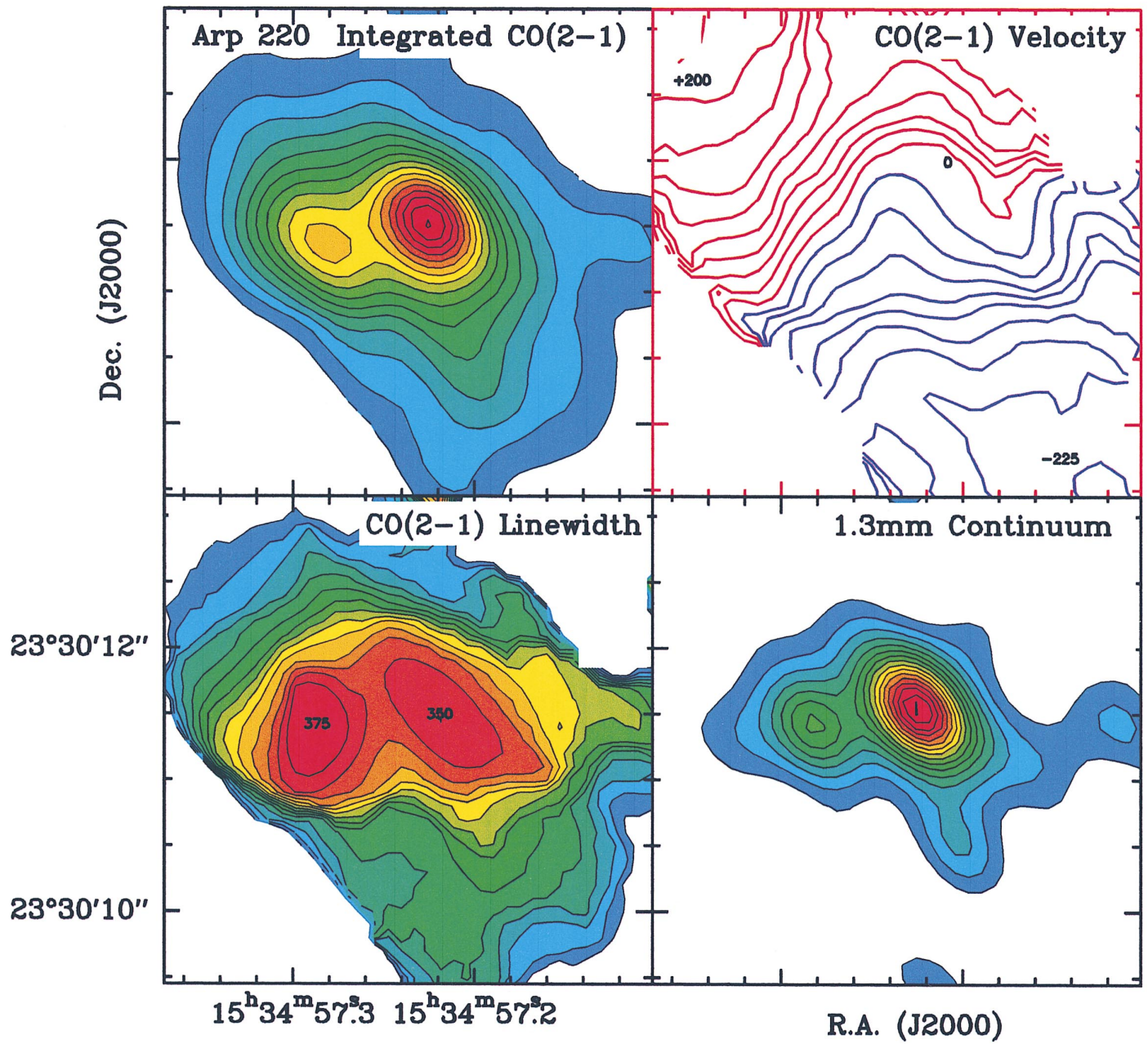


FIG. 18.—Arp 220. This page: CO (2-1) integrated intensity, velocity, line width (FWHM), and the 1.3 mm continuum. CO integration limits are -320 , $+300 \text{ km s}^{-1}$. Beam is $0.^{\circ}7 \times 0.^{\circ}5$. Contours for integrated CO are 1 to 14 by 1, in units of $11.4 \text{ Jy beam}^{-1} \text{ km s}^{-1}$, with $T_b/S = 69 \text{ K Jy}^{-1}$. Contours for CO velocity are -225 to $+225 \text{ km s}^{-1}$, in steps of 25 km s^{-1} relative to 226.422 GHz ($c_{\text{lsr}} = 5450 \text{ km s}^{-1}$). Contours for CO line width are 25 to 350 km s^{-1} , in steps of 25 km s^{-1} . Contours for 1.3 mm continuum are 1 to 12 by 1, in units of $5.7 \text{ mJy beam}^{-1}$. Labels are in km s^{-1} . Next page: CO (1-0) integrated intensity, velocity, line width (FWHM), and east streamer. For all maps, the beam is $1.^{\circ}6 \times 1.^{\circ}1$, with $T_b/S = 55 \text{ K Jy}^{-1}$, and velocities are relative to 113.228 GHz ($c_{\text{lsr}} = 5410 \text{ km s}^{-1}$). Contours for CO integrated from -320 to $+300 \text{ km s}^{-1}$ are 0.1, 0.25, 0.5, then 1 to 12 by 1, in units of $11.4 \text{ Jy beam}^{-1} \text{ km s}^{-1}$. Contours for CO velocity are -200 to $+260 \text{ km s}^{-1}$, in steps of 20 km s^{-1} . Contours for CO line width are 25 to 350 km s^{-1} , in steps of 25 km s^{-1} . Labels are in km s^{-1} . Contours for CO east streamer, integrated from $+85$ to $+165 \text{ km s}^{-1}$, are 0.025 to 0.2 by 0.025, then 0.25, then 0.4 to 2.4 by 0.4, in units of $11.4 \text{ Jy beam}^{-1} \text{ km s}^{-1}$.

prominent optical dust lane at 50° (Fig. 23a), while the CO east streamer coincides with the perpendicular dust lane in the optical image (Fig. 23b).

Our model fits to the CO position-velocity diagrams of the Arp 220 disk (Fig. 21) yield a much higher dynamical mass than estimates from the IR (e.g., Doyon et al. 1994; Shier, Rieke, & Rieke 1994, 1996; Larkin et al. 1995). From the masses in Table 9, we estimate $M(<350 \text{ pc}) = 8.8 \times 10^9 M_{\odot}$ and $M(<600 \text{ pc}) = 1.5 \times 10^{10} M_{\odot}$, 3–4 times higher than the IR estimates. The millimeter CO data and the 2.3

μm CO bandhead absorption data yield different masses because the two IR nuclei do not lie on the line of nodes traced by the CO maps and because the NIR starlight is obscured and does not trace the full extent of the molecular disk.

The gas mass derived from both the dust and the CO implies a column density of $1 \times 10^{24} \text{ cm}^{-2}$ and $A_V \sim 1000$ mag through the disk, consistent with the dust having an opacity of unity at $180 \mu\text{m}$ (Emerson et al. 1984; Scoville et al. 1991). The high opacity in the far-infrared (FIR) may

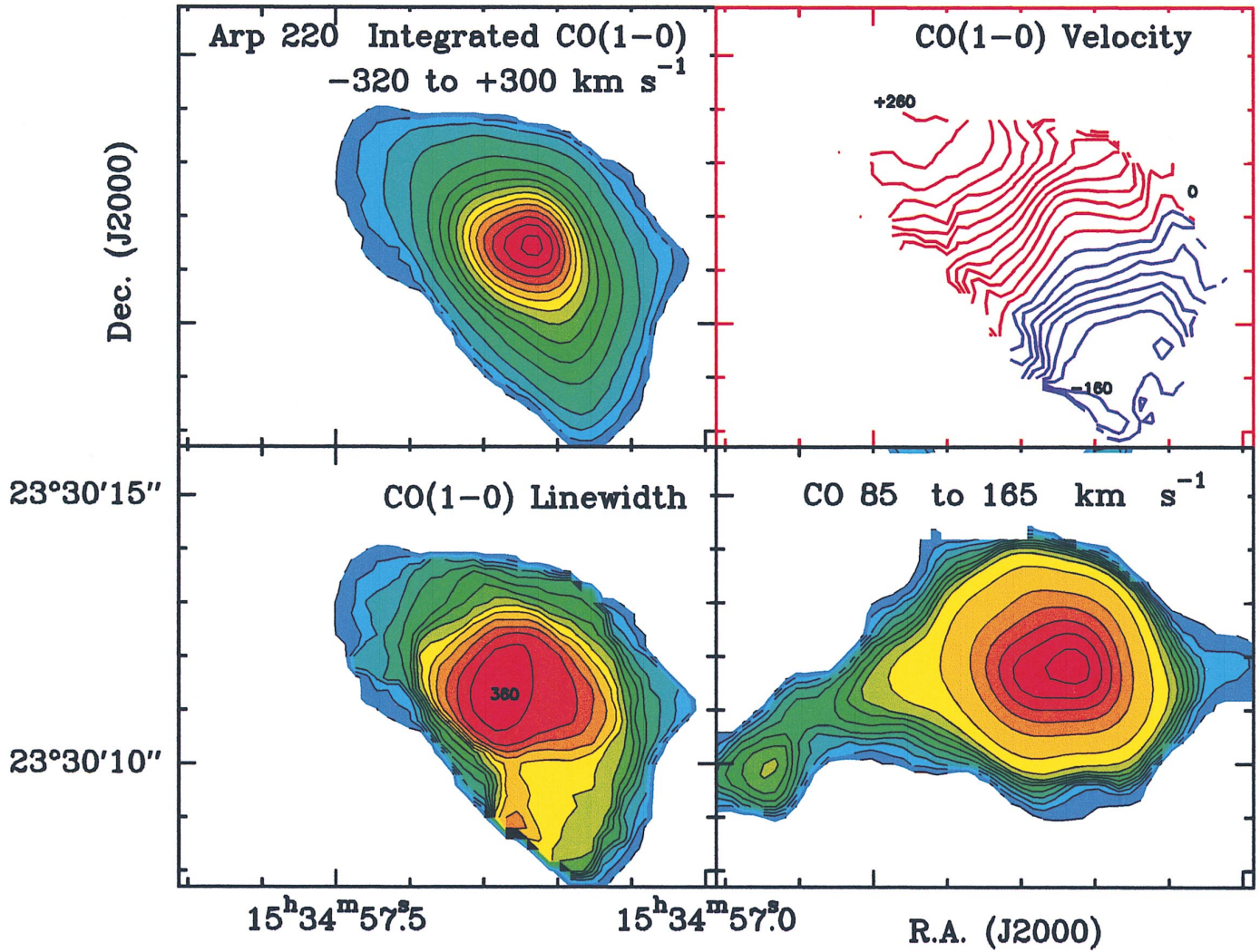


FIG. 18.—Continued

partly explain why the C^+ 158 μm line is weak in Arp 220 (Fischer et al. 1998). The ratios of fine structure lines observed by the *ISO* satellite yield an equivalent screen of $A_V \sim 45$ mag (Genzel et al. 1998). As is well known, a screen model gives only an extreme lower limit. The corresponding extinction when the emitting gas and dust are completely mixed is $A_V \sim 1000$ mag, the same as we deduce from the column density derived from the CO maps.

Figure 24 shows our model of the molecular disk and the two “nuclei.” The CO disk is inclined 40° from face-on, Arp 220 west has a radius of 68 pc, and Arp 220 east has a radius of 110 pc. The disk thickness is 90 pc, which means that the path to the near surface of the east and west *K*-band sources is 0–20 pc, which is why the two nuclei are visible at all in the *K* band. That is, although the visible extinction through the entire molecular disk is 1000 mag, the visible extinction to the near surfaces of the east and west sources is only about 50 mag, because of the shorter path. Our diagram is similar to that of Scoville et al. (1997, their Fig. 7), except that our presentation is a view from the pole of the disk. In our model, the near side is north, the far side is south. This agrees with the optical colors, which are bluer on the north side of the dust lane (Shaya et al. 1994). Since the CO east nucleus is south of the major axis, it is on the far side. The

CO disk or ring includes both nuclei, but the nuclei are oriented east-west, and hence the difference in their line-of-sight velocities does not give the full rotation speed of the disk.

Our data and model have some important consequences for the interpretation of the Arp 220 nuclear sources.

1. The rotation curve of the CO disk indicates a dynamical mass of $12 \times 10^9 M_\odot$ interior to 480 pc, which corresponds to the central bulge mass of a large spiral such as the Milky Way.

2. The gas mass in each of the two extreme starburst “nuclei” is only $6 \times 10^8 M_\odot$. Their individual luminosities are $\sim 3 \times 10^{11} L_\odot$. (About half of the Arp 220 FIR luminosity comes from the molecular disk, not the two nuclei). With an L/M ratio of 1000, corresponding to a super-starburst in its initial phase, the mass of new stars in each nucleus would be only $3 \times 10^8 M_\odot$, sufficient to explain all the *K*-band continuum luminosity. The velocity dispersion of the CO in each of the two nuclei implies a dynamical mass of $\sim 1 \times 10^9 M_\odot$, about the same as our estimate of the sum of the gas and new stars.

3. Hence, there is no room left over for old stars in the two “nuclei”; they cannot be the relics of the old nuclei of

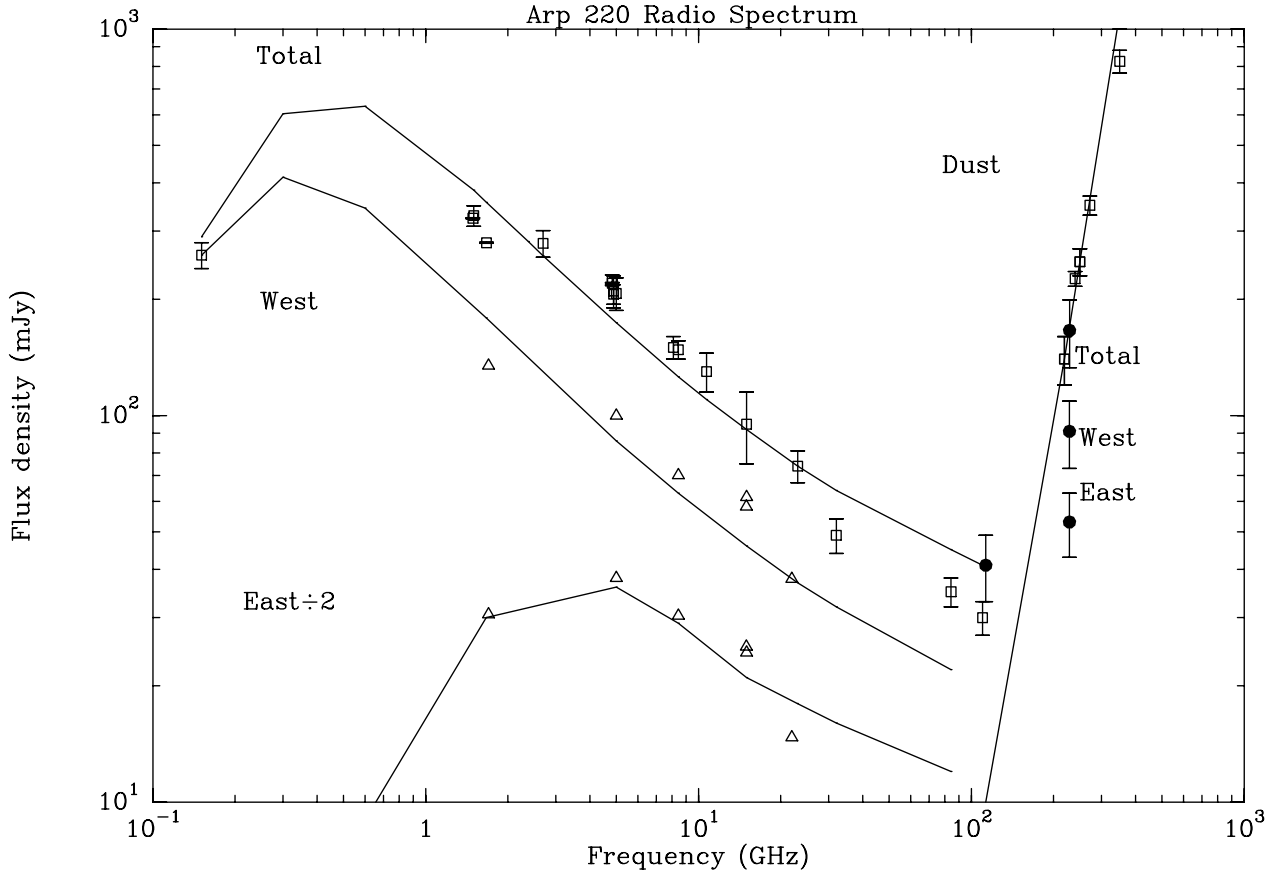


FIG. 19.—Arp 220 radio continuum spectrum. The emission below 30 GHz is nonthermal (Norris et al. 1985; Becklin & Wynn-Williams 1987; Baan & Haschick 1987; Baan et al. 1987; Norris 1988; Condon et al. 1991; Sopp & Alexander 1991 and references in their Table 3). Millimeter and submillimeter data show the increasing flux of dust emission (this paper, solid circles; Radford et al. 1991b; Scoville et al. 1991, 1997; Woody et al. 1989; Carico et al. 1992; Eales, Wynn-Williams, & Duncan 1989; and Rigopoulou et al. 1996). The curves are spectra of the form $v^{2.1+n}(1 + e^{-v/v_0})$, normalized to the observed fluxes. The free-free opacity, τ , has the form $(v/v_0)^{-2.1}$, where v_0 is the turnover frequency. The curve for the dust spectrum is for an emissivity index $n = 1.5$.

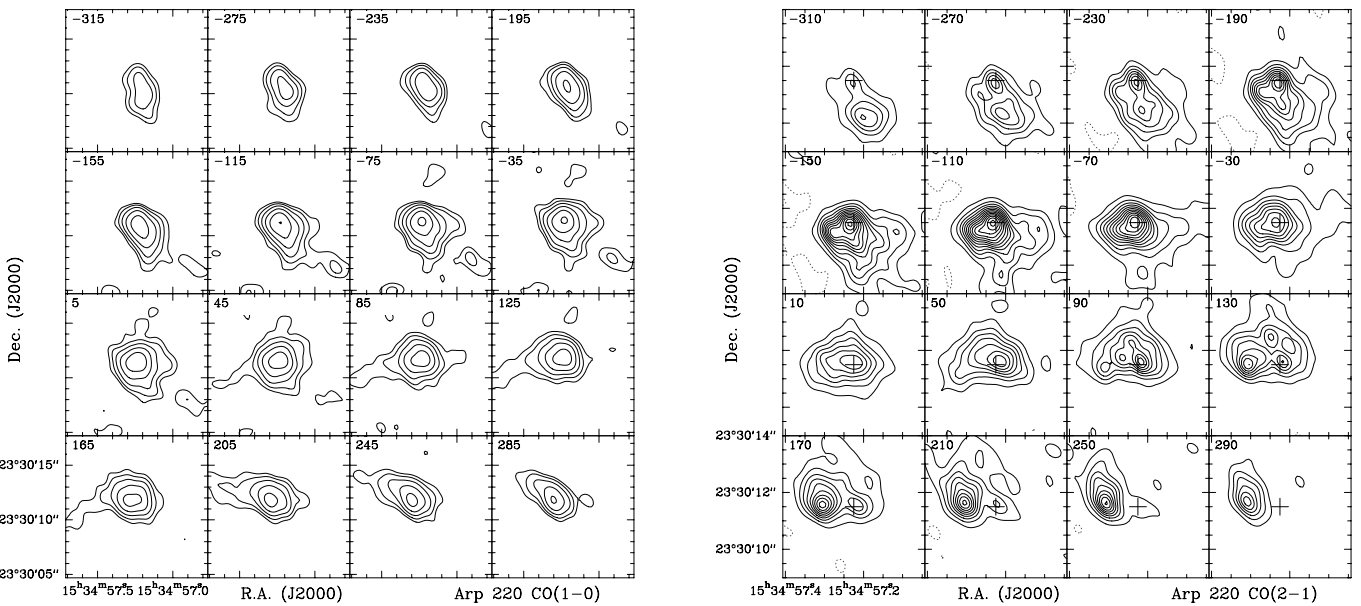


FIG. 20.—Arp 220. *Left panel:* CO (1-0) maps in 40 km s⁻¹ channels. Radial velocities (km s⁻¹, upper left of each box) are relative to 113.228 GHz ($c_{z,\text{lsr}} = 5410 \text{ km s}^{-1}$). Contours are at 1, 2, 4, 8, 16, 32, in units of 11.4 mJy beam⁻¹. Beam is 1.6' × 1.1', with $T_b/S = 55 \text{ K Jy}^{-1}$. *Right panel:* CO (2-1) maps in 40 km s⁻¹ channels. Radial velocities (km s⁻¹, upper left of each box) are relative to 226.422 GHz ($c_{z,\text{lsr}} = 5450 \text{ km s}^{-1}$). The cross marks the position of the integrated CO (2-1) west peak (see Table 2). Beam is 0.7' × 0.5', with $T_b/S = 69 \text{ K Jy}^{-1}$. The continuum has been subtracted from the CO maps. Contour unit is 50 mJy beam⁻¹. On this contour scale, the continuum from the west peak would be two contours.

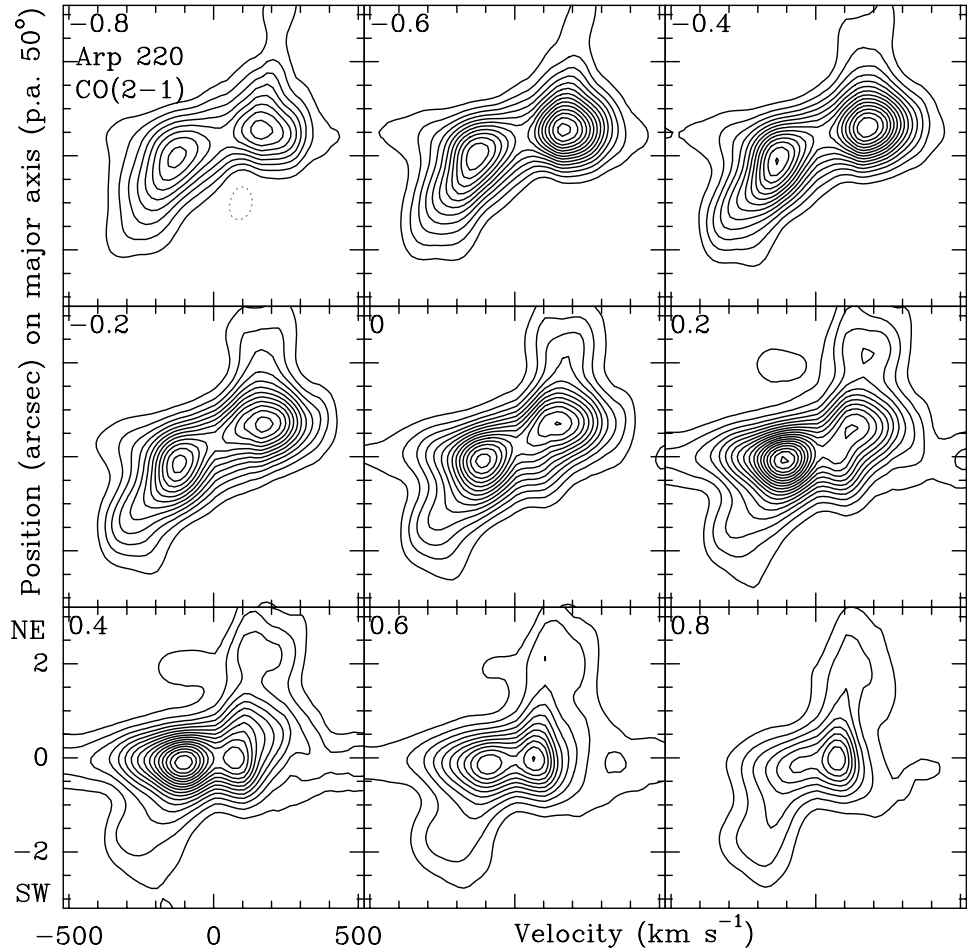


FIG. 21a

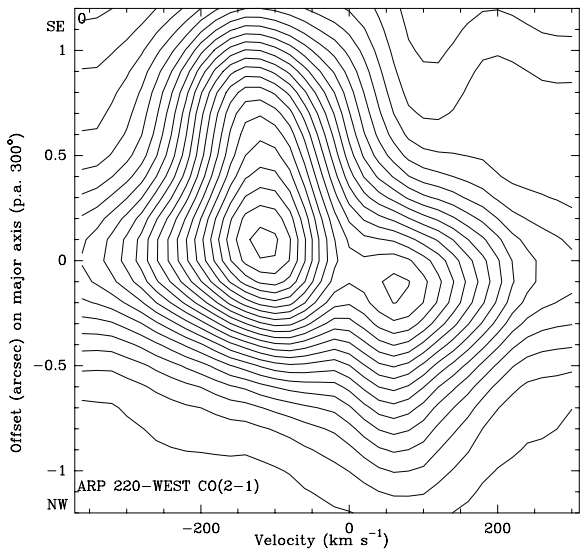


FIG. 21b

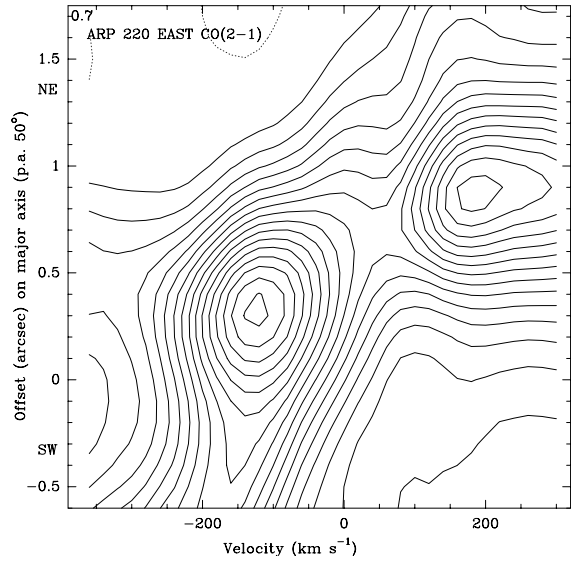


FIG. 21c

FIG. 21.—(a) Arp 220 disk CO (2–1) position-velocity cuts along the line of nodes (P.A. 50°). Labels in the upper left of each box are offsets (in arcsec) along the minor axis (northwest is positive, southeast is negative). The (0, 0) position is 15^h34^m57^s.24, 23°30'11".2 (J2000). Contour levels are 1 to 17, in units of 30 mJy beam⁻¹, with $T_b/S = 44$ K Jy⁻¹. Beam is smoothed to = 1'.0 × 0'.55 at P.A. 45°. (b) Arp 220 west CO (2–1) position-velocity cut through Arp 220 west, along a possible major axis at P.A. 300° (see text). Contour interval is 17 mJy beam⁻¹, with $T_b/S = 80$ K Jy⁻¹. The source peak is 280 mJy beam⁻¹. (c) Arp 220 east CO (2–1) position-velocity cut through Arp 220 east at P.A. 50°. Contour interval is 17 mJy beam⁻¹, with $T_b/S = 80$ K/Jy. The source peak is 380 mJy beam⁻¹. For (b) and (c), the restoring beam is 0'.6 × 0'.5 at P.A. 120°, and the (0, 0) position is 15^h34^m57^s.225, 23°30'11".5 (J2000) (the western continuum peak). In all these position-velocity diagrams, velocity is relative to 226.422 GHz ($cz_{lsr} = 5450$ km s⁻¹).

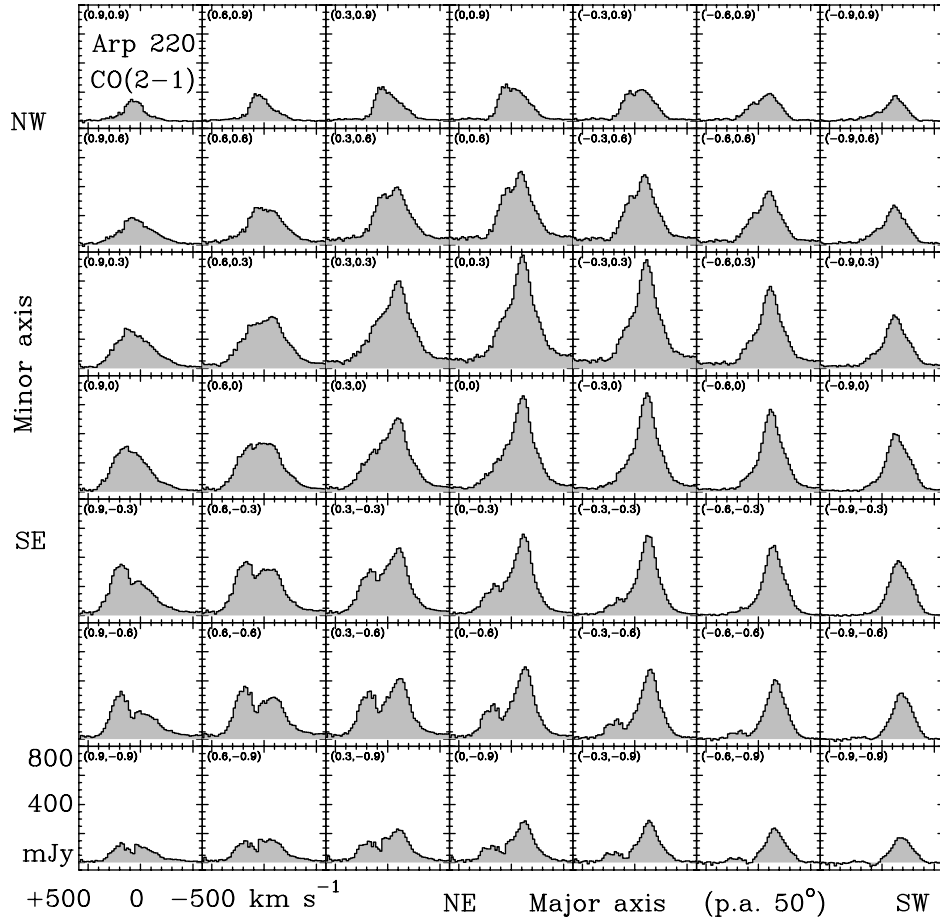


FIG. 22.—Arp 220 CO (2–1) spectra. In each box, the vertical axis is CO intensity, and the horizontal axis is radial velocity relative to 226.422 GHz ($cz_{lsr} = 5450 \text{ km s}^{-1}$). In the upper left of each box are offsets (in steps of $0.^{\circ}3$) on the kinematic major and minor axes, relative to $15^{\text{h}}34^{\text{m}}57\text{s}.24, 23^{\circ}30'11\text{''}.2$ (J2000). Beam is smoothed to $1.^{\prime}1 \times 0.^{\prime}6$ at P.A. 34° , with $T_b/S = 34 \text{ K Jy}^{-1}$.

the premerger galaxies. Furthermore, there is no observational evidence—radio, infrared, or optical—that they contain old stars.

4. In any case, the masses of the two “nuclei” are negligible compared to the mass that controls the motion of the molecular disk. Furthermore, the two “nuclei” of Arp 220 have radial velocities indicating that they take part in the general disk rotation, i.e., that they share the general rotation in the potential of the old bulge, and are dominated by its gravity, not their own.

5. In our interpretation, the two “nuclei” of Arp 220 are not the premerger nuclei at all. We think they are just large ensembles of preexisting GMCs that have been strongly compressed upon their infall into the old bulge potential as a result of the merger. The masses of these large, compressed gas structures can reach $10^9 M_{\odot}$, and the strong compression, in about one orbital period, leads to the extreme starbursts, with luminosities of a few times $10^{11} L_{\odot}$ from each compact 100 pc structure. These extreme starbursts power the ultraluminous galaxies. We are not seeing the birth of quasars.

8.3. Arguments for a Starburst

What produces Arp 220’s luminosity? We think that it is stars, for three reasons: (1) there is no obvious AGN, (2) there are enough ionizing photons for a starburst, and (3) there is enough dense molecular gas to make stars.

1. *Arp 220 has no AGN lines.* The mid-IR lines of [O IV] and [Ne V] are *not* detected (Sturm et al. 1996; Lutz et al. 1996). The Br α width of 1300 km s^{-1} reported by Depoy, Becklin, & Geballe (1987) as evidence for an AGN has not been confirmed by later measurements (Goldader et al. 1995; Larkin et al. 1995).

2. *Arp 220 has no AGN in the radio continuum.* New VLBA maps (Smith et al. 1998b) indicate all the VLBI point sources are young radio supernovae in a dense medium, with radio luminosities comparable to SN 1986J in NGC 891.

3. *The radio nuclei are extended starburst regions.* At centimeter wavelengths, their diameters are: west, $0.^{\prime}21 \times 0.^{\prime}14$ (72×48 pc); east, $0.^{\prime}32 \times 0.^{\prime}19$ (110×64 pc) (Condon et al. 1991). The source extent, the low brightness at 5 GHz, and the high FIR-to-radio flux ratio all show the nonthermal radio continuum is starburst-dominated, not AGN-dominated (Sopp & Alexander 1991; Condon et al. 1991; Baan & Haschick 1995).

4. *Arp 220 is not a “warm” ultraluminous galaxy.* IR ultraluminous galaxies with an AGN, such as Mrk 231, Mrk 1014, and 08572+3915, have warm mid-IR colors ($f_{2.5}/f_{6.0} > 0.2$) and bright, symmetric nuclei resembling reddened QSOs (Surace et al. 1998). Unlike these sources, Arp 220 has strong FIR and weaker mid-IR flux ($f_{2.5}/f_{6.0} = 0.08$). It has been argued that a QSO is hidden in Arp 220, but the silicate absorption depth at $10 \mu\text{m}$ in Arp 220 (e.g.,

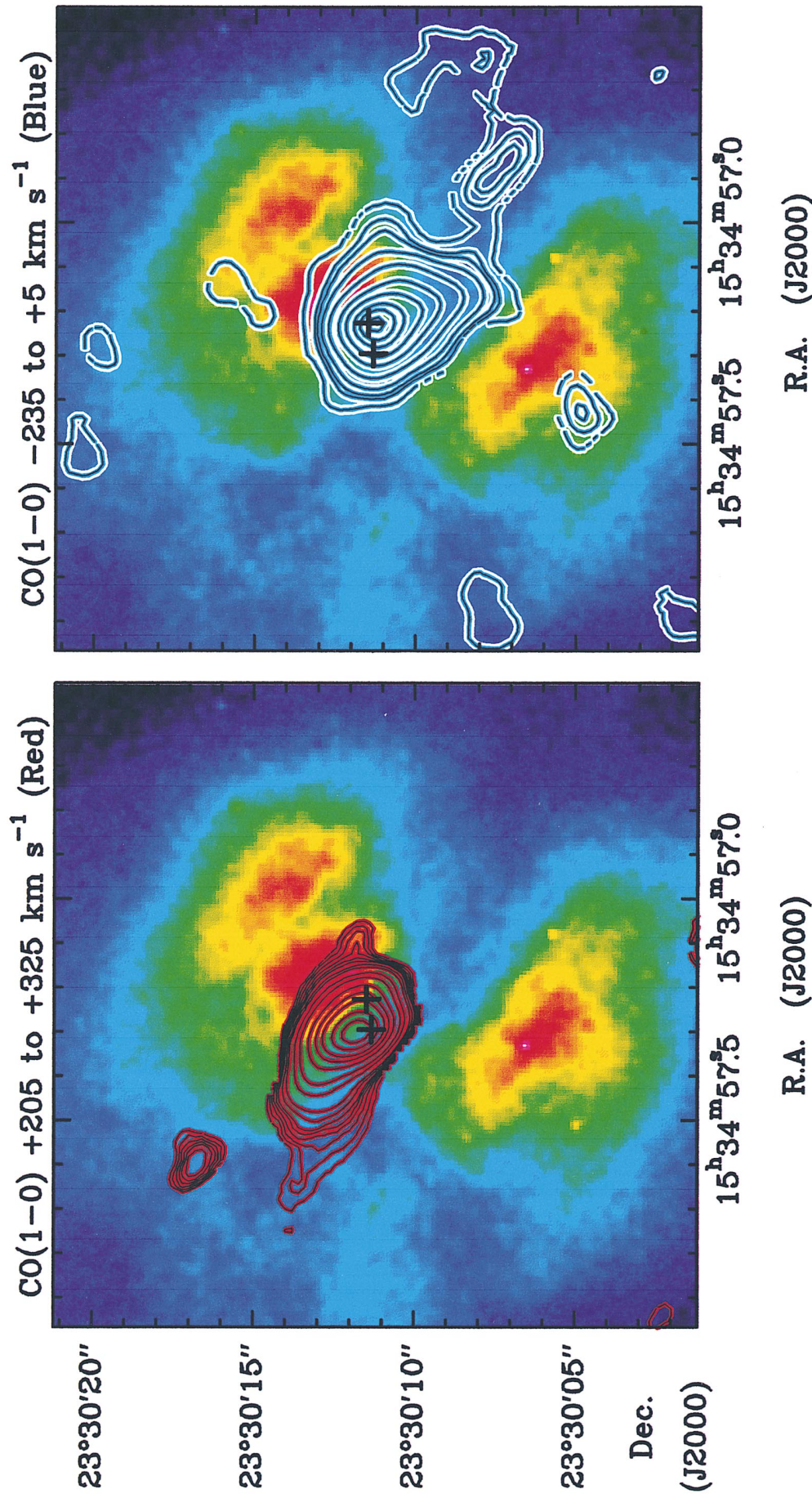


FIG. 23a

FIG. 23.—Arp 220 CO contours superposed on a false-color presentation of the *HST* V-band image of Arp 220 (Shaya et al. 1994). (*a*) CO (1–0) emission mapped with a beam of $1\farcs6 \times 1\farcs1$, with $T_b/S = 55$ K Jy^{-1} , integrated in two different velocity ranges, relative to $c_{2\text{lsr}} = 5410 \text{ km s}^{-1}$. *Left panel:* redshifted CO (1–0) emission from +205 to +325 km s^{-1} ; contours are 0.75 to 1.75 by 0.25, 2, 2.5, 3, 4.5, 6, 9, 12, 15, 20, and 25, in units of $1.14 \text{ Jy beam}^{-1}$. *Right panel:* blueshifted CO (1–0) emission integrated from –235 to +5 km s^{-1} , with contours 0.75, 2.5, 3.5, 6, 12, 24, 36, 50, 60, and 70, in units of $1.44 \text{ Jy beam}^{-1}$. (*b*) CO (1–0) emission in the east streamer and CO (2–1) emission. *Left panel:* CO (1–0) emission in the east streamer, integrated from +85 to +165 km s^{-1} ; contours and beam are as in (*a*). *Right panel:* CO (2–1) emission integrated from –320 to +300 km s^{-1} , relative to $c_{2\text{lsr}} = 5450 \text{ km s}^{-1}$, with contours 20, 30 to 180 by 30, then 240, in units of $0.57 \text{ Jy beam}^{-1} \text{ km s}^{-1}$; beam is $0\farcs7 \times 0\farcs5$, with $T_b/S = 69 \text{ K Jy}^{-1}$. The crosses indicate the radio nuclei at centimeter wavelengths.

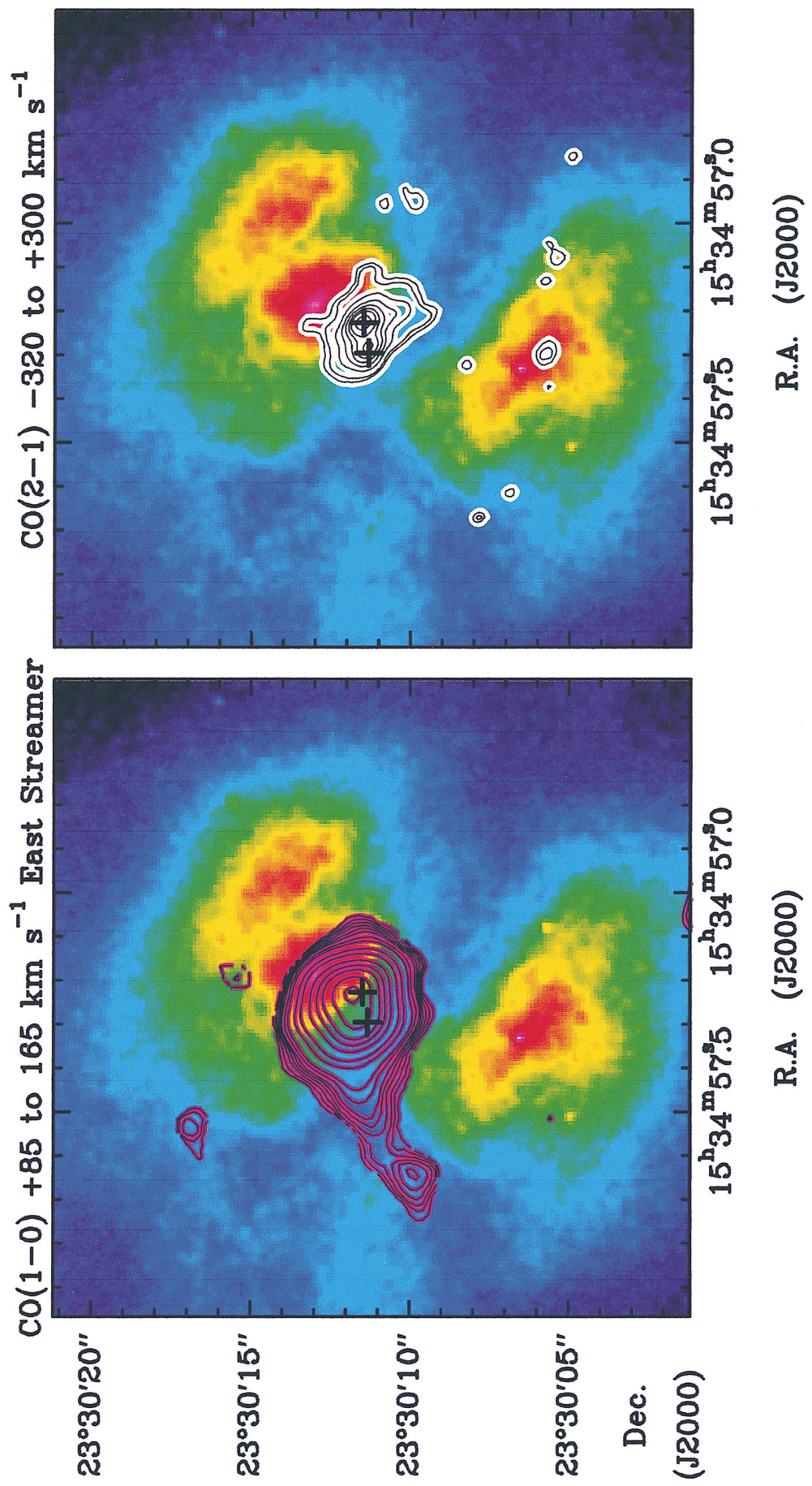


FIG. 23b

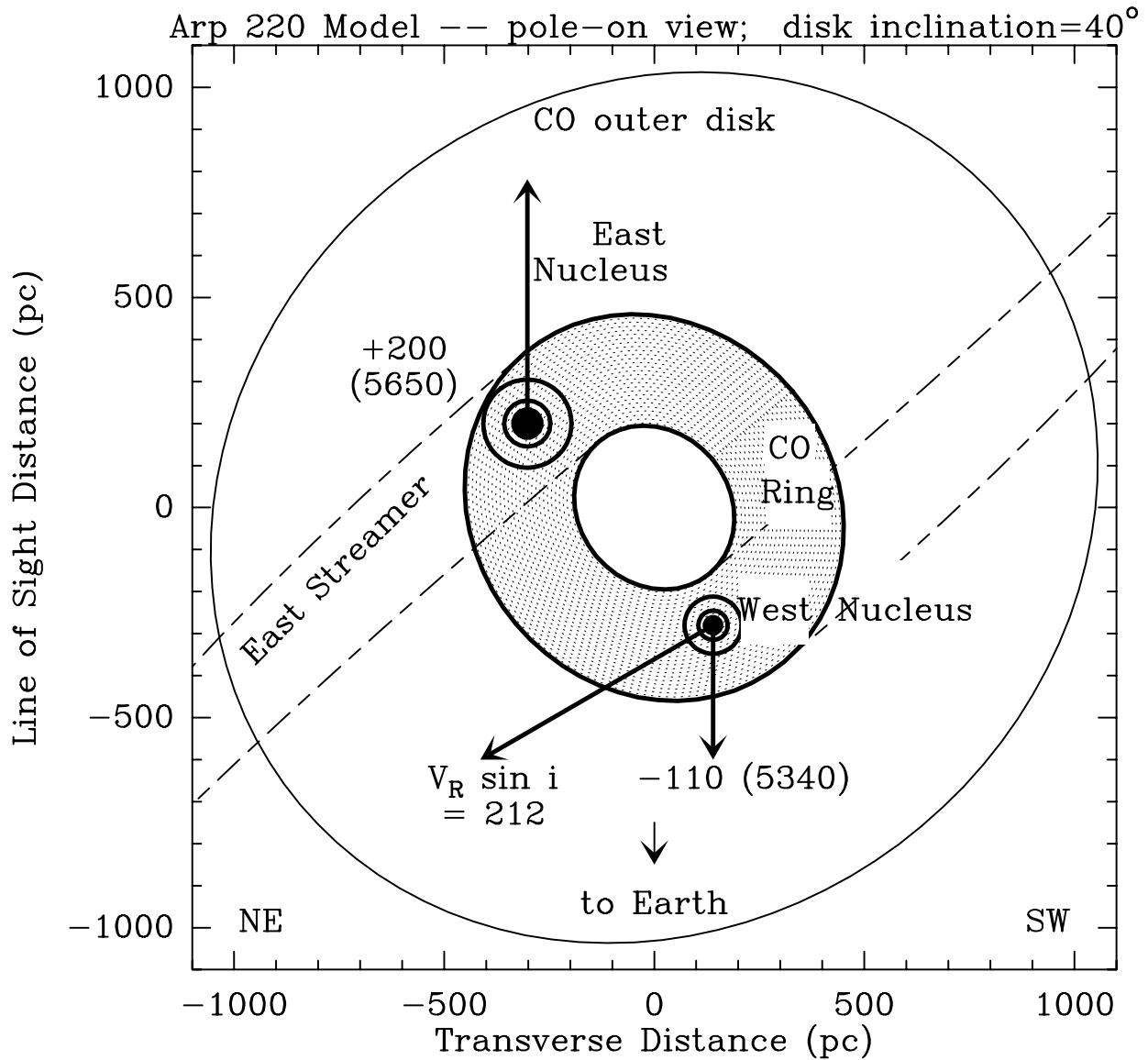


FIG. 24.—Model of the eastern and western nuclei in the molecular disk of Arp 220. The rotation velocity is 330 km s^{-1} , and the view is pole-on. The arrows indicate the observed radial components along the line of sight, at a disk inclination of 40° from face-on. Velocities are relative to a systemic velocity of $cz_{\text{lsr}} = 5450 \text{ km s}^{-1}$. Labels are in km s^{-1} , and values in parentheses are cz_{lsr} .

Smith, Aitken, & Roche 1989; Dudley & Wynn-Williams 1997) has been greatly overestimated, as a consequence of the strong PAH lines directly adjacent to the silicate feature (Genzel et al. 1998), so a deeply embedded AGN is not required.

5. *The diffuse OH megamasers do not indicate black holes.* A new VLBI study (Lonsdale et al. 1998) shows that Arp 220 has two OH megamaser components in each nucleus, one diffuse and the other compact. The diffuse megamaser component arises in the extended starburst medium, and can be explained by IR pumping via photons absorbed in the 35 and $53 \mu\text{m}$ lines of OH. The observed 9 Jy depth of the $35 \mu\text{m}$ OH line can only be explained by absorption against an extended source (Skinner et al. 1997). The compact OH megamasers, probably collisionally pumped shocks, are currently the only evidence for possible AGNs in Arp 220 (Lonsdale et al. 1998), but it is hard to understand why such AGNs would have no associated radio-continuum core jet sources.

8.4. The Ratio of Bolometric Flux to Ionizing Flux Resembles That in Sgr B2

From the observed Bry flux, Armus et al. (1995a) and Shier, Rieke, & Rieke (1996) estimated that $\leq 10\%$ of Arp 220's luminosity came from a starburst. Armus et al. noted, however, that if they had underestimated the K-band extinction, then a starburst could power the source. A higher NIR extinction is indeed required by the high column densities found from the CO maps. From the radio free-free continuum, Scoville et al. (1991; 1997) claimed that there were not enough ionizing photons for a starburst to power Arp 220. We think that this expectation was wrong, because Galactic star-forming regions such as W49, W51, and Sgr B2 have FIR luminosities greatly exceeding the Lyman luminosities derived from their radio fluxes. In compact H II regions such as W3 (OH), or in our Galactic center, the FIR excess is a factor of ~ 20 (e.g., Zylka et al. 1995).

In H II regions with densities $>10^3 \text{ cm}^{-3}$, most of the Lyman photons heat dust rather than ionizing the gas (Jennings 1975; Panagia 1977; Fazio 1978; Mezger 1985), so the Lyman photon rate derived from the radio flux is only a lower limit. We can estimate this lower limit to Arp 220's Lyman continuum photon flux from the continuum at 113 GHz, which includes 15 mJy from the synchrotron spectra and 13 mJy from dust (Fig. 19). This leaves 13 mJy as optically thin free-free flux, and implies a Lyman continuum photon rate of $>1 \times 10^{55} \text{ s}^{-1}$. Similar lower limits come from the H92 α radio recombination line (Zhao et al. 1996) and the low-frequency turnover of the radio spectra of the two nuclei (Fig. 19), due to free-free absorption in ionized gas with an emission measure of $10^8 \text{ cm}^{-6} \text{ pc}$ and a mass of $5 \times 10^7 M_\odot$ (Sopp & Alexander 1991).

For comparison, in the Galactic giant H II region and molecular cloud Sgr B2, the FIR power is 10 times the ionizing luminosity derived from the radio (Gatley et al. 1978). Sgr B2 resembles Arp 220's molecular gas in column density, strong molecular lines, and FIR opacity, but no one has ever claimed that Sgr B2's FIR excess proves it is powered by a black hole. Arp 220 and Sgr B2 both have the same ratio of FIR flux (in W m^{-2}) to radio free-free flux (in Jy), and hence the same FIR excess. So, our lower limit on Arp 220's ionizing flux, scaled by the Sgr B2 template, yields exactly Arp 220's FIR luminosity of $1.2 \times 10^{12} L_\odot$, and is indeed compatible with a starburst. Similar conclusions are reached by Genzel et al. (1998) from ISO line data on the ionizing flux.

8.5. Arp 220 has plenty of Gas for a Starburst

Our models yield gas masses of $0.6 \times 10^9 M_\odot$ for Arp 220 west, $1 \times 10^9 M_\odot$ for Arp 220 east, and $3 \times 10^9 M_\odot$ for the disk to $R_2 = 1.2 \text{ kpc}$ (Table 9). The total gas mass is $5 \times 10^9 M_\odot$, about 6 times lower than previous estimates made using a standard ratio of gas mass to CO luminosity. Our value agrees with the gas mass of $3.5 \times 10^9 M_\odot$ obtained by Sturm et al. (1996) from the H₂ lines at 6.9 and 17 μm , although this latter value depends sensitively on the assumed temperature. Our method differs from that of Scoville et al. (1997), who assumed that all the dynamical mass is in gas, rather than in stars, thereby forcing their model CO disk to be only 16 pc thick at $R = 250 \text{ pc}$ and to have a mean density of $1.5 \times 10^4 \text{ cm}^{-3}$. Because we do not assume that all the mass is gas, we derive a disk thickness of 80 pc and a lower mean density than Scoville et al. (1997). Our higher resolution data indicate that the gas density is highest at the two nuclei, not at the center of the molecular disk, as in the model of Scoville et al. (1997), and our value for the total gas mass is therefore a factor of 2 lower than their estimate.

Even the lower molecular gas mass, however, is about the same as in the entire disk of a gas-rich spiral. This is enough gas for a huge nuclear starburst. In the Arp 220 inner disk, the gas surface density is 100 times the peak value in the Milky Way 4 kpc molecular ring and more than 20 times the surface density in the inner few hundred pc of our Galaxy. To estimate the stellar mass in the nuclear bulge, we adopted a global luminosity-to-starburst mass ratio in the Arp 220 disk of $300 L_\odot M_\odot^{-1}$, based on starburst L/M ratios from the models of Leitherer & Heckman (1995). This gives an estimate of the mass in newly formed stars from the current merger-induced starbursts. Subtracting this mass and the gas mass from the dynamical mass then gives a

rough estimate of the mass in old, premerger stars. The resulting bulge mass is $8 \times 10^9 M_\odot$ within $R = 480 \text{ pc}$ (Table 11), about the same as in a large galaxy like our own (e.g., Oort 1977). The starburst interpretation thus implies that old stars are a significant part of the dynamical mass.

8.6. Arp 220 West has 25% of the Total Luminosity

The CO lines, the 1.3 mm dust flux, and the centimeter radio continuum all suggest that the most currently active starburst is Arp 220 west. Its radius of 68 pc and dust temperature of 75–80 K imply a blackbody luminosity of $3 \times 10^{11} L_\odot$, or about 25% of Arp 220's total IR luminosity of $1.3 \times 10^{12} L_\odot$, as expected from the $R^2 T_d^4$ ratio of the west and disk sources. This estimate also agrees with the fraction of the mid-IR flux absorbed by the 35 μm OH line at 5320 km s^{-1} (Skinner et al. 1997), the velocity of Arp 220 west. If the Lyman continuum scales as the FIR luminosity, then Arp 220 west has 1000 times the ionizing flux of 30 Doradus, which is $10^{52} \text{ photons s}^{-1}$ (Kennicutt & Chu 1994), from 2400 OB stars in a region of comparable size (Parker 1993). Because Arp 220 west is small and the dynamical timescale is short, its starburst must be younger (age $5 \times 10^6 \text{ yr}$) than that in the larger Arp 220 disk. The initial phase of a compact starburst can be highly luminous, reaching L/M ratios of 1000–3000 $L_\odot M_\odot^{-1}$ (see models in Leitherer & Heckman 1995). Our estimate of the total mass (from the CO line width) and the gas mass (from the CO luminosity) suggests that in Arp 220 west, 50% to 60% of the original gas mass has already turned into the new stars in the current extreme starburst (Table 12).

9. SOURCES OBSERVED IN CO (1–0) ONLY

We observed these sources with lower resolution, and thus our kinematic models are less precise. However, all these sources show the same phenomena as the previous group of sources, with velocity gradients and line profiles that suggest rotating rings or disks.

9.1. 00057 + 4021

The galaxy IRAS 00057 + 4021 has not been well studied, despite its high luminosity of $L_{\text{IR}} = 4 \times 10^{11} L_\odot$ and its OH megamaser (Kazès, Mirabel, & Combes 1988). The R-band image by Armus, Heckman, & Miley (1987) shows a 60" (48 kpc) southeast-northwest disk, with a tidal tail stretching a farther 45" (36 kpc) southeast. In contrast to the optical light, the CO source is quite compact. Most of the molecular gas is in a 1'1" \times <0".6 core source. The CO has wider lines (140 km s^{-1} FWHM) and is more intense on the southeast side of the line of nodes than on the northwest (Fig. 25). The continuum flux from the CO source is <10 mJy at 110 GHz. This limit on the thermal dust flux is consistent with the gas mass of $9 \times 10^8 M_\odot$ deduced from our model fits to the CO.

In the position-velocity diagram along the line of nodes at P.A. 135°, the CO line has a velocity range of 300 km s^{-1} over a diameter of 3" (Fig. 25). The CO lines are blueshifted in the northwest and redshifted in the southeast. In strips parallel to the kinematic major axis, the CO spectra show the double-peak behavior of a rotating disk or ring. To the southeast, the CO profile is steep toward the red, and gently sloping toward the blue. To the northwest, the profile is reversed. The nuclear velocity gradient in CO has the same major axis as the larger scale optical isophotes. The position-velocity data and the spectra both indicate

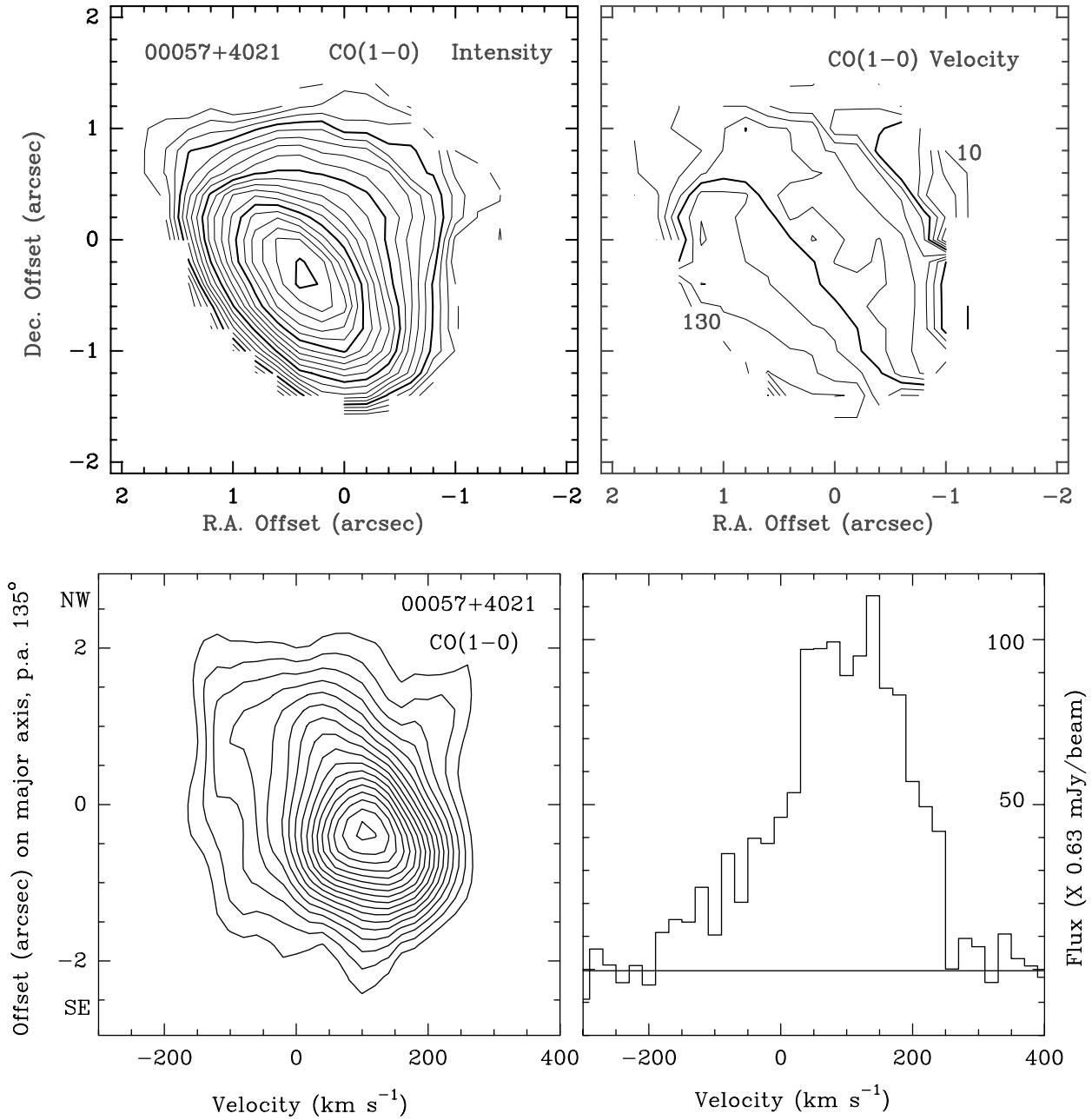


FIG. 25.—00057 + 4021. *Upper left panel:* CO (1–0) integrated over -160 , $+240$ km s^{-1} . Beam is $2\text{''}2 \times 1\text{''}1$. Contour step is $0.63 \text{ Jy beam}^{-1} \text{ km s}^{-1}$, with $T_b/S = 40 \text{ K Jy}^{-1}$. *Upper right panel:* CO velocity contours in steps of 10 km s^{-1} . Labels are in km s^{-1} . *Lower left panel:* CO (1–0) position-velocity diagram at P.A. 135° . Contours are 3 to 19 by 1, in units of $3.1 \text{ mJy beam}^{-1}$, with $T_b/S = 40 \text{ K Jy}^{-1}$. *Lower right panel:* CO spectrum in the $2\text{''}2 \times 1\text{''}1$ beam at the source peak. Position offsets are relative to $00^{\text{h}}08^{\text{m}}20\text{.58}$, $+40^{\circ}37'55\text{.5}^{\prime\prime}$ (J2000), and velocity scales are relative to 110.360 GHz ($c z_{\text{lsr}} = 13341 \text{ km s}^{-1}$).

another, lower intensity (0.5 K) disk, with a broad line width (200 km s^{-1}) in the same region as the brighter, high-density disk.

9.2. 02483 + 4302

The galaxy IRAS 02483 + 4302 is a merger with a tidal tail extending $90''$ to the west. The merger has two nuclei separated by $3\text{''}8$ east-west. In optical lines, nucleus A (west) has a Seyfert 2 spectrum, while nucleus B (east) has a LINER spectrum. The optically more intense nucleus A appears to belong to an elliptical galaxy plowing through the disk of a former spiral containing nucleus B (Kollatschny et al. 1991). The optical continuum of nucleus B comes partly from hot stars (Womble et al. 1990).

The CO (Table 2) coincides with nucleus B, supporting the idea that this was originally a gas-rich spiral. Our CO position also agrees to within $0\text{''}5$ with the 13 mJy source seen at 5 GHz (Crawford et al. 1996). At 109 GHz, the continuum flux from the CO source is < 10 mJy. This limit on the thermal dust flux is consistent with the gas mass deduced from the CO. In velocity channels 40 km s^{-1} wide, the CO source is very compact. Figure 26 shows the maps of CO integrated intensity and isovelocity contours across the source. The CO has a north-south velocity gradient, with a kinematic major axis perpendicular to the optical tidal tail extending west from the merger nuclei.

In strips parallel to the kinematic major axis, the CO spectra show the symmetric behavior of a rotating disk or

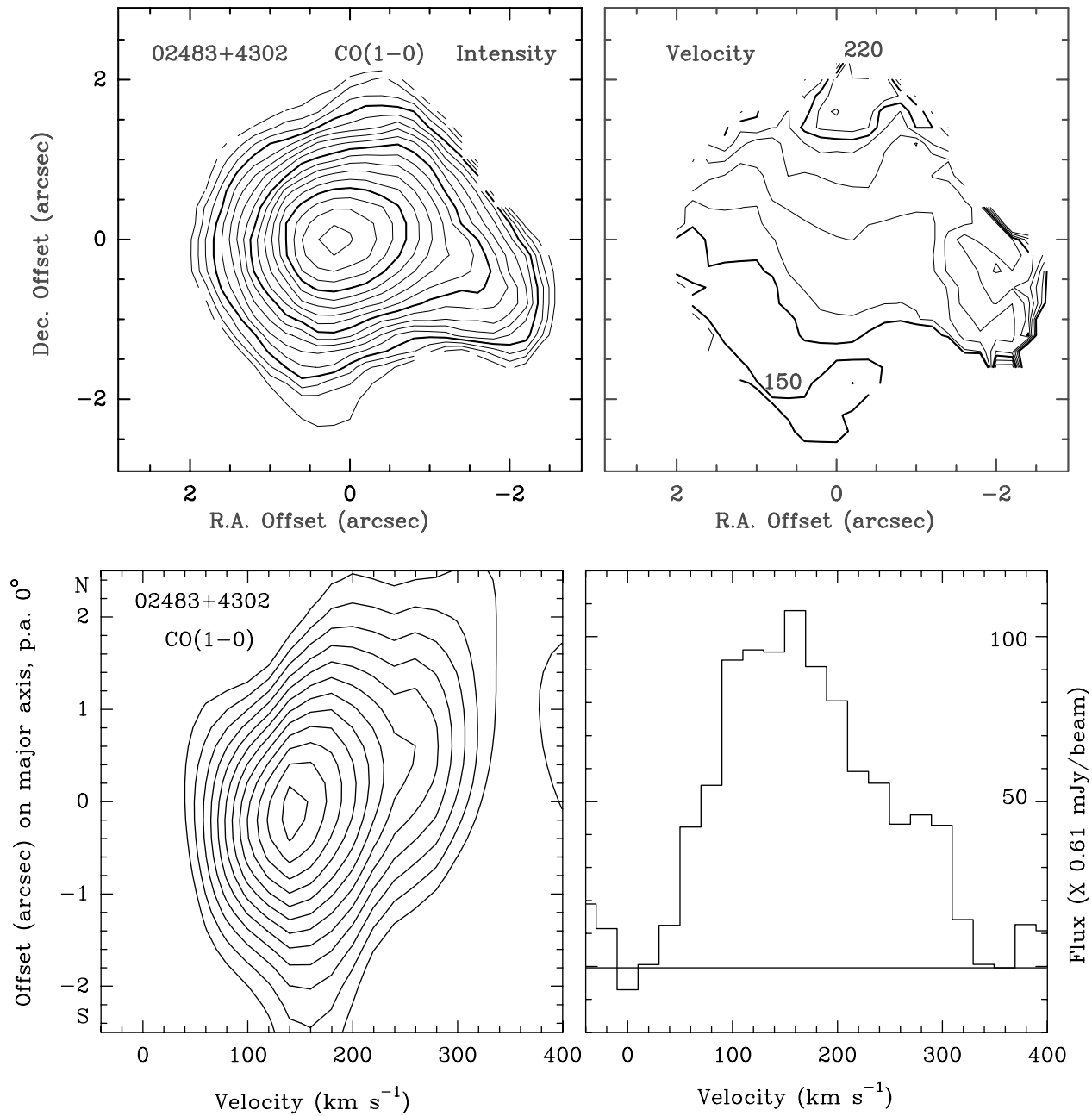


FIG. 26.—02483+4302. *Upper left panel:* CO (1–0) integrated over $+40$, $+340$ km s^{-1} . Beam is $2.^{\circ}0 \times 2.^{\circ}0$. Contour step is $0.61 \text{ Jy beam}^{-1} \text{ km s}^{-1}$, with $T_b/S = 25 \text{ K Jy}^{-1}$. *Upper right panel:* CO isovelocity contours from $+140$ to $+220$ km s^{-1} , in steps of 10 km s^{-1} . Labels are in km s^{-1} . *Lower left panel:* CO (1–0) position-velocity diagram at P.A. 0° . Contours are 3 to 14 by 1, in units of 3 mJy beam^{-1} , with $T_b/S = 32.5 \text{ K Jy}^{-1}$. Beam is $2.^{\circ}5 \times 1.^{\circ}3$. *Lower right panel:* CO spectrum at the source peak, in the $2.^{\circ}0 \times 2.^{\circ}0$ beam, with $T_b/S = 25 \text{ K Jy}^{-1}$. Position offsets are relative to $02^{\mathrm{h}}51^{\mathrm{m}}36\rlap{.}^{\mathrm{s}}01$, $+43^{\circ}15'10\rlap{.}^{\mathrm{s}}8$ (J2000), and velocity scales are relative to 109.700 GHz ($c z_{\text{lsr}} = 15225 \text{ km s}^{-1}$).

ring. In the south, the CO profile is steep toward the blue and gently sloping toward the red. In the north, the profile is reversed. The position-velocity diagram along the line of nodes shows a gradient of 200 km s^{-1} over $0.^{\circ}9$ in declination (Fig. 26). The narrow CO line width and the low optical extinction to the nucleus both suggest that the molecular disk around nucleus B is face-on.

The CO source, at $z = 0.05144$, ($c z_{\text{lsr}} = 15420 \text{ km s}^{-1}$), and the quasar Q0248+4302, at $z = 1.311$, are separated on the sky by $16.^{\circ}9$ (the galaxy-quasar separation is incorrectly listed as $3.^{\circ}5$ by Burbidge 1996 and by Hoyle & Burbidge 1996). The tidal tail that extends > 80 kpc from the two merger nuclei crosses the quasar at a projected distance of

15.4 kpc from the CO source. At this position, low-density atomic gas in the tidal tail is seen in absorption against the quasar in the Na I D and Ca II H and K lines at $z = 0.0515$ and 0.0523 , with line widths of $< 150 \text{ km s}^{-1}$ (Womble et al. 1990). There are two other absorption systems in Mg II, at $z = 0.394$ and 0.451 , from the halos of other, more distant galaxies on the line of sight to the quasar (Womble et al. 1990; Sargent & Steidel 1990; Borgeest et al. 1991). After correcting for the primary beam, we derived the quasar's continuum flux to be 190 mJy at 110 GHz in 1994 June–October. Toward the quasar, our data at 20 km s^{-1} resolution do not show any CO (1–0) absorption within $\pm 600 \text{ km s}^{-1}$ of the center frequency (Table 1), to a limit of

30 mJy, or 15% of the quasar's millimeter continuum flux. This range includes the $z = 0.0523$ ($cz = 15300 \text{ km s}^{-1}$) redshift seen in absorption against the quasar in Na I and Ca II. If the absorbing atomic gas extends 0.3–3 kpc on the line of sight, the width of the tidal tail on optical images, then the column densities derived from the Na I and Ca II lines by Womble et al. (1990) imply H I densities of $1\text{--}10 \text{ cm}^{-3}$, too low for any gas to be in molecular form.

9.3. 10565 + 2448

The main optical and NIR peak of IRAS 10565 + 2448 has strong Bry lines (Goldader et al. 1995) and H II region-type line ratios (Armus, Heckman, & Miley 1989, 1990; Veilleux et al. 1995). Murphy et al. (1996) suggest that this merger is a triple galaxy system. On their *r*-band image there is a secondary source on a tidal tail $26''$ (20 kpc) northeast of the main peak, at the same redshift. A third object with unknown redshift is $7.9''$ (6.2 kpc) southeast of the main peak. In our 500 MHz band, we detect no CO toward the other two *r*-band sources, to a limit of 20 mJy beam $^{-1}$ in 20 km s^{-1} channels. At centimeter wavelengths, there is extended emission and an unresolved, nonthermal core (Condon et al. 1991; Crawford et al. 1996).

Figure 27 shows the maps of CO integrated intensity, isovelocity contours, and CO line width. The peak of the $2.3'' \times 1.7''$ CO source coincides with the compact centimeter radio continuum core. Along the line of nodes, the CO line

profiles are very symmetric, with well-defined blueshifted peaks in the east and redshifted peaks in the west (Fig. 28). Together with VII Zw 31 and Arp 193, the galaxy 10565 + 2448 is one of the best examples of a rotating ring in our sample. In the position-velocity diagram (Fig. 29), there are two prominent peaks, with a velocity shift of 180 km s^{-1} over the central $1''$ in R.A. Models that best fit the data are those with a minimum ring radius R_{\min} in equation (1) equal to $R_0 = 230 \text{ pc}$. As with VII Zw 31 and Arp 193, filled-disk models, with $R_{\min} = 0$, give poorer fits, with much less contrast. The CO ring must be nearly face-on, because of the small separation (80 km s^{-1}) of the twin peaks, the narrow CO line width (140 km s^{-1} FWHM), and the small extent of the integrated CO intensity on the kinematic major axis. Unlike Arp 220 or VII Zw 31, there is not much CO in an outer disk beyond the nuclear ring of 10565 + 2448.

9.4. 17208 – 0014

The ultraluminous galaxy 17208 – 0014 has $L_{\text{IR}} = 2.2 \times 10^{12} L_{\odot}$ and optical and NIR line spectra that indicate H II region-type excitation and high reddening (Martin et al. 1989; Kim et al. 1995; Goldader et al. 1995; Veilleux et al. 1995). Images at the *r*-band (6550 \AA) show two tidal tails from a merger (Melnick & Mirabel 1990; Murphy et al. 1996). The innermost parts of the two tails, extending north and east to radii of $> 20 \text{ kpc}$, are nicely shown in the *r*-band image by Sanders & Kim (in Solomon et al. 1997). At $2.9''$

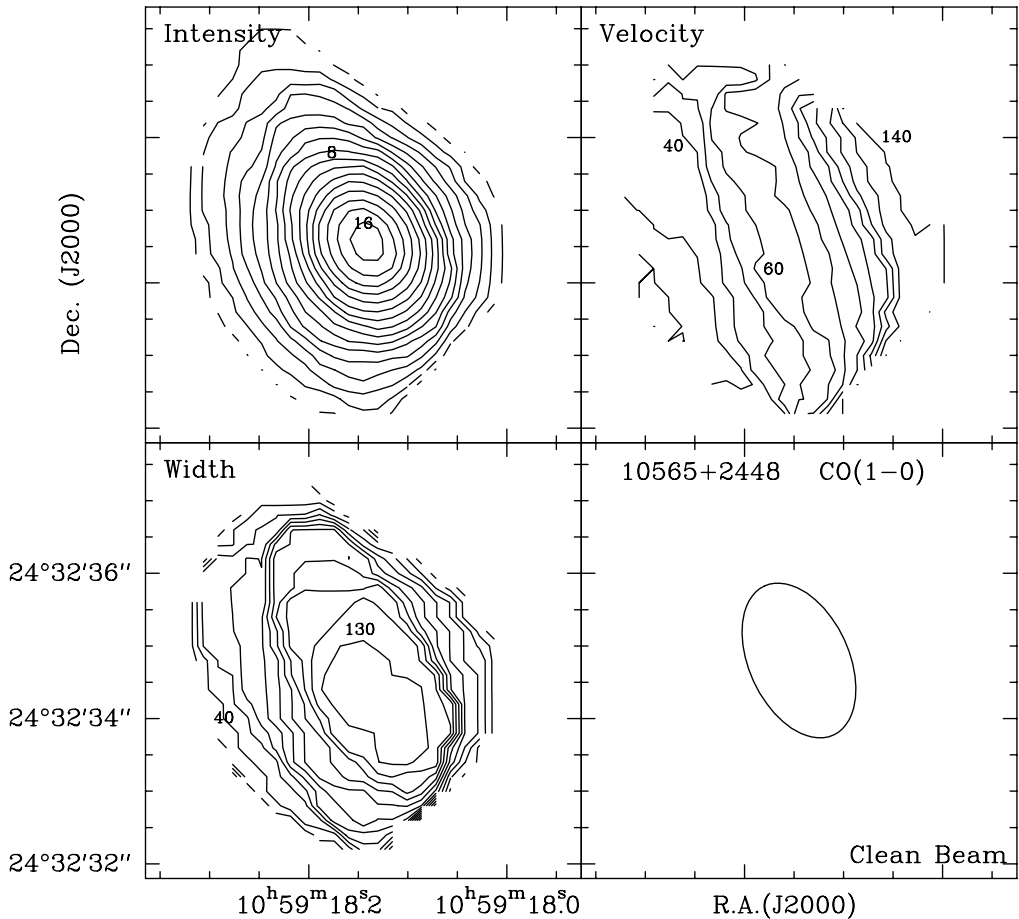


FIG. 27.—10565 + 2448 CO (1–0) integrated intensity, velocity, and line width (FWHM). Integration limits are -100 , $+220 \text{ km s}^{-1}$. Beam is $2.3'' \times 1.4''$ (lower right panel). Contours for integrated CO, 1 to 16 by 1, in units of $1.47 \text{ Jy beam}^{-1} \text{ km s}^{-1}$, with $T_b/S = 32 \text{ K Jy}^{-1}$. Contours for CO velocity are $+20$ to $+140 \text{ km s}^{-1}$, in steps of 10 km s^{-1} relative to 110.535 GHz ($cz_{\text{lsr}} = 12,846 \text{ km s}^{-1}$). Contours for CO line width are 30 to 130 km s^{-1} in steps of 10 km s^{-1} . Labels are in km s^{-1} .

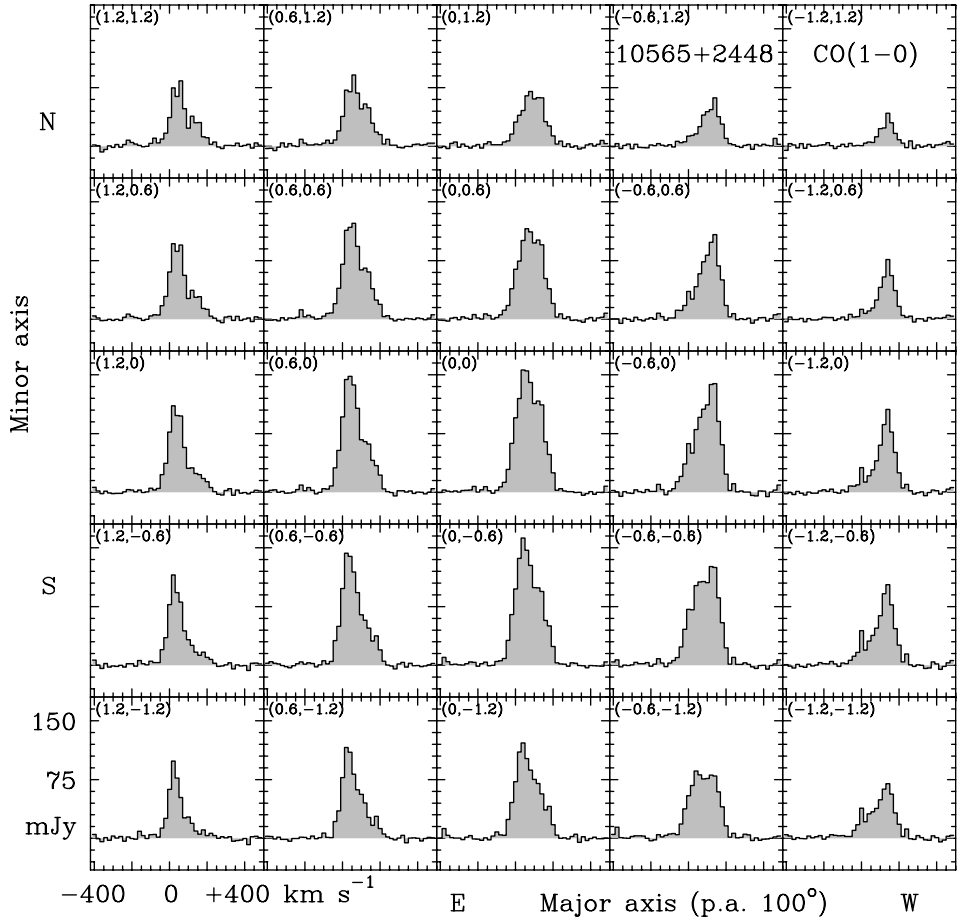


FIG. 28.—10565+2448 CO (1–0) spectra. In each box, the vertical axis is CO intensity, and the horizontal axis is radial velocity relative to 110.535 GHz ($cz_{\text{lsr}} = 12846 \text{ km s}^{-1}$). In the upper left of each box are offsets (in arcsec) on the kinematic major and minor axes relative to the CO centroid listed in Table 2. Beam is $2.^{\circ}3 \times 1.^{\circ}4$, with $T_b/S = 32 \text{ K Jy}^{-1}$.

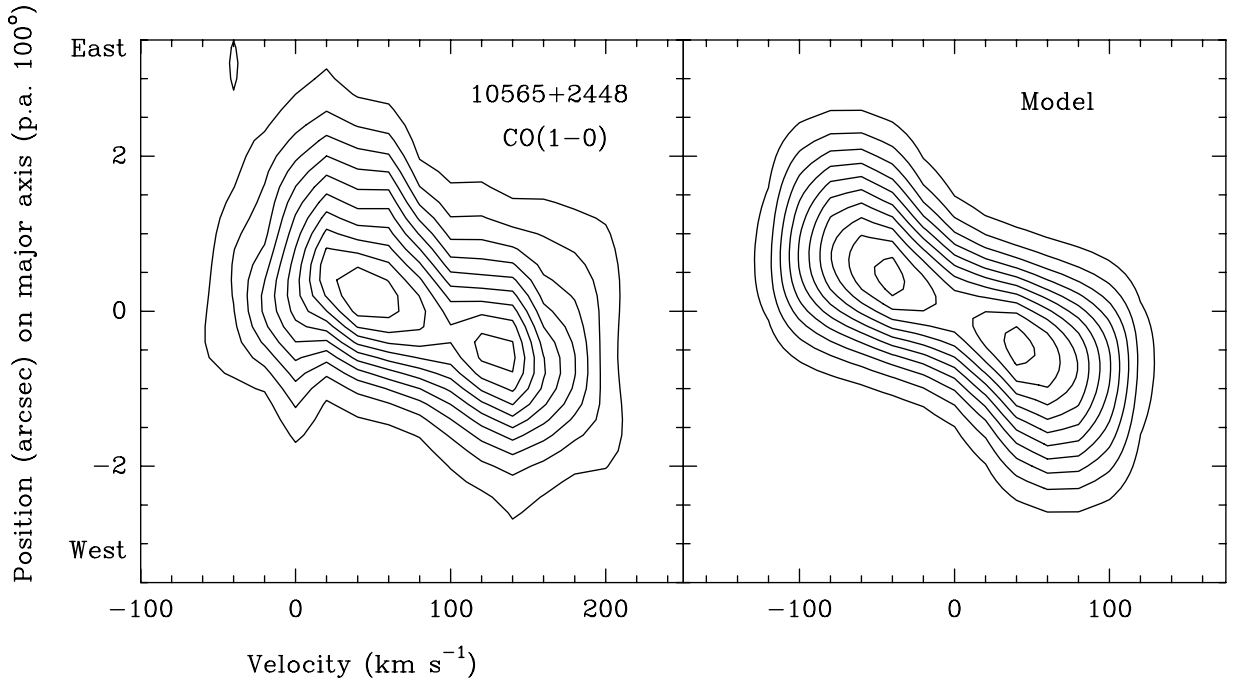


FIG. 29.—10565+2448 CO (1–0) position-velocity diagrams along the line of nodes (P.A. 100°). *Left panel:* Observed data. Contour levels are 1 to 10, in units of 15 mJy beam^{-1} , with $T_b/S = 32 \text{ K Jy}^{-1}$. Beam is $2.^{\circ}3 \times 1.^{\circ}4$. The $(0, 0)$ position is listed in Table 2. Velocity is relative to 110.535 GHz ($cz_{\text{lsr}} = 12,846 \text{ km s}^{-1}$). *Right panel:* Ring/disk model, with the parameters listed in the Tables. Contours and resolution are the same as for the observed data at the left.

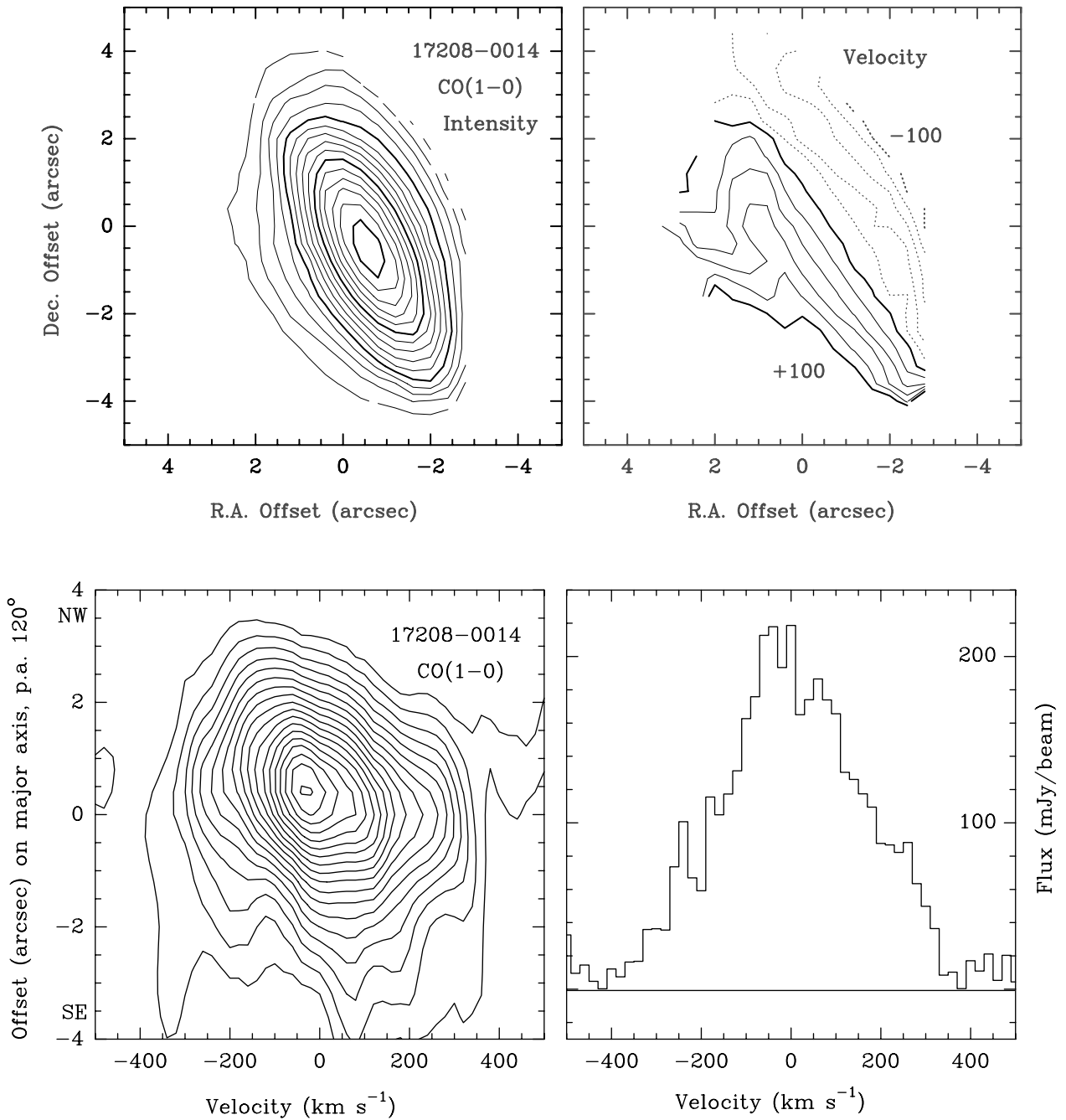


FIG. 30.—17208–0014. *Upper left panel:* CO (1–0) integrated over -360 , $+360$ km s $^{-1}$. Beam is $5\rlap{.}^{\prime}1 \times 1\rlap{.}^{\prime}6$. Contour steps are 5 Jy beam $^{-1}$ km s $^{-1}$, with $T_b/S = 12$ K Jy $^{-1}$. *Upper right panel:* CO velocity contours in steps of 20 km s $^{-1}$. Labels are in km s $^{-1}$. *Lower left panel:* CO (1–0) position-velocity diagram at P.A. 120° . Contours are 10 to 180 , in steps of 10 mJy beam $^{-1}$, with $T_b/S = 12$ K Jy $^{-1}$. *Lower right panel:* CO spectrum in the $5\rlap{.}^{\prime}1 \times 1\rlap{.}^{\prime}6$ beam at the source peak (Table 2). Position offsets are relative to $17^{\mathrm{h}}23^{\mathrm{m}}21\rlap{.}^{\mathrm{s}}99$, $-00^\circ17'00\rlap{.}^{\prime}2$ (J2000), and velocity scales are relative to 110.535 GHz ($cz_{\mathrm{lsr}} = 12846$ km s $^{-1}$).

(2.2 kpc) southeast of the nucleus, the *r*-band and *I*-band ($0.82 \mu\text{m}$) images show a secondary peak on a tidal tail. The *K*-band ($2.2 \mu\text{m}$) surface brightness has an $r^{1/4}$ profile out to a radius of 10 kpc, as in elliptical galaxies, probably due to the merger. The nucleus has a size of $1\rlap{.}^{\prime}8 \times 1\rlap{.}^{\prime}4$ in the *K* band and appears to be single, which suggests a completed merger (Zenner & Lenzen 1993; Murphy et al. 1996). The nucleus also has one of the strongest known OH megamasers, with $10^3 L_\odot$ in the 1667 MHz OH line, and a radio continuum source of size $0\rlap{.}^{\prime}32 \times 0\rlap{.}^{\prime}26$ (220 \times 270 pc; Martin et al. 1989).

Figure 30 shows the maps of CO (1–0) integrated intensity and isovelocity contours. The CO source has a size of $1\rlap{.}^{\prime}8 \times 1\rlap{.}^{\prime}6$, smaller than measured by Planesas, Mirabel, & Sanders (1991), and about the same size as the *K*-band source. The centroid of the CO source (Table 2) agrees to within $0\rlap{.}^{\prime}2$ with the centimeter radio continuum source (Martin et al. 1989). The isovelocity contours and the CO spectra show that the molecular gas is blueshifted in the northwest and redshifted in the southeast. The position-velocity diagram (Fig. 30) indicates a strong velocity gradient, with a change of 400 km s $^{-1}$ over $1\rlap{.}^{\prime}5$ at P.A. 120° .

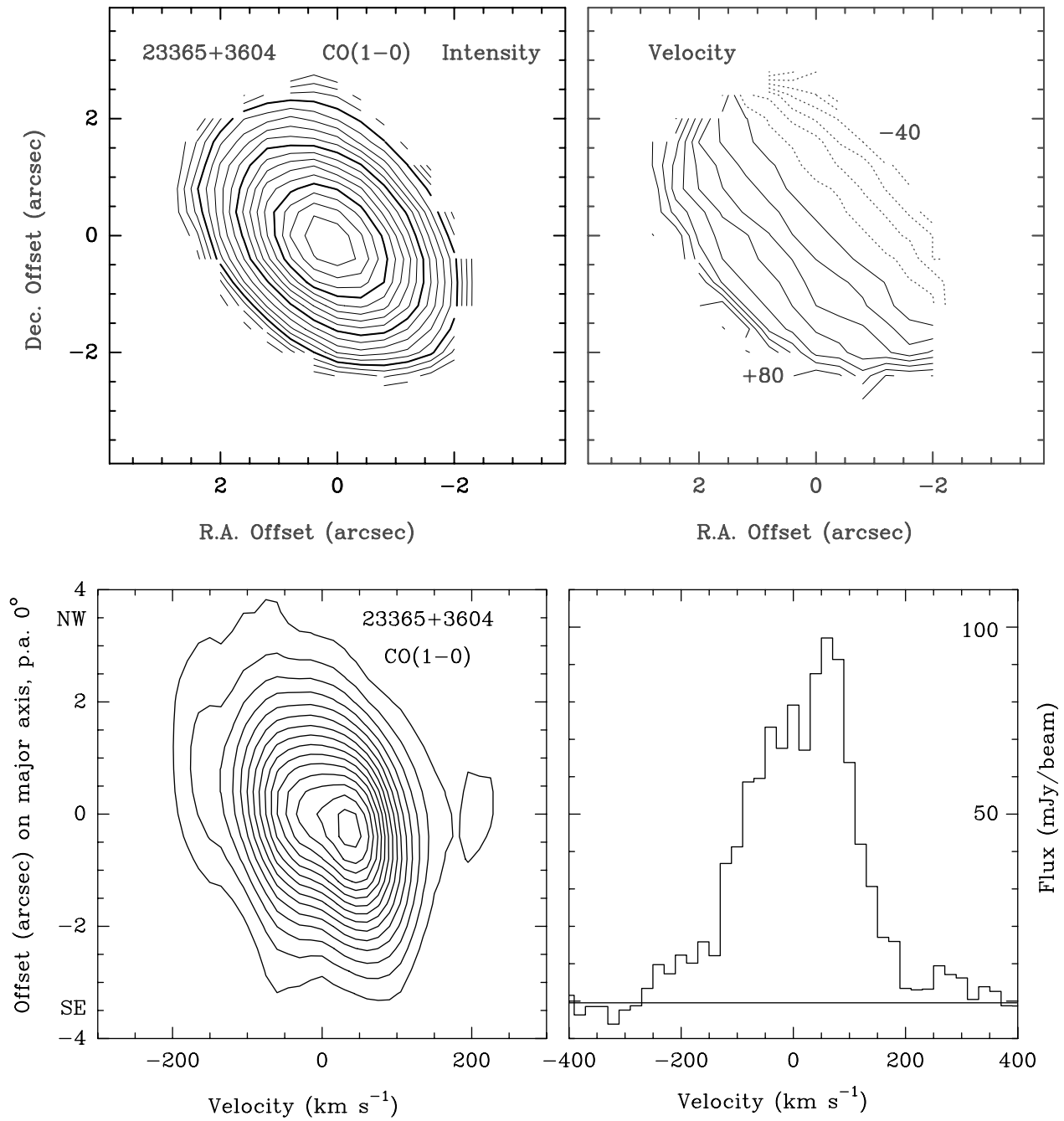


FIG. 31.—23365+3604. *Upper left panel:* CO (1–0) integrated over -240 , $+180$ km s $^{-1}$. Beam is $3.^{\circ}9 \times 2.^{\circ}5$. Contour steps are 2 Jy beam $^{-1}$ km s $^{-1}$, with $T_b/S = 11$ K Jy $^{-1}$. *Upper right panel:* CO velocity contours in steps of 10 km s $^{-1}$. Labels are in km s $^{-1}$. *Lower left panel:* CO (1–0) position-velocity diagram at P.A. 135° . Contour interval is 3 mJy beam $^{-1}$. *Lower right panel:* CO spectrum at the source peak, in the $3.^{\circ}9 \times 2.^{\circ}5$ beam. Position offsets are relative to $23^{\mathrm{h}}39^{\mathrm{m}}01\rlap{.}^s25$, $36^{\circ}21'08\rlap{.}''4$ (J2000), and velocity scales are relative to 108.292 GHz ($cz_{\mathrm{lsr}} = 19321$ km s $^{-1}$).

We interpret this angle as the line of nodes of the nuclear disk. The CO spectrum at the peak of the source (Fig. 30) has a line width of 375 km s $^{-1}$ FWHM, and 700 km s $^{-1}$ to zero intensity. At the CO peak, there appears to be a weak continuum at the 5 mJy level.

9.5. 23365+3604

On R-band images, the ultraluminous galaxy 23365+3604 has two tidal tails, but only a single, blue nucleus (Klaas & Elsässer 1991; Murphy et al. 1996). The optical spectrum (e.g., Veilleux et al. 1995) is of the LINER type, with line ratios implying shock velocities of 80 – 90 km s $^{-1}$ and preshock electron densities of 1 – 10 cm $^{-3}$ in

tenuous gas, as in old supernova remnants (Klaas & Elsässer 1991). In the nucleus, The [O III] line has a width of 260 km s $^{-1}$ FWHM (Kim et al. 1995). The source has strong Brγ and H₂ lines at 2 μm (Goldader et al. 1995). In the 6 cm radio continuum, there is a secondary source extending $1''$ south of the nucleus (Crawford et al. 1996).

In our 40 km s $^{-1}$ channel maps, the CO source is compact in all channels over a range of 320 km s $^{-1}$. The CO source has a size of $1.^{\circ}0 \times 0.^{\circ}9$, with a peak $2''$ south of the optical position listed by Klaas & Elsässer (1993). The gradient in the isovelocity contours is at P.A. 135° , and the CO spectra along this line of nodes show asymmetric profiles characteristic of a rotating ring or disk. Along this

kinematic major axis, the position-velocity diagram shows a shift of 300 km s^{-1} over $4''$ (Fig. 31).

10. DISCUSSION

10.1. Source Sizes, Gas Masses from CO Imaging, and the Ratios $M_{\text{gas}}/L'_{\text{CO}}$ and $M_{\text{gas}}/M_{\text{dyn}}$

The main results of this study are the CO source sizes: the half-widths of the integrated CO emission (Table 3), and the inner and outer disk radii from the model fits to the position-velocity diagrams and the channel maps (Table 4). The measured radii of the integrated CO correspond to the half-power radii, R_1 , derived from the kinematic data. We had previously noted that for ultraluminous galaxies, the CO (1–0) flux (Jy km s^{-1}) was ~ 4 times the $100 \mu\text{m}$ flux (Jy), as expected from a blackbody model for the FIR (Downes et al. 1993). We derived the dust temperature from the FIR fluxes, and took this to be the intrinsic CO brightness temperature. From the CO luminosity, we then predicted the mean radius, R_{CO} , for a spherical CO source (Solomon et al. 1997). Interestingly, the sizes measured with the interferometer are within a factor of 2 of the blackbody sizes. The radii R_0 and R_1 from our fits to the kinematic data (Table 4) bracket our single-dish estimate: $R_0 < R_{\text{CO}} < R_1$. The CO radii measured with the interferometer now allow us to better estimate the gas and dynamical masses (Table 9).

In the centers of ultraluminous galaxies, we find $M_{\text{gas}}/L'_{\text{CO}} \approx 0.8 M_{\odot} (\text{K km s}^{-1} \text{ pc}^2)^{-1}$, about 5 times lower than the standard value for self-gravitating molecular clouds. We had anticipated this result from single-dish data (Downes et al. 1993; Solomon et al. 1997), and it is now confirmed by the interferometer maps. We had earlier used the CO line widths and radii from our blackbody model to obtain dynamical masses, which in turn led us to revise downward the gas masses from single-dish CO luminosities. We estimated a minimum gas mass by assuming optically thin CO. These estimates, which we labeled M_{thin} (Solomon et al. 1997), are within a factor of 1.5 of the gas masses derived from our model fits to the interferometer data. Table 9 also lists the ratio of gas mass to dynamical mass, which is $\sim 1/6$ in the inner, high-density disk, and $1/10$ in the outer, low-density disks.

We showed earlier (Downes et al. 1993) that the $M_{\text{gas}}/M_{\text{dyn}}$ and $M_{\text{gas}}/L'_{\text{CO}}$ ratios are related by

$$\frac{M_{\text{gas}}}{M_{\text{dyn}}} = \left(\frac{M_{\text{gas}}}{L'_{\text{CO}}} \right)^2 \frac{1}{\alpha^2}, \quad (10)$$

where, letting $f \equiv M_{\text{gas}}/M_{\text{dyn}}$, we have

$$M_{\text{gas}} = f^{0.5} \alpha L'_{\text{CO}}. \quad (11)$$

The factor $\alpha = Cn^{0.5}/T_b$, where n is the mean H_2 number density over the whole volume and T_b is the CO brightness temperature. In the units used here, the constant $C = 2.6$ for a sphere and ~ 1.0 for a flared disk with a thickness/radius ratio of 0.15, as in some of the disks in our sample. These equations depend only on gravity, and are independent of whether the gas is self-gravitating or not, or whether the CO lines are optically thick or thin.

The derived values for $M_{\text{gas}}/M_{\text{dyn}}$ and $M_{\text{gas}}/L'_{\text{CO}}$ are compatible with starbursts. Assume that a starburst powers an ultraluminous IR galaxy, with $L/M_{\text{new}\star} = 300 L_{\odot} M_{\odot}^{-1}$ for the new stars in the burst, all the power emerging in the IR. Such galaxies typically have $L_{\text{IR}}/L'_{\text{CO}} = 200 L_{\odot} (\text{K km s}^{-1}$

$\text{pc}^2)^{-1}$. Combining the two luminosity ratios gives

$$M_{\text{new}\star} = \frac{2}{3} L'_{\text{CO}} \quad (12)$$

or $\sim 3 \times 10^9 M_{\odot}$ as the mass of new stars in the burst. Most galaxies prior to the merger would have had a rotation velocity of $\sim 250 \text{ km s}^{-1}$ at a radius of 500 pc, which implies an old stellar bulge about twice as massive as the newly formed population. Since $M_{\text{dyn}} = M_{\text{gas}} + M_{\text{new}\star} + M_{\text{old}\star}$, we have from the previous equation

$$M_{\text{dyn}} = M_{\text{gas}} + 2L'_{\text{CO}}. \quad (13)$$

Solving for the molecular gas mass yields

$$\frac{M_{\text{gas}}}{L'_{\text{CO}}} = (1 + \alpha^2)^{1/2} - 1. \quad (14)$$

This equation can be generalized to arbitrary mass ratios of the old and new stellar populations. For the Arp 220 disk, with a mean H_2 density of $\sim 500 \text{ cm}^{-3}$ and $\langle T_b \rangle = 20 \text{ K}$, these equations predict $\alpha \sim 1$, $M_{\text{gas}}/M_{\text{dyn}} = 0.2$, and $M_{\text{gas}}/L'_{\text{CO}} = 0.4 M_{\odot} (\text{K km s}^{-1} \text{ pc}^2)^{-1}$, close to the values derived from our model fits to the interferometer data. In other words, the starburst scenario is compatible with the derived ratios.

10.2. Dense Gas Traced by HCN and Extreme Starburst Regions

There is another important gas component that is better traced by emission from high dipole moment molecules such as HCN, rather than by CO. The HCN emission requires densities of $n(\text{H}_2) > 10^4 \text{ cm}^{-3}$. In giant molecular clouds in the disks of the Milky Way and normal spirals, the average HCN emission is weak, with a typical ratio of $L_{\text{HCN}}/L_{\text{CO}} = 1/20$ to $1/40$ (Gao & Solomon 1998). In the Milky Way, HCN emission is strong only in cloud cores that form high-mass stars. We showed previously that ultraluminous galaxies have abnormally high HCN luminosities (Solomon et al. 1992), with $L_{\text{HCN}}/L_{\text{CO}} = 1/4$ to $1/8$, indicating that a higher fraction of the total molecular gas is in dense $> 10^4 \text{ cm}^{-3}$ star-forming cores than in normal galaxies. The densities we derive for the smoothly distributed gas in the rotating disks (see Table 6) are typically 10 times lower than that needed for HCN excitation, except for the extreme starburst regions Arp 220 west, Arp 220 east, and the disk of Mrk 231. The denser gas responsible for the HCN emission (and CS emission) is thus not adequately accounted for in most sources by the “diffuse” CO-emitting component that fills the disk.

In Arp 220, the HCN lines we observed have the same velocities as the east and west “nuclei,” so it seems that the east and west “nuclei” alone account for most of the HCN emission. These dense, compact sources have a hydrogen column density of $0.6 \times 10^{25} \text{ cm}^{-2}$ and mean density of $20,000 \text{ cm}^{-3}$, enough to thermalize the lower rotational levels of HCN by a combination of collisions and radiative trapping. Within the Arp 220 east and west sources, the HCN emission may thus have the same intrinsic brightness temperature as the CO (2–1) emission, namely, 50 K (Table 8). Using the sizes and line widths from Tables 4 and 5, we estimate the HCN luminosity of these two regions alone to be $L_{\text{HCN}} \approx 7 \times 10^8 \text{ K km s}^{-1} \text{ pc}^2$, which is $3/4$ of the observed total (Solomon et al. 1992). These two regions thus emit only $1/4$ of the CO luminosity, but most of the HCN luminosity. Their total gas mass of $1.7 \times 10^9 M_{\odot}$ is already

accounted for in the mass budget given in Table 9. Thus, for Arp 220, only a small increase in the mass budget would be enough to account for the HCN emission.

While some of the HCN emission undoubtedly comes from dense star-forming molecular cores embedded in the (relatively) diffuse CO disks of ultraluminous galaxies, it is likely that high-density extreme starburst regions similar to Arp 220 east and west exist in most of the other ultraluminous galaxies in our sample, and are the real sources of most of the HCN emission. Arp 220 is the closest ultraluminous galaxy and has the best-resolved structure. The second closest galaxy, Arp 193 (see § 6 and Figs. 10 and 11), also shows evidence of an extreme starburst in the southeast that appears similar to the strong sources in Arp 220. We suggest that the high-density extreme starburst regions are the source of much of the HCN luminosity, but only a fraction of the CO luminosity. Most are beyond detection at our current resolution in CO emission, since their size of ≈ 100 pc would be $< 0''.14$ for all but two of the galaxies (see Table 3). These objects may then add about $1 \times 10^9 M_\odot$, or 25%, to the total gas mass in galaxies with very high HCN emission. This is less than we estimated in our 1992 paper. In line with this reinterpretation, we note that the galaxy VII Zw 31 has much weaker HCN emission than most of the others in our sample. It also has the largest CO disk, a lower $L_{\text{FIR}}/L_{\text{CO}}$ ratio (less star formation per solar mass of gas), and may not have any extreme starburst regions like Arp 220 east or west.

10.3. Stability of the Molecular Disks

The standard parameter for characterizing stability against local axisymmetric perturbations of a disk supported by differential rotation and random motion is

$$Q = \frac{\sigma_v \kappa}{\pi G \Sigma}, \quad (15)$$

where σ_v is the one-dimensional random velocity dispersion, κ is the local epicyclic frequency, and Σ is the mass surface density. (Safronov 1960; Toomre 1964; Goldreich & Lynden-Bell 1965; for a recent review of the criteria applied to gravitationally coupled stars and gas in a disk, see Jog 1996). If $Q < 1$, the structure is unstable, and large, massive star clusters may form. We used our interferometer data on the sizes, turbulent velocities, rotation velocities, and mass surface densities to estimate the stability of the nuclear disks of the ultraluminous galaxies. In our model rotation curves, the epicyclic frequencies are $\kappa \approx 2V/R = \text{constant}$ on the rising part of the rotation curve, and $\kappa \approx 2^{1/2}V/R$ on the flat part of the rotation curve. The objects in our sample have high gas mass fractions and typically have $Q_{\text{gas}} \leq 2$, with $Q_{s+g} < 1$ for stars plus gas (the regime in Fig. 1e of Jog 1996). For Arp 220, we obtain $Q_{\text{gas}} = 2.2$ at $R = 480$ pc for the gas alone, but $Q \sim 1$ for the gas plus stars. For VII Zw 31, at a radius of $R = 1100$ pc, we obtain $Q = 1.1$ and 0.9 for these two masses, respectively. These values suggest that the molecular disks of Arp 220 and VII Zw 31 are globally unstable against axisymmetric perturbations and will form massive star clusters.

Empirically, this instability in the central disks appears to produce one or more large clumps of dense molecular gas—the compact, nearly unresolved peaks seen on the CO maps. Table 12 lists some of these compact regions of dense molecular gas, which we identify with extreme starbursts.

Their typical radius of 70–100 pc may be the scale on which the two-component (stars + gas) system becomes unstable. Their mean H_2 density can reach $2 \times 10^4 \text{ cm}^{-3}$, and their mass appears to be $\sim 1 \times 10^9 M_\odot$ of gas initially, which then forms $\sim 10^6$ OB-type stars over 10^7 yr, or ~ 1000 times the number of OB stars in 30 Doradus. The total luminosity of one of these extreme starburst regions is 3×10^{11} to $1 \times 10^{12} L_\odot$. The central disk of an ultraluminous IR galaxy typically contains two or three such extreme starburst regions at any given time. It is mainly these regions that provide the input power to the ultraluminous galaxies. They heat the dust in the central disks to typical temperatures of 75 K (the blackbody fits to the colors measured by *IRAS*). Since the dust is opaque at $100 \mu\text{m}$, the disk radiates as a blackbody. The typical disk radius is 200 to 300 pc, and the Stefan-Boltzmann formula for the disk as a whole yields a luminosity of the order of $10^{12} L_\odot$, the typical output power of the ultraluminous galaxies. If these starbursts occur in the old, premerger nuclei, they change them considerably, creating a new cusp with a much greater density of stars. If the extreme starbursts occur slightly outside of the old premerger nuclei, they will form new nuclei—new cusps of high stellar density.

10.4. Why Stars Outshine Black Holes

The CO disks' radii of ~ 500 pc and rotation speeds of $\sim 300 \text{ km s}^{-1}$ yield orbital periods of 10 Myr. If their FIR luminosity of $\sim 10^{12} L_\odot$ comes from new stars, then our estimates of $L_{\text{FIR}}/M_{\text{new}\star} = 300 L_\odot M_\odot^{-1}$ imply star formation rates of $50 M_\odot \text{ yr}^{-1}$. The mass of gas plus new stars is $\sim 6 \times 10^9 M_\odot$, so in 10 rotations of the molecular disks, half the gas turns into new stars.

If part of the $\sim 10^{12} L_\odot$ luminosity came from a black hole accretion disk radiating at $L \sim 0.1 mc^2$, the accretion rate would be $\sim 1 M_\odot \text{ yr}^{-1}$, so in 10 molecular disk rotations the black hole could only accrete $\sim 1\%$ of the molecular gas. The other 99% of the gas would continue to form stars over this long period, outshining the black hole.

Alternatively, if the gas fell in faster and created a $6 \times 10^9 M_\odot$ black hole in one or two orbital periods, then the accretion rate would be $60 M_\odot \text{ yr}^{-1}$, and a standard Shakura & Sunyaev (1973) optically thick accretion disk, radiating at one-tenth the Eddington luminosity, would have a luminosity shooting up to $10^{15} L_\odot$, 1000 times more luminous than the IR ultraluminous galaxies and quasars in the local universe. If the gas fell in rapidly at an accretion rate of $60 M_\odot \text{ yr}^{-1}$, but the luminosity stayed at $10^{12} L_\odot$, then the accretion disk's radiative efficiency would be only $L = 10^{-4} mc^2$, not any more efficient than producing energy from starbursts. Although it is unlikely that such a massive, high-density accretion flow would be advection dominated (e.g., Rees 1982), if the flow were in this regime, then almost by definition the accretion disk would not be a luminous object.

The model of rapid accretion to a black hole thus poses more problems than it solves. With a very high accretion rate of $60 M_\odot \text{ yr}^{-1}$, why would the IR ultraluminous galaxies only have an output of $10^{12} L_\odot$ if their power source is a black hole? Why aren't they as luminous as the powerful quasars at high redshifts, since there is no shortage of fuel? Inversely, if the power source were a black hole accreting at a modest rate of $1 M_\odot \text{ yr}^{-1}$, it would last for 6×10^9 yr, and there would be many more ultraluminous galaxies than are observed. Since the source statistics indicate that the

ultraluminous phase in mergers lasts for $\sim 10^8$ yr, the more likely answer is that the gas is used up in forming stars, not quasars.

In summary, even in 10 rotations of the molecular disk, a black hole radiating $10^{12} L_\odot$ at high efficiency could accrete only 1% of the molecular disk's mass. So even though new stars convert matter into energy less efficiently than a standard accretion disk, they make up for this in ultraluminous IR galaxies by occurring in burst, in a 2000 times larger volume, with a 2000 times larger total mass than is available within the Bondi radius, GM_{bh}/V^2 , of a supermassive black hole. The molecular disks probably survive for at least 10 rotations. During this time, at most $10^7 M_\odot$ is accreted to a black hole. The rest of the molecular gas forms stars.

11. CONCLUSIONS

1. Rotating disks.—At subarcsecond resolution, our CO maps of ultraluminous galaxies show rotating disks of molecular gas that has been driven into the centers of the mergers. The maps of Mrk 273 and Arp 220 also show large-scale streamers or tidal tails roughly perpendicular to the nuclear disks.

2. CO only moderately opaque.—Model fits show that the observed double-peaked CO spectra and the peak-to-center contrast in the twin-peaked patterns in CO position-velocity diagrams are produced by radiative transfer through the rotating disks, in CO that is only moderately opaque. The CO (1–0) opacities are 4–10 at the peaks, and lower elsewhere in the disks.

3. High turbulence in the molecular disks.—In the Arp 220 disk, the one-dimensional velocity dispersion of the molecular gas is $\sigma = 100 \text{ km s}^{-1}$ (FWHM 230 km s^{-1}). This high turbulence is one of the reasons why the CO is less opaque than in quiescent Milky Way molecular clouds. The turbulence also determines the disk thickness and the heat input to the gas. The turbulent heat input, $M_{\text{gas}} \Delta V^3 / R$, is $\sim 10^9 L_\odot$, the same as the output from the $17 \mu\text{m}$ S(1) line of H₂, a principal cooling line (Sturm et al. 1996). The line luminosity is that expected from $10^9 M_\odot$ of gas at ~ 100 K.

4. Most of the CO luminosity comes from relatively “low-density” gas.—Except for the compact cores in Mrk 231, Mrk 273, and Arp 220, the molecular disks have true CO brightness temperatures of ~ 20 K. This is rather lower than the dust and gas kinetic temperatures, which are ~ 65 –100 K. This implies that the density over most of the molecular disk is relatively low (300 – 2000 cm^{-3}), giving subthermal excitation. The CO (2–1)/(1–0) ratios are also consistent with the CO being subthermally excited.

5. The CO lines in the molecular disks come from a continuous medium, not from self-gravitating (“virialized”) clouds.—At the densities of 10^3 cm^{-3} needed to explain the observed flux, low-density molecular clouds would be unstable against tidal shear in the rotating disks. Because we also detect high-density tracers such as HCN and CS, we estimate that $\sim 10\%$ of the gas is in highly opaque, high-density (10^5 cm^{-3}) self-gravitating clouds that are stable against tidal forces. In the outer disks, however, the CO emission may come from “normal” molecular clouds. In this outer disk gas, the volume filling factor would be ~ 0.1 , and the area filling factor 0.3, as in normal galactic disks.

6. Low dust flux consistent with lower molecular mass.—Only in Arp 220 is there significant thermal continuum flux from dust at 1.3 mm. The continuum in Mrk 231 at 3 and 1.3 mm is nonthermal. At 3 mm, no thermal continuum is

detected from dust, to limits of ~ 2 – 10 mJy, in accord with the gas masses obtained from CO, corresponding to a CO luminosity-to-gas mass conversion factor about 5 times lower than in self-gravitating clouds in the Milky Way.

7. Still lots of gas, nevertheless.—In spite of the “low” gas densities and CO line opacities, the derived gas mass is high; the mass of $\approx 5 \times 10^9 M_\odot$ is equal to the mass of molecular clouds in a large, gas-rich spiral galaxy. Within the molecular disks, the ratio of gas mass to the enclosed dynamical mass is $M_{\text{gas}}/M_{\text{dyn}} = 1/6$. The ratio of gas to total mass surface density, μ/μ_{tot} , reaches a maximum value of $1/3$ within the molecular disks. The ratio $M_{\text{gas}}/L'_{\text{CO}}$ of gas mass to CO luminosity is about one-fifth of the value in self-gravitating molecular clouds. For the galaxies in this sample, typical ratios are $M_{\text{gas}}/L'_{\text{CO}} = 0.8 M_\odot (\text{K km s}^{-1} \text{ pc}^2)^{-1}$.

8. Extreme Starburst Regions.—Four extreme starbursts are identified in the 3 closest galaxies in the sample, including Arp 220, Arp 193, and Mrk 273. These are the most prodigious star formation events in the local universe, each representing about 1000 times as many OB stars as 30 Doradus. They have a characteristic size of only 100 pc, with about $10^9 M_\odot$ of gas and an IR luminosity of $\approx 3 \times 10^{11} L_\odot$ from recently formed OB stars.

Arp 220 has 2 extreme starbursts. The integrated CO and 1.3 mm continuum maps of Arp 220 show two compact peaks. The west nucleus, at $cz_{\text{lsr}} = 5340 \text{ km s}^{-1}$, is the same as the centimeter radio and IR west peak. The CO east gas at 5330 km s^{-1} is associated with the centimeter radio east peak and its OH megamasers. The CO east gas at 5650 km s^{-1} is associated with the ionized gas in the K-band east nucleus. The IR luminosity of the compact peaks in Arp 220 can be explained by extreme starbursts in their early phases. The centimeter radio continuum, the CO intensity, and the 1.3 mm dust flux all suggest that the currently most active starburst is the west peak. Arp 220 west also shows a complex velocity structure that may indicate a bar in formation or a huge molecular outflow. The mass of these compact regions is dominated by molecular gas and young stars, not by a bulge population.

9. Regions of dense molecular gas are regions of extreme starbursts.—We suggest that the HCN emission, which is very strong in most ultraluminous galaxies, originates in the high-density extreme starburst regions similar to Arp 220 east and west. These regions are larger than ordinary GMCs, but are filled with molecular gas at a density usually found only in small cloud cores. They do not produce most of the CO luminosity, but they do emit most of the HCN luminosity. This explains the high HCN luminosity and directly relates the HCN emission to star formation, as we have suggested previously (Solomon et al. 1992).

10. Ultraluminous galaxies are powered by starbursts, not AGNs.—The CO data show that the gas in ultraluminous galaxies is in extended disks that cannot intercept all the power of central AGNs, if they exist. As a rule of thumb, if you can see the AGN in the UV/visible spectrum, then it is not heavily absorbed, and cannot be responsible for the FIR/submillimeter luminosity. Furthermore, if the rotating molecular disks were very thin (30 pc) and extended all the way into central AGNs, then their dust would be very hot, emitting most of their power at 10 – $20 \mu\text{m}$. In fact, most of the dust (and gas) observed in the ultraluminous IR galaxies is cool (70 K), emitting at 60 – $100 \mu\text{m}$, the usual temperature of dust in molecular clouds heated by starbursts. We con-

clude that in ultraluminous galaxies—even in Mrk 231, which hosts a quasar—the FIR luminosity is powered by extreme starbursts in the molecular disks, not by dust-enshrouded quasars.

We thank the telescope operators at Plateau de Bure and the IRAM staff astronomers for their help in taking the data, A. Dutrey for the use of her disk-modeling program, C. M. Walmsley for the escape probability program, and

S. Guilloteau, R. Lucas, and J. Wink for help in data reduction. We also thank H. Ungerechts for remeasuring some CO fluxes at the IRAM 30 m telescope, and P. van der Werf, R. Genzel, and N. Scoville for helpful talks. We thank the referee for many helpful comments. P. M. S. is grateful for a research award from the Alexander von Humboldt Foundation and for a senior scientific fellowship from the North Atlantic Treaty Organization.

REFERENCES

- Allen, D. A. 1976, *ApJ*, 207, 367
 Armus, L., Heckman, T. M., & Miley, G. K. 1987, *AJ*, 94, 831
 ———. 1989, *ApJ*, 347, 727
 ———. 1990, *ApJ*, 364, 471
 Armus, L., Mazzarella, J. M., Graham, J. R., Soifer, B. T., Neugebauer, G., Matthews, K., & Gaume, R. A. 1992, *BAAS*, 24, 728
 Armus, L., Neugebauer, G., Soifer, B. T., & Matthews, K. 1995a, *AJ*, 110, 2610
 Armus, L., Shupe, D. L., Matthews, K., Soifer, B. T., & Neugebauer, G. 1995b, *ApJ*, 440, 200
 Armus, L., Surace, J. A., Soifer, B. T., Matthews, K., Graham, J. R., & Larkin, J. E. 1994, *AJ*, 108, 76
 Asatrian, A. S., Petrosian, A. R., & Börngen, F. 1990, in *Paired and Interacting Galaxies*, ed. J. W. Sulentic, W. C. Keel, & C. M. Telesco (NASA CP-3098) (Washington: GPO), 201
 Baan, W. A., & Haschick, A. D. 1987, *ApJ*, 318, 139
 ———. 1995, *ApJ*, 454, 745
 Baan, W. A., van Gorkom, J., Haschick, A. D., & Mirabel, F. I. 1987, *ApJ*, 313, 102
 Becklin, E. E., & Wynn-Williams, C. G. 1987, in *Star Formation in Galaxies*, ed. C. J. Lonsdale Persson (NASA CP-2466) (Washington: GPO), 643
 Binney, J., & Tremaine, S. 1987, *Galactic Dynamics* (Princeton: Princeton Univ. Press), 76
 Boksenberg, A., Carswell, R. F., Allen, D. A., Fosbury, R. A. E., Penston, M. V., & Sargent, W. L. W. 1977, *MNRAS*, 178, 451
 Borgeest, U., Dietrich, M., Hopp, U., Kollatschny, W., & Schramm, K. J. 1991, *A&A*, 243, 93
 Bryant, P. M., & Scoville, N. Z. 1996, *ApJ*, 457, 678
 Burbidge, G. 1996, *A&A*, 309, 9
 Carico, D. P., Keene, J., Soifer, B. T., & Neugebauer, G. 1992, *PASP*, 104, 1086
 Carilli, C. L., Wrobel, J. M., & Ulvestad, J. S. 1998, *AJ*, 115, 928
 Chini, R., Krügel, E., Kreysa, E., & Gemünd, H. P. 1989, *A&A*, 216, L5
 Condon, J. J., Huang, Z. P., Yin, Q. F., & Thuan, T. X. 1991, *ApJ*, 378, 65
 Crawford, T., Marr, J., Partridge, B., & Strauss, M. A. 1996, *ApJ*, 460, 225
 Cutri, R. M., Rieke, G. H., & Lebofsky, M. J. 1984, *ApJ*, 287, 566
 Depoy, D. L., Becklin, E. E., & Geballe, T. R. 1987, *ApJ*, 316, L63
 Diamond, P. J., Norris, R. P., Baan, W. A., & Booth, R. S. 1989, *ApJ*, 340, L49
 Djorgovski, S., de Carvalho, R. R., & Thompson, D. J. 1990, *AJ*, 99, 1414
 Downes, D., Solomon, P. M., & Radford, S. J. E. 1993, *ApJ*, 414, L13
 Doyon, R., Wells, M., Wright, G. S., Joseph, R. D., Nadeau, D., & James, P. A. 1994, *ApJ*, 437, L23
 Dudley, C. C., & Wynn-Williams, C. G. 1997, *ApJ*, 488, 720
 Dutrey, A., Guilloteau, S., & Simon, M. 1994, *A&A*, 286, 149
 Eales, S. A., Wynn-Williams, C. G., & Duncan, W. D. 1989, *ApJ*, 339, 859
 Emerson, J. P., et al. 1984, *Nature*, 311, 237
 Fairclough, J. H. 1986, *MNRAS*, 219, 1p
 Fazio, G. G. 1978, in *Infrared Astronomy*, ed. G. Setti & G. G. Fazio (Dordrecht: Reidel), 25
 Fischer, J., et al. 1998, in *ISO to the Peaks*, ed. M. Kessler & M. Perry (Noordwijk: ESTEC), in press
 Gao, Yu., & Solomon, P. M. 1998, in preparation
 Gatley, I., Becklin, E. E., Werner, M. W., & Harper, D. A. 1978, *ApJ*, 220, 822
 Genzel, R., et al. 1998, *ApJ*, 498, 579
 Goldader, J. D., Joseph, R. D., Doyon, R., & Sanders, D. B. 1995, *ApJ*, 444, 97
 Goldreich, P., & Lynden-Bell, D. 1965, *MNRAS*, 130, 125
 Graham, J. R., Carico, D. P., Matthews, K., Neugebauer, G., Soifer, B. T., & Wilson, T. D. 1990, *ApJ*, 354, L5
 Guilloteau, S., et al. 1992, *A&A*, 262, 624
 Hamilton, D., & Keel, W. C. 1987, *ApJ*, 321, 211
 Hoyle, F., & Burbidge, G. 1996, *A&A*, 309, 335
 Hutchings, J. B., & Neff, S. G. 1987, *AJ*, 92, L14
 Jennings, R. B. 1975, in *H II Regions and Related Topics*, ed. T. L. Wilson & D. Downes (Berlin: Springer), 137
 Jog, C. J. 1996, *MNRAS*, 278, 209
 Kazès, I., Mirabel, I. F., & Combes, F. 1988, *IAU Circ.* 4629
 Kennicutt, R. C., & Chu, Y. H. 1994, in *Violent Star Formation from 30 Doradus to QSOs*, ed. G. Tenorio-Tagle (Cambridge: Cambridge Univ. Press), 1
 Keto, E., Ball, R., Arens, J., Jernigan, G., & Meixner, M. 1992, *ApJ*, 387, L17
 Kim, D. C., Sanders, D. B., Veilleux, S., Mazzarella, J. M., & Soifer, B. T. 1995, *ApJS*, 98, 129
 Klaas, U., & Elsässer, H. 1991, *A&AS*, 90, 33
 ———. 1993, *A&AS*, 99, 71
 Knapen, J. H., Laine, S., Yates, J. A., Robinson, A., Richards, A. M. S., Doyon, R., & Nadeau, D. 1997, *ApJ*, in press
 Kobayashi, Y., Sato, S., Yamashita, T., Shiba, H., & Takami, H. 1993, *ApJ*, 404, 94
 Kollatschny, W., Dietrich, M., Borgeest, U., & Schramm, K. J. 1991, *A&A*, 249, 57
 Koski, A. T. 1978, *ApJ*, 223, 56
 Krabbe, A., Colina, L., Thatte, N., & Kroker, H. 1997, *ApJ*, 476, 98
 Krügel, E., & Siebenmorgen, R. 1994, *A&A*, 288, 929
 Larkin, J. E., Armus, L., Knop, R. A., Matthews, K., & Soifer, B. T. 1995, *ApJ*, 452, 599
 Leitherer, C., & Heckman, T. M. 1995, *ApJS*, 96, 9
 Lipari, S., Colina, L., & Macchetto, F. 1994, *ApJ*, 427, 174
 Lonsdale, C. J., Diamond, P. J., Smith, H. E., & Lonsdale, C. J. 1998, *ApJ*, 493, L13
 Lonsdale, C. J., Smith, H. E., & Lonsdale, C. J. 1993, *ApJ*, 405, L9
 Lutz, D., et al. 1996, *A&A*, 315, L137
 Majewski, S. R., Hereld, M., Koo, D. C., Illingworth, G. D., & Heckman, T. M. 1993, *ApJ*, 402, 125
 Malkan, M. A., & Sargent, W. L. W. 1982, *ApJ*, 254, 22
 Martin, J. M., Bottinelli, L., Dennefeld, M., Gouguenheim, L., & Le Squeren, A. M. 1989, *A&A*, 208, 39
 Matthews, K., Neugebauer, G., McGill, T., & Soifer, B. T. 1987, *AJ*, 94, 297
 Melnick, J., & Mirabel, I. F. 1990, *A&A*, 231, L19
 Mestel, L. 1963, *MNRAS*, 126, 553
 Mezger, P. G. 1985, in *Birth & Infancy of Stars*, ed. R. Lucas, A. Omont, & R. Stora (Amsterdam: Elsevier), 31
 Miles, J. W., Houck, J. R., Hayward, T. L., & Ashby, M. L. N. 1996, *ApJ*, 465, 191
 Murphy, T. W., Armus, L., Matthews, K., Soifer, B. T., Mazzarella, J. M., Shupe, D. L., Strauss, M. A., & Neugebauer, G. 1996, *AJ*, 111, 1025
 Neff, S. G., & Ulvestad, J. S. 1988, *AJ*, 96, 841
 Norris, R. P. 1988, *MNRAS*, 230, 345
 Norris, R. P., Baan, W. A., Haschick, A. D., Booth, R. S., & Diamond, P. J. 1985, *MNRAS*, 213, 821
 Oort, J. H. 1977, *ARA&A*, 15, 295
 Panagia, N. 1977, in *Infrared & Submillimeter Astronomy*, ed. G. G. Fazio (Dordrecht: Reidel), 43
 Parker, J. W. 1993, *AJ*, 106, 560
 Planesas, P., Mirabel, I. F., & Sanders, D. B. 1991, *ApJ*, 370, 172
 Preuss, E., & Fosbury, A. E. 1983, *MNRAS*, 204, 783
 Radford, S. J. E., Solomon, P. M., & Downes, D. 1991a, *ApJ*, 368, L15
 Radford, S. J. E., et al. 1991b, in *Dynamics of Galaxies and Their Molecular Cloud Distributions*, ed. F. Combes & F. Casoli (Dordrecht: Kluwer), 303
 Rees, M. J. 1982, in *Am. Inst. of Physics Conf. Proc. 83, The Galactic Center*, ed. G. R. Riegler & R. D. Blandford (New York: AIP), 166
 Rieke, G. H. 1976, *ApJ*, 210, L5
 Rigopoulou, D., Lawrence, A., & Rowan-Robinson, M. 1996, *MNRAS*, 278, 1049
 Roche, P. F., Aitken, D. K., & Whitmore, B. 1983, *MNRAS*, 205, 21P
 Safronov, V. S. 1960, *Ann. d' Astrophys.*, 23, 979
 Sage, L. J., & Solomon, P. M. 1987, *ApJ*, 321, L103
 Sanders, D. B., Phinney, S., Neugebauer, G., Soifer, B. T., & Matthews, K. 1989, *ApJ*, 347, 29
 Sanders, D. B., Young, J. S., Scoville, N. Z., Soifer, B. T., & Danielson, G. E. 1987, *ApJ*, 312, L5
 Sargent, W. L. W. 1972, *ApJ*, 173, 7
 Sargent, W. L. W., & Steidel, C. C. 1990, *ApJ*, 359, L37
 Schmelz, J. T., Baan, W. A., & Haschick, A. D. 1988, *ApJ*, 329, 142
 Schmidt, G. D., & Miller, J. S. 1985, *ApJ*, 290, 517

- Scoville, N. Z., Sanders, D. B., Sargent, A. I., Soifer, B. T., & Tinney, C. G. 1989, *ApJ*, 345, L25
- Scoville, N. Z., Sargent, A. I., Sanders, D. B., & Soifer, B. T. 1991, *ApJ*, 366, L5
- Scoville, N. Z., Yun, M. S., & Bryant, P. M. 1997, *ApJ*, 484, 702
- Scoville, N. Z., et al. 1998, *ApJ*, 492, L107
- Shakura, N. I., & Sunyaev, R. A. 1973, *A&A*, 24, 337
- Shaya, E. J., Dowling, D. M., Currie, D. G., Faber, S. M., & Groth, E. J. 1994, *AJ*, 107, 1675
- Shier, L. M., Rieke, M. J., & Rieke, G. H. 1994, *ApJ*, 433, L9
- . 1996, *ApJ*, 470, 222
- Skinner, C. J., Smith, H. A., Sturm, E., Barlow, M. J., Cohen, R. J., & Stacey, G. J. 1997, *Nature*, 386, 472
- Smith, C. H., Aitken, D. K., & Roche, P. F. 1989, 241, 425
- Smith, D. A., Herter, T., Haynes, M. P., Beichman, C. A., & Gautier, T. N. 1995, *ApJ*, 439, 623
- . 1996, *ApJS*, 104, 217
- Smith, H. E., Lonsdale, C. J., & Lonsdale, C. J. 1998a, *ApJ*, 492, 137
- Smith, H. E., Lonsdale, C. J., Lonsdale, C. J., & Diamond, P. J. 1998b, *ApJ*, 493, L17
- Smith, P. S., Schmidt, G. D., Allen, R. G., & Angel, J. R. P. 1995, *ApJ*, 444, 146
- Solomon, P. M., Downes, D., & Radford, S. J. E. 1992, *ApJ*, 387, L55
- Solomon, P. M., Downes, D., Radford, S. J. E., & Barrett, J. W. 1997, *ApJ*, 478, 144
- Sopp, H. M., & Alexander, P. 1991, *MNRAS*, 251, 112
- Staveley-Smith, L., Cohen, R. J., Chapman, J. M., Pointon, L., & Unger, S. W. 1987, *MNRAS*, 226, 689
- Sturm, E., et al. 1996, *A&A*, 315, L133
- Surace, J. A., Sanders, D. B., Vacca, W. D., Veilleux, S., & Mazzarella, J. M. 1998, *ApJ*, 492, 116
- Taylor, G. B., Vermeulen, R. C., Pearson, T. J., Readhead, A. C. S., Hennstock, D. R., Browne, I. W. A., & Wilkinson, P. N. 1994, *ApJS*, 95, 345
- Toomre, A. 1964, *ApJ*, 139, 1217
- Ulvestad, J. S., & Wilson, A. S. 1984, *ApJ*, 278, 544
- van der Werf, P. P. 1996, in *Cold Gas at High Redshift*, ed. M. N. Bremer, H. J. A. Röttgering, & C. L. Carilli (Dordrecht: Kluwer), 37
- van der Werf, P. P., & Israel, F. 1998, in preparation
- Veilleux, S., Kim, D. C., Sanders, D. B., Mazzarella, J. M., & Soifer, B. T. 1995, *ApJS*, 98, 171
- Womble, D. S., Junkkarinen, V. T., Cohen, R. D., & Burbidge, E. M. 1990, *AJ*, 100, 1785
- Woody, D. P., et al. 1989, *ApJ*, 337, L41
- Yun, M. S., & Scoville, N. Z. 1995, *ApJ*, 451, L45
- Zenner, S., & Lenzen, R. 1993, *A&AS*, 101, 363
- Zhao, J. H., Anantharamaiah, K. R., Goss, W. M., & Viallefond, F. 1996, *ApJ*, 472, 54
- Zwicky, F. 1971, *Catalogue of Selected Compact Galaxies and Post-Eruptive Galaxies* (Güemlingen: F. Zwicky)
- Zylka, R., Mezger, P. G., Ward-Thompson, D., Duschl, W. J., & Lesch, H. 1995, *A&A*, 297, 83